

Small Molecule Inhibitors as Probes for Studying the Role of Quiescin Sulphydryl
Oxidase 1 in Tumor-Associated Extracellular Matrix

by

Amber L. Fifield

A Dissertation Presented in Partial Fulfillment
of the Requirements for the Degree
Doctor of Philosophy

Approved October 2020 by the
Graduate Supervisory Committee:

Douglas Lake, Chair
Thai Ho
Chad Borges
Jeffery Rawls

ARIZONA STATE UNIVERSITY

December 2020

ABSTRACT

Quiescin Sulfhydryl Oxidase 1 (QSOX1) generates disulfide bonds in its client substrates via oxidation of free thiols. Localized to the Golgi and secreted, QSOX1 helps to fold proteins into their active form. Early work with QSOX1 in cancer began with the identification of a peptide from the long form of QSOX1 in plasma from patients with pancreatic ductal adenocarcinoma. Subsequent work confirmed the overexpression of QSOX1 in numerous cancers in addition to pancreatic, including those originating in the breast, lung, brain, and kidney. For my work, I decided to answer the question, “How does inhibition of QSOX1 effect the cancer phenotype?” To answer this I sought to fulfill the following goals A) determine the overexpression parameters of QSOX1 in cancer, B) identify QSOX1 small molecule inhibitors and their effect on the cancer phenotype, and C) determine potential biological effects of QSOX1 in cancer. Antibodies raised against rQSOX1 or a peptide from QSOX1-L were used to probe cancer cells of various origins for QSOX1 expression. High-throughput screening was utilized to identify 3-methoxy-N-[4-(1-pyrrolidinyl)phenyl]benzamide (SBI-183) as a lead inhibitor of QSOX1 enzymatic activity. Characterization of SBI-183 activity on various tumor cell lines revealed inhibition of viability and invasion *in vitro*, and inhibition of growth, invasion, and metastasis *in vivo*, a phenotype that was consistent with QSOX1 shKnockdown cells. Subsequent work identified 3,4,5-trimethoxy-N-[4-(1-pyrrolidinyl)phenyl]benzamide (SPX-009) as an SBI-183 analog with stronger inhibition of QSOX1 enzymatic activity, resulting in a more potent reduction in tumor invasion *in vitro*. Additional work with QSOX1 shKnockdown and Knockout (KO) cell lines confirmed current literature that QSOX1 is biologically active in modulation of the ECM. These results provide evidence

for the master regulatory role of QSOX1 in cancer, making it an attractive chemotherapeutic target. Additionally, the small molecules identified here may prove to be useful probes in further elucidation of QSOX1 tumor biology and biomarker discovery.

DEDICATION

I would not be where I am today were it not for the tremendous support and constant encouragement of my husband, Andrew Fifield. He has tirelessly walked (many times crawled) this journey with me. I love you.

To my parents Dennis and Nancy Moyer. You always told me I could be anything I wanted to be. I still don't know for sure what that is, but I suppose a scientist will do.

Thank you to my children, Isaiah and Elsi, for all your hugs and kisses along the way.

To my sister friends Kathi Ridgeway, Jessica Lavelle, Amy English, Becky Barcon, and Jenn Purvis. You have been my therapists for miles. You have brought smiles to my face and joy to my heart.

To Jonah. May our trails be ever wild.

ACKNOWLEDGMENTS

I am filled with gratitude for the many individuals who have poured into my professional life.

To my advisor Dr. Douglas Lake for his guidance and mentorship. When I joined his lab as an undergraduate, I was looking just to learn about research. Little did I know I would finally discover what I wanted to be when I grew up. Thank you to my committee members for your support. To Jeffery Rawls who gave me guidance, helping me to form my writing style, and whose encouraging words came at a key point in my journey to a PhD. To Chad Borges who always had a smile during my presentations and who provided expertise which gave me solid ground to stand on. To Thai Ho who provided significant mentorship, guidance, and financial support. His generosity, along with his excitement for the data, is infectious.

Thank you to all my lab members. To Paul Hanavan for his untiring teaching and continued mentorship. To Calvin Koelbel for his help and inquiring mind. To Kirsten Pfeffer, Alexa Roeder, Francisca Grill, and Austin Blackmon: our many, many conversations about science and graduate life were a joy. To Yvette Ruiz: a huge and special thank you. I could not have done this without her. Her knowledge and wisdom directed me, while her friendship and transparency kept me grounded.

To Cheryl Myers who provided guidance early on and who has continued to be a huge support to me in my journey. To Delon Washo-Krupps who gave me career guidance and friendship. To Anup Abraham who was consistently encouraging and who gave me a chance. To Katon Kras for his mentorship and teaching.

A most special thanks to Natalie Mitchell whose excitement for the unknown sparked new ideas and whose constant friendship kept me joyfully motivated.

TABLE OF CONTENTS

	Page
LIST OF TABLES	viii
LIST OF FIGURES	vix
CHAPTER	
1 INTRODUCTION	1
2 METHODS TO ANALYZE THE ROLE OF SMALL MOLECULE INHIBITORS OF QSOX1 IN RENAL ADENOCARCINOMA AND SARCOMATOID CARCINOMA, BREAST ADENOCARCINOMA, PANCREATIC, AND LUNG CARCINOMA	15
a. Overview	15
b. Materials and Methods	16
3 MOLECULAR INHIBITOR OF QSOX1 SUPPRESSES TUMOR GROWTH IN VIVO	29
a. Overview	29
b. Results	29
c. Conclusions	45
4 TARGETED MODIFICATIONS TO THE CHEMICAL STRUCTURE OF SBI-183 INCREASE INHIBITION OF BOTH QSOX1 ENZYMATIC ACTIVITY AND INHIBITION OF TUMOR INVASION	55
a. Overview	55
b. Results	56
c. Conclusions	94

CHAPTER	Page
5 DISCUSSION AND CONCLUSIONS.....	102
REFERENCES	111
APPENDIX	
A FULL DOCKING SCORES FOR SBI-183	128
B CHEMICAL STRUCTURES FOR TESTED COMPOUNDS	130

LIST OF TABLES

Table	Page
1. Results from SBI-183 Docking Protocols	50
2. SBI-183 Reduces Proliferation	52
3. SBI-183 is Not Toxic to Athymic Nude Mice.....	52
4. SBI-183 Does Not Reduce Primary Tumor Growth of MDA-MB-231 <i>In Vivo</i> ..	53
5. Full Results from SBI-183 Docking Protocols	129
5. List of SPX Compounds and Structures	131

LIST OF FIGURES

Figure	Page
1. SBI-183 Binds to and Inhibits the Enzymatic Activity of QSOX1	31
2. SBI-183 Inhibits Proliferation of Tumor Cells, but Does Not Kill Fibroblasts or Rapidly Proliferating PBMC	36
3. 3D & 2D Invasion of Cells Treated with SBI-183.....	36
4. SBI-183 Reduced Deposition of Laminin α 4 in Tumor Cell ECM Immunofluorescence	38
5. Partial Rescue of Invasive Phenotype by Addition of Exogenous rQSOX1.....	40
6. SBI-183 Does Not Inhibit Activity of Eight Tested Tyrosine Kinases	41
7. Treatment with SBI-183 Suppresses 786-O and RCJ-41T2 Growth in Mice.....	43
8. Treatment with SBI-183 Reduced Laminin α 4 Deposition in RCJ-41T2 Mouse Xenografts	44
9. Chemical Structure of SBI-183.....	49
10. Stably Transduced 786-O Cells Have Reduced QSOX1 mRNA Expression.....	49
11. Viability Dose Response Curve.....	50
12. 3D Invasion Dose Response Curve for SBI-183.....	51
13. SBI-183 Reduces Lung Metastasis <i>In Vivo</i>	54
14. Screening Chemical Analogs of SBI-183 for Inhibition of QSOX1 Enzymatic Activity with the HVA Fluorescence Assay	57
15. SBI-183 Analogs Demonstrate an Inhibitory Dose Response in the HVA Fluorescence Assay	59
16. Chemical Structure of SPX-009	60

Figure	Page
17. SPX-009 Inhibits 3D Invasion in a Dose Dependent Manner	62
18. Determination of SPX-009 3D Invasion IC ₅₀	63
19. SPX-009 is the Strongest Inhibitor of 3D Invasion	64
20. SPX-009 Inhibits 2D Boyden Chamber Invasion in a Dose Dependent Manner	65
21. Addition of Exogenous rQSOX1 Partially Rescues 3D Invasion	66
22. Alterations to the Chemical Structure of SBI-183 Resulting in a Loss of QSOX1 Enzymatic Activity Also Resulted in a Loss of Inhibition of 3D Invasion	67
23. Targeted Modifications to SBI-183 Inhibit 3D Invasion	70
24. SPX-009 Modulates Spheroid Formation	72
25. SPX-009 Inhibits Proliferation by Day Five, but Not by Day Three by MTT	73
26. Determination of SPX-009 Viability IC ₅₀	75
27. QSOX1 Levels in Supernatant Increase over Time	77
28. Inhibiting QSOX1 Does Not Increase Expression of Three Sulfhydryl Oxidases in Compensation	79
29. Genetic Knockdown or KO of QSOX1, or Inhibition of QSOX1 with SPX-009, Modulates ECM Formation via Deposition of Laminin α 4 in 3D Invaded Cells	81
30. 3D Invaded Cells Treated with SPX-009 Display Disorganization of Laminin α 4	83

Figure	Page
31. Treatment with SPX-009 Causes Disorganization of F-actin in 3D Invaded Cells.....	84
32. Immunostaining of Fibronectin on 3D Invaded Cells Does Not Yield Any Consistent Changes in Intensity or Organization Between Conditions/Cell Lines	86
33. Immunostaining of Nidogen on 3D Invaded Cells Causes an Increase in Nidogen Intensity in MIA PaCa2, but No Changes in Other Cell Lines	88
34. Immunostaining of Versican on 3D Invaded Cells Resulted in No Consistent Changes Between Condition/Cell Lines.....	90
35. Immunofluorescence Images of 3D Invasion Short Hairpin, DMSO Vehicle, or SPX-009 Treated MDA-MB-231 and MIA PaCa2 Not Treated with Primary Antibody (Secondary Antibody Only Control)	92
36. Immunofluorescence Images of 3D Invasion HAP-1 Parental or HAP-1 QSOX1 KO Incubated Without Primary Antibody (Secondary Antibody Only Control).....	93
37. SPX-009 IC ₅₀ 's in 3D Invasion and Proliferation Do Not Correlate with QSOX1 Expression	101

CHAPTER 1

INTRODUCTION

The second leading cause of death in the United States is the heterogeneous disease cancer, making it a major public health concern (1). Each patient's germline is genetically unique. Additionally, each individual has their own singular gene expression modifications, plus an accumulation of genetic and epigenetic mutations from which cancer arises. This leads to tumors composed of highly variable cells within an individual which are completely different from any other patient (2). The uniqueness of tumors makes both drug discovery and fighting cancer exceedingly difficult since chemotherapeutics which are effective in one patient may not be effective in another. While genetically cancer is heterogeneous, phenotypically it does have general hallmarks including uncontrolled cell growth, immortalization, invasion, and metastasis (3). Typically, cancer associated deaths are due to metastasis and not the primary tumor (4). Current drug discovery methods aim to selectively inhibit at least one of these hallmarks (5), with the goal of inhibiting metastasis, thereby prolonging patient survival.

The goal of cancer drug discovery is to identify novel anti-cancer therapeutics while minimizing damage afforded to healthy cells (6). The two major methods currently utilized in drug discovery are either target based or phenotype based. In the target based approach, modulation of the protein of interest in cells is performed through methods such as clustered regularly interspaced short palindromic repeats (CRISPR) or RNA interference (RNAi), and the resultant phenotype is observed. An ideal target candidate will be overexpressed in cancer cells and be essential in tumor progression, while not effecting normal cells (7). Once a target protein has been identified, high-throughput

screening strategies are performed utilizing purified target protein and libraries of potential chemotherapeutics. After identification of top hits, the compounds are applied to a biological system to again observe the phenotype. The major drawbacks of this method are the time-consuming data validation to verify the protein of interest as a target, and the fact that the interaction of the compound with the protein initially occurs in a highly artificial environment. Compounds identified via this method may give a different phenotype on cells than what would be expected from inhibition of the target due to off-target effects, or due to a lack of interaction with the intended target in a biologically relevant model. Additional research to increase affinity of the compound for the target and to identify other cellular targets is required. In the phenotype based method, the targets of the compounds are unknown. Instead, the compounds are directly applied to biological systems. Compounds that give the desired phenotype are further screened to identify the target or targets. This method provides an unbiased approach in cancer drug discovery, and additionally allows for the identification of novel biomarkers, however the subsequent screening to identify targets is again exceedingly time-consuming and complex (6,8,9). Whichever method is used, the end goal is to improve patient survival, so any compound discovered must translate to the clinic. To aid drug discovery, it is imperative to have an understanding of the tumor microenvironment, what is occurring in tumor cells during invasion and metastasis, and how *in vitro* growth conditions effect the cellular phenotype.

The primary tumor initially grows in its microenvironment. This heterogeneous environment consists of both cancerous and non-cancerous cells, with all cell types secreting extracellular matrix (ECM). The ECM, which is constantly undergoing

deposition, degradation, and remodeling, is integral in structural support and cell signaling for such processes as inter- and intracellular communication, proliferation, adhesion, and invasion. Major components of the ECM are variable by tissue type and, among many other proteins, include laminin, collagen, and fibronectin (4,10), and their numerous sub-types. Each of these proteins contains at least one disulfide bond, leading to its final, functional structure. The ECM of a tumor is abnormally stiff due to aberrant expression and secretion of ECM structural and remodeling proteins (11,12). This stiffness, in turn, enhances tumor proliferation and invasion (13), making proteins of the tumor ECM an attractive target in drug discovery.

Tumor cell invasion, in which cells invade the surrounding ECM and basement membrane, is an early step in the metastatic process, and therefore is regularly studied during drug discovery. The general steps leading to deadly cancer metastasis are highly influenced by the ECM and are as follows: Epithelial Mesenchymal Transition (EMT), Intravasation, Circulation, Engraftment, and Outgrowth (4). EMT, influenced by numerous ECM constituents including hyaluronan (HA) and versican, is characterized by the downregulation of epithelial protein markers (i.e. E-cadherin) and the upregulation of mesenchymal markers (i.e. N-cadherin), resulting in a migratory mesenchymal phenotype (4). Once migratory, the tumor cells invade their local microenvironment and enter the lymphatic system or bloodstream. This intravasation is influenced by HA, which is involved in regulating the integrity of blood vessels. It is degraded to low molecular weight (LMW)-HA, which disrupts endothelial cell barrier functions and promotes angiogenesis (4,14,15). Survival in the blood stream includes resistance to sheer forces and evasion from the immune system. Among other possible pathways, the plasma

protein fibrinogen can be secreted by tumor cells and act as an ECM protein, inducing a protective barrier of platelets to form around the free-floating tumor cells (4,16–18). Following HA mediated adhesion and extravasation at a distal site, the tumor cells must set up residence at a foreign site in the body. Tumor secreted ECM constituents such as lysyl oxidase (LOX) and tenascin c, make the metastatic site more permissive to engraftment. Additionally cancer cells also induce the surrounding stroma to secrete tumor-supporting ECM, such as periostin to support tumor adhesion and proliferation (4,19,20). Finally, metastatic outgrowth is again heavily influenced by ECM components (tenascin c, periostin, fibronectin, etc.) mediating tumor proliferation and viability (4,21,22).

In order to effectively study tumor biology in the lab, cancer cell lines are cultured *in vitro* and are subjected to various experimental stimuli to determine the effect on cell behavior. Commonly, adherent cells are cultured in 2D monolayer conditions in which they are seeded onto a flat surface which is coated with a chemical or protein such as polylysine or collagen, to promote their adhesion. While 2D culture conditions allow scientists to study singular changes to cells, something that is not possible in a cellularly heterogeneous animal, often 2D cells do not accurately recapitulate an *in vivo* phenotype (23–25). Differences in proliferation, differentiation, and invasion (25–30) are common causing a roughly 90% failure rate of novel therapeutics at the clinical trial level due to a lack of efficacy or toxic side effects (28,31). This is because the 2D monolayer does not allow for the spatial organization and physical constraints observed with *in vivo* cells (6,28). The 3D tumor biology model allows cells to be morphologically and physiologically similar to those observed *in vivo*, as evidenced by the formation of

heterogeneous tumoroids with a hypoxic core, the formation of and interaction with a more *in vivo*-like microenvironment, and more appropriate signal transduction leading to *in vivo*-like gene expression (6,28,32). Further, the 3D tumoroid itself poses a diffusion barrier which a studied compound must overcome- a barrier which is not present in flat, stretched out, 2D cells (28). While 2D culture systems have a valuable place in tumor biology, a model 3D culture system provides data which more closely mimics the phenotype observed in the body.

The numerous proteins of the tumor microenvironment all contain disulfide bonds which are generally thought to be formed in the endoplasmic reticulum (ER), prior to membrane localization or secretion (33). The protein family known as sulfhydryl oxidases (SOXs) catalyze the formation of disulfide bonds in protein substrates from the oxidation of free sulfhydryls, with oxygen as the final electron acceptor resulting in hydrogen peroxide (H_2O_2) as the byproduct of enzymatic activity. Disulfide bonds are a covalent linkage which can be reversed (by thiol reductases) or changed (by thiol isomerases) (34), and can be intra- or intermolecular (34). The disulfide bond is an important structural aspect of ECM proteins, leading to their proper structure and functionality (34).

There are numerous SOXs which have implications in cancer. As is seen with ECM proteins, SOXs are often aberrantly overexpressed by cancer as compared to normal tissue, with the implication that their activity benefits tumor survival. Due to their intimate involvement with catalyzing the final functional state of client substrates, some SOXs may serve as potential “master regulators” of the cancer phenotype. This dissertation will focus on QSOX1 (described later). First I will describe three other SOXs

which are important in cancer progression and drug discovery, which are related to QSOX1 structurally, and which were briefly examined as part of this work; protein disulfide isomerase (aliases: PDI, PDIA1, P4HB, PHDB), endoplasmic reticulum oxidoreductin 1 (aliases: ERO1, ERO1L), and augments liver regeneration (aliases: ALR, GFER, HPO, HSS, ERV1).

PDI, a 55kD protein, is part of the thioredoxin (Trx) superfamily which contain at least one CxxC (where “x” is any amino acid) motif (35). PDI has two enzymatically active CxxC motifs. It is targeted to the ER via a KDEL retention signal (36,37), but it has also been identified in the plasma membrane (37–39). PDI is involved in disulfide bond formation, reduction, and isomerization in substrate proteins (40). Nascent polypeptides enter the ER with reduced cysteine residues. Oxidized PDI grabs the electrons from the cysteine residues, forming a disulfide bond on the substrate while itself becoming reduced in the process. To become reoxidized, PDI must coordinate with, among other oxidation partners, ERO1. ERO1 reoxidizes PDI via its CxxCxxC motif; on ERO1, electrons are shuffled to flavin adenine dinucleotide (FAD) then to molecular oxygen as the final electron acceptor (41–43).

By gene expression and proteome analysis, PDI is significantly upregulated in numerous cancers including those of the brain and central nervous system (CNS) (44–50), kidney (50–53), ovaries (50,54,55), prostate (50,56–58), lungs (50,59), and male germ cells (50,60). It is upregulated in lymphoma (50,61–63), male and female infiltrating ductal breast carcinoma (50,64,65), and in breast tumor interstitial fluids (50,66). PDI is also a marker in tumor invasion and metastasis in breast cancer (50,67), and glioma (68). Inhibiting tumor PDI with bacitracin (69) sensitizes cells to the

chemotherapeutics Aplidin (HeLa) (70), fenretinide and velcade (melanoma), and 3-Bromopyruvate (3BP) (hepatocellular carcinoma or HCC) (71). Inhibition of PDI with siRNA in ovarian cancer cell lines severely attenuated their growth, similar to treatment with propynoic acid carbamoyl methyl amides (PACMA) 31 (72). While inhibition of PDI in tumor cells typically results in cytotoxicity, this is not always the case. One study found that siRNA inhibition of PDI was not cytotoxic in HeLa cells. This difference from other cancers was possibly due to differential activation of caspase cascades during apoptosis (73). PDI demonstrates the necessity of elucidating the full molecular context of potential cancer therapeutic targets.

There are two isoforms of ERO1 in vertebrates: ERO1 α and ERO1 β (74–77). Both have the same enzymatic function, but, with minor overlap, different tissue localization. ERO1 α will be discussed briefly in this dissertation due to its wide tissue distribution (74,76) and the wealth of data correlating its expression with cancer progression.

ERO1 α , a 54kD protein disulfide oxidase, works in close conjunction with PDI in the ER. Once PDI forms a disulfide bond in its client substrate and itself becomes reduced, ERO1 reoxidizes PDI. ERO1, via its FAD moiety, shuttles the electrons onto molecular oxygen as the final electron acceptor, resulting in H₂O₂. This reaction oxidizes ERO1 again, making it available to repeat the cycle with PDI (78–80).

ERO1 α overexpression is associated with a poor prognosis in all cancers surveyed (81–92). Inhibition of ERO1 α with siRNA in cholangiocarcinoma and HCC reduces proliferation and migration (83), and metastasis and angiogenesis (89) respectively. In triple negative breast cancer models, siRNA knockdown (KD) or treatment with the

ERO1 α inhibitor EN460 (93) resulted in a reduction of Programmed Death Ligand 1 (PD-L1) on the cell surface. In a cervical cancer cell model, CRISPR/Cas9 knockout (KO) resulted in decreased intracellular H₂O₂ which inhibited EMT markers. Additionally, cancer cell growth and invasion were also reduced (84). More work is needed to understand ERO1 α in cancer and how inhibition with antibodies or small molecules will impact the cancer phenotype.

ALR, is an intracellular, 22kD protein localized to the cytosol and to mitochondria of all mammalian cells (94,95), however it may also be secreted (96). It is dependent on a CxxC motif and FAD for enzymatic function (97), donating electrons from enzymatic activity to either cytochrome c (mitochondria) or oxygen (98,99). ALR appears to be a favorable prognostic marker in renal cancer (100–102). ALR may have antimetastatic properties in HCC (96,103), however another study demonstrated that it may be a therapeutic target in hepatoma by inhibiting viability and resistance to radiation-induced oxidative stress (104). ALR has been implicated in hepatocarcinogenesis (105), and glioma and neuroblastoma anti-apoptosis and anti-oxidation (106,107). In 2017, Guo *et al* reported that overexpression of ALR in HCC had antitumor effects due to increased intracellular retention of the chemotherapeutic doxorubicin (108). Other studies have shown that inhibition of ALR with siRNA increases the sensitivity of acute T lymphoblastic leukemia to the chemotherapeutic vincristine (109), or decreases tumor growth *in vitro* and in an *in vivo* allogeneic mouse model of HCC, similar to treatment with an anti-ALR monoclonal antibody (110). The apparently conflicting roles of ALR in cancer may be due to differences in localization of the long (23kD) and short (15kD) isoforms (96). The short form is found in the nucleus,

cytosol, and extracellularly. In each instance it is a pro-proliferative growth factor (111–117). The long form of ALR is active in the mitochondrial intermembrane space where it interacts with MIA40 (mitochondria intermembrane space import and assembly protein 40), reoxidizing it to its active state, as part of a disulfide relay system (99,118). When the long form is localized to the cytosol, it modulates mitochondrial morphology and hematopoietic stem cell proliferation (119,120). The seemingly conflicting data in the literature make it apparent that it is imperative to note the molecular context of ALR when considering research into targeted therapy.

An understudied SOX which is overexpressed in all cancers examined to date is Quiescin Sulfhydryl Oxidase 1 (QSOX1). In 1993, Coppock *et al* were studying WI38 fibroblasts and noted the upregulation of two cDNA clones, termed Q6 and Q10, during transition from logarithmic growth to quiescence (121). Later these clones were identified as mRNA splice variants of the QSCN6 gene, located on chromosome 1: QSOX1-Long (QSOX1-L, 747 amino acids) and QSOX1-Short (QSOX1-S, 604 amino acids) (122,123). The reaction catalyzed by QSOX1 is the same as that of PDI/ERO1, however, because QSOX1 is one enzyme, the reaction rate is orders of magnitude higher (124). Because QSOX1's reaction is the same as PDI/ERO1, and because QSOX1 can suppress the lethality of a complete KO of ERO1 in yeast (125), it would seem that intracellular QSOX1 activity would be localized to the ER. Instead, QSOX1 is found primarily in the Golgi apparatus and secreted (125,126).

QSOX1, found in all multicellular organisms (127) and some protists including *Trypanosoma* (128), but not in fungi (122) is comprised of an ancient fusion of two Trx domains and an ERV/ALR domain, joined by a helix-rich flexible linker region (HRR).

The enzymology of QSOX1 has been well-studied (124,125,128–138). The first Trx domain (Trx1) contains the initial CxxC motif imperative in enzymatic activity, C₇₀ and C₇₃. These cysteines are responsible for the initial electrophilic attack on the free sulfhydryls in a reduced client substrate. The second Trx domain (Trx2) does not contain a CxxC motif, but does have two cysteines at C₁₆₅ and C₂₃₇ (129). Neither of these cysteines are thought to participate in enzymatic activity, however in 2015, Hanavan *et al* reported that the small molecule ebselen bound covalently to both of these cysteines, inhibited tumor invasion *in vitro*, and reduced tumor growth in a mouse xenograft model (139). They hypothesized that by binding to these cysteines, ebselen may prevent Trx1 from coming into close proximity with the ERV/ALR domain which would prevent electron shuttling. Alternatively, they proposed that these cysteines may be involved in modulation of QSOX1 enzymatic activity. Additionally, in 2019, I reported that the novel small molecule SBI-183 bound non-covalently near C₂₃₇, lending more support for the role of this region in modulation of enzymatic activity (27). The HRR allows the QSOX1 molecule to bend, bringing the Trx1 into close proximity with the ERV/ALR domain (136,137). The ERV/ALR domain contains the second CxxC motif of QSOX1 (C₄₄₉ and C₄₅₂) closely associated with FAD and as the name implies, is a homolog to ALR. Similar to the PDI/ERO1 α enzymatic activity model, electrons from the initial electrophilic attack are shuttled from Trx1 to the CxxC motif in the ERV/ALR domain. From there they go to FAD to form FADH₂ and then to molecular oxygen as the final electron acceptor, resulting in H₂O₂ as the final byproduct of enzymatic activity (129). Downstream of FAD is another CxxC motif (C₅₀₉ and C₅₁₂) which, interestingly, is not involved in enzymatic activity and its function is unknown (129). QSOX1-S and

QSOX1-L contain the same amino acid sequence up until the ERV/ALR domain except at 603 and 604. QSOX1-S ends with leucine and isoleucine while QSOX1-L has alanine and serine at these positions and continues on, containing the NEQ peptide (140) and a transmembrane domain. Both variants are enzymatically active. It is currently unknown why there are two forms.

While the enzymology of QSOX1 is well-characterized, the characterization of its biological role is just beginning. In 2007, Morel *et al* described a protective role for QSOX1 in breast cancer during oxidative stress induced apoptosis, partly through preservation of mitochondrial polarization (141). In prostate tumorigenesis, QSOX1 mRNA and protein levels were upregulated following the loss of the transcriptional regulator and tumor suppressor Nkx3.1 (142) likely due to its pro-oxidative effects (143). In pancreatic cancer cell models, QSOX1 expression was shown to be under the control of hypoxia-inducible factor 1 (HIF1) (144). An ECM “master regulator” role for QSOX1 has been described via modulation of deposition of laminin α 4 in siRNA WI38 fibroblasts (145) and with the small molecule inhibitor, SBI-183 (27); in a shRNA model and a hypoxia induced model via activation of the basement membrane degrading matrix metalloproteinase (MMP)-2 and -9 (144,146); and via defective fibronectin organization in WI38 cells upon addition of exogenous mutant QSOX1 (147). Both fibronectin and collagen showed aberrant organization when QSOX1 was inhibited with a monoclonal antibody in an allogeneic mouse model (148). Recent work has shown QSOX1 to be involved in proliferation, migration, and invasion in glioblastoma cells via the PI3k/AKT pathway (149). While these results begin to give insight into the regulation and biological

function of QSOX1, much work remains to be done, including discovery of QSOX1 biological substrates.

As with the other SOXs discussed here, QSOX1 has been heavily implicated as a poor prognostic marker in the progression of many cancers (139,140,142,143,146,150–156). In a prostate carcinogenesis mouse model (mice are *Nkx3.1^{-/-}*) QSOX1 mRNA and protein expression were upregulated (143). In patients with pancreatic ductal adenocarcinoma a peptide from QSOX1-L (termed the NEQ peptide) was discovered circulating in their plasma, but not in normal donors. Additionally QSOX1 was overexpressed in pancreatic tumors but not in adjacent healthy tissue (140). QSOX1 is a biomarker of HCC (155). It has a pro-invasive phenotype in pancreatic cancer (27,139,144), in renal cancer (27,139), in nasopharyngeal carcinoma (154), in breast cancer (27,148,150–152), in glioblastoma (149), and a pro-metastatic phenotype in lung cancer (153). QSOX1 overexpression was shown to increase radioresistance in nasopharyngeal carcinoma (154). Interestingly, similar to PDI and ALR, there is also literature which apparently conflicts with these pro-tumorigenic and poor prognostic reports, stating that QSOX1 is a favorable prognostic marker in breast cancer (157,158) and HCC (159). It is possible that these apparent disparities could be explained as being due to differential cell signaling as may be the case with PDI, or differential localization of the splice variants as may be the case with ALR. Interestingly, differential localization of QSOX1 splice variants has been reported by Radom *et al* in rats; QSOX1-S was ubiquitously expressed while QSOX1-L was specifically detected in brain tissue (160). Differential subcellular and extracellular compartment localization in different tumors/cell lines seems a plausible explanation and has been suggested by Rudolf *et al*

(126). These variable results highlight the need for a full understanding of the molecular context of QSOX1 in tumor progression.

With the wealth of data which points towards QSOX1 being an important player in the progression of cancer, it was hypothesized that inhibition of QSOX1 enzymatic activity would suppress the cancer phenotype. Other previous work supports this hypothesis. The viability of arsenicals as chemotherapeutics targeting QSOX1 was studied. While this approach did inhibit protein folding, the main target of the arsenicals was the disordered unfolded proteins themselves, showing the need for QSOX1 targeted small molecules (161). Inhibition of QSOX1 enzymatic activity with the small molecule ebselen led to a reduction in tumor proliferation and invasion *in vitro* and a reduction in tumor volume in a xenograft nude mouse model (139). Inhibition of QSOX1 enzymatic activity with the small molecule SBI-183 resulted in a decrease in tumor proliferation and 2D and 3D invasion in *in vitro* models, a reduction in tumor volume of two renal xenograft mouse models (nude and NSG mice), and a reduction in metastasis in a xenograft CB.17 SCID mouse model (27) (discussed in depth in Chapter 3). Utilizing anti-QSOX1 antibodies as potential therapeutics, one paper described a single chain antibody which inhibits enzymatic activity, preventing the migration of tumor cells across a fibroblast monolayer (138). Additionally anti-QSOX1 monoclonal antibodies decreased breast and melanoma tumor growth and metastasis in syngeneic BalbC and C57BL/6 mouse models, and a breast cancer xenograft nude mouse model (148).

This work aimed to elucidate the biological expression profile of QSOX1 in cancer and identify and characterize targeted novel small molecule therapeutics against the enzyme, characterizing the resultant cancer phenotype. The final goal of this work is

for QSOX1 small molecule inhibitors to eventually be used clinically in combined chemotherapy. Initially QSOX1 expression in cancer cell lines was probed using a polyclonal antibody against QSOX1-L. Small molecule screening was performed on a library of ~50,000 small molecules in a cell-free QSOX1 enzymatic activity assay in collaboration with Sanford Burnham Prebys Medical Discovery Institute (SBI). Of these, 3-methoxy-n-[4(1pyrrolidinyl)phenyl]benzamide (SBI-183) was a top hit and was subjected to further biological analysis. In collaboration with Sapphire Biotech, Inc. ~50 chemical analogs of SBI-183 were purchased and again screened in the cell-free enzymatic assay. Structural modifications to SBI-183 and the resultant effect on enzymatic activity and the cancer phenotype were explored. Additionally, this work utilized QSOX1 KD and KO models in conjunction with identified potential therapeutics as probes to broaden our understanding of the molecular context of QSOX1 in cancer.

CHAPTER 2

METHODS TO ANALYZE THE ROLE OF SMALL MOLECULE INHIBITORS OF QSOX1 IN RENAL ADENOCARCINOMA AND SARCOMATOID CARCINOMA, BREAST ADENOCARCINOMA, PANCREATIC, AND LUNG CARCINOMA

Overview:

In collaboration with Sanford Burnham Prebys Medical Discovery Institute and Mayo Clinic, the small molecule, “SBI-183” was identified as the top inhibitor of QSOX1 enzymatic activity from the Library of Pharmacologically Active Compounds (LOPAC¹²⁸⁰) and an in-house library containing 50,000 compounds, utilizing a cell-free activity assay with RNaseA as a model substrate. Microscale Thermophoresis and Computer Modeling were used to determine the interaction of SBI-183 with QSOX1. SBI-183 was screened biologically to determine inhibitory effects. RNAi technology was used as a positive control. Mice were implanted with tumor cell line xenografts and treated with SBI-183 or vehicle control to determine the effects of SBI-183 on tumor growth and metastasis *in vivo*. Xenograft tumors were harvested and analyzed for effect on ECM composition. Subsequent screening was performed on seventy-one additional analogs, with one compound, termed SPX-009, emerging as the top hit, with increased inhibition of enzymatic activity and 3D invasion as compared to SBI-183. Rescue invasion assays were performed, confirming QSOX1 as a cellular target of SPX-009. Immunofluorescence on 3D invaded spheroid ECM's revealed increased intensity of laminin $\alpha 4$ in SPX-009 treated spheroids versus controls. This phenotype was likely due

to incorrect laminin $\alpha 4$ deposition because of interrupted f-actin formation, indicative of a potential additional cellular target of SPX-009 in the cytoskeleton.

Materials & Methods:

Compounds

SBI-183 (molecular weight 296.3723 g/mol) and SPX-009 (molecular weight 356 g/mol) were purchased from ChemBridge Corp. (San Diego, CA). Compounds were dissolved in tissue culture-grade DMSO (Sigma-Aldrich) and kept at -20°C to -80°C as 10 - 20 mM stock solutions. Other reported compounds were purchased from ChemBridge Corp. or synthesized by collaborators as described. See Figure 9, Figure 16, and Table 6 for the chemical structures of SBI-183, SPX-009, and all reported compounds respectively.

TCA Precipitation

One mL of cell culture supernatants were collected and four mL of ice-cold TCA precipitation buffer (10% TCA, .007% DTT, in acetone) was added and briefly vortexed. Samples were centrifuged at 3,000xg for 10 minutes. Pellets were re-suspended in one mL of wash buffer (.007% DTT in acetone) and centrifuged to pellet three times. Pellets were re-suspended in 500 μL of rehydration buffer (7M urea, 2M thiourea, 4% CHAPS, .02M DTT), loaded onto a 3kD Amicon filter (Millipore) and buffer exchanged with PBS. A BCA assay was utilized to estimate protein concentration.

SDS-PAGE Western Blot

Cells were washed two times in PBS and lysed in the flask using ice cold RIPA buffer. Pellets were centrifuged at 21,000xg, and the supernatant was removed to a new Eppendorf tube. Protein concentration was estimated using a BCA assay.

Five – twenty μg total protein was loaded onto an 8-16% Mini-PROTEAN TGX Gel (BIORad) and run at 120V for 55 minutes. Proteins were transferred to a PVDF membrane at 90V for 90 minutes, on ice. Membranes were blocked with 1% BSA-TBST for at least one hour. Membranes were probed with primary antibodies in blocking buffer as follows: 2 $\mu\text{g}/\text{mL}$ αNEQ polyclonal antibody, αERO1 clone 2G4/12 (Millipore) at 1:1000, αGFER polyclonal antibody (Sigma-Aldrich) at .4 $\mu\text{g}/\text{mL}$, and αPDI clone RL90 (Invitrogen) at 1:1000. Membranes were washed 3x with TBST, then probed with the appropriate secondary antibody conjugated to HRP for one hour at room temperature. Membranes were washed 3 times in TBST, then briefly rinsed in PBS before applying SuperSignal West Dura Extended Duration Substrate (Thermo Fisher Scientific). Membranes were imaged on Amersham Imager 680 (GE Healthcare) and edited in Photoshop.

ELISA

High-bind plates (Corning) were coated with 1 $\mu\text{g}/\text{mL}$ 3A10.6 monoclonal antibody in ELISA coating buffer overnight at 4°C. In a separate plate, cell lysates were loaded at 20 $\mu\text{g}/\text{mL}$ and diluted two-fold down the plate, prior to loading onto the ELISA plate. Cell culture supernatants were concentrated 4x on a 3kD Amicon filter (Millipore), then diluted in the same manner as cell pellets prior to ELISA plate loading. The antigen was incubated for one hour at room temperature followed by 4 washes with ELISA wash buffer (.05% Tween-20 in PBS). Detection antibody was incubated for one hour at room temperature and was loaded as follows: αNEQ at 2 $\mu\text{g}/\text{mL}$ or 2F1.F4.14 monoclonal antibody (biotinylated) at 1 $\mu\text{g}/\text{mL}$. Plates were washed 4x with ELISA wash buffer then detected with GaR-HRP (NEQ) or streptavidin-HRP (2F1). After addition of TMB

substrate (BD Biosciences) development occurred for 5-20 minutes, and was stopped with .016M H₂SO₄, and read on a plate reader (Molecular Devices).

Cell Culture

RCC line 786-O was purchased from the American Type Culture Collection (ATCC) and maintained in RPMI 1640 (Corning) containing 10% fetal bovine serum (FBS) (Atlanta Biologicals), 1% Penicillin-Streptomycin (Pen-Strep) (Corning), and 1% Glutamax (Gibco). A recently derived sarcomatoid RCC line from Mayo Clinic, RCJ-41T2 (162), was maintained in DMEM in 5-10% FBS, 1% Pen-Strep, and 1% Glutamax. The TNBC adenocarcinoma cell line MDA-MB-231 (ATCC), lung adenocarcinoma cell line A549 (ATCC), pancreatic ductal adenocarcinoma cell line MIA PaCa2 (ATCC), and WI38 fibroblasts (ATCC) were also maintained in 5-10% DMEM. MDA-MB-231-Luc (Cell Biolabs) was maintained in 10% RPMI 1640 without Pen-Strep. De-identified fibroblasts derived from a 28-year-old Caucasian male with no overt disease were a kind gift from Dr. Clifford Folmes. Peripheral blood mononuclear cells were obtained under an IRB-approved protocol (#06010000548) from Arizona State University. The identity of all cell lines was confirmed by STR analysis. Each cell line also tested negative for mycoplasma and mouse pathogens throughout the study and were maintained at 37°C in 5% CO₂. All cell lines were used immediately upon thawing throughout the study.

Stable Lentiviral QSOX1 KD Generation

Short hairpin (sh) lentiviral particles were purchased from GeneCopoeia containing either sh742 RNA as described (151) (Catalog # LPP-CS-HSH273J-LVRU6GP-100) or a shScramble (shScr) control (Catalog # LPP-CSHCTR001-LVRU6GP-025). 786-O cells were seeded at 2.5x10⁴ cells/well in a 6-well plate in

complete RPMI 1640. Adherent cells were transduced in triplicate with lentiviral particles following the manufacturer's instructions. After 72 hours, cells were selected in puromycin and sub-cloned by limiting dilution. A monoclonal population denoted as 786-O sh742.E11 was expanded. KD of QSOX1 was determined to be 90% by qRT-PCR as compared to the 786-O shScr cells (Figure 10).

Enzymatic Activity Assay

PcDNA3.1 containing the short form of human QSOX1 (rQSOX1) was used to transfect Freestyle 293F cells (Thermo Fisher Scientific). rQSOX1 was expressed by 293F cells, harvested from supernatants and purified on a nickel column via the C-terminal histidine tag. Enzymatic activity of QSOX1 and inhibitory activity of SBI-183 was confirmed using a fluorogenic assay as previously reported (131). Briefly, a mixture of 150 μ M dithiothreitol (DTT) substrate (Sigma-Aldrich), was added to 150 nM rQSOX1, 1.4 μ M horse radish peroxidase (HRP) (Thermo Fisher Scientific), and 1 mM homovanillic acid (HVA) (Sigma-Aldrich) in PBS at ambient temperature, pH 7.5. Assays were performed in a black plate in a total volume of 150 μ L in triplicate. Fluorescence was measured at 20 second intervals over 15 minutes after the addition of DTT at λ_{ex} 320 nm/ λ_{em} 420 nm using a FlexStation spectrophotometer (Molecular Devices). SBI-183 was pre-incubated with rQSOX1 for at least 10 minutes at concentrations ranging from 6.25 μ M – 50 μ M.

Microscale Thermophoresis (MST)

rQSOX1 was labeled with DyLight 650 Amine-Reactive Dye (Thermo Fisher Scientific). Briefly, Dylight-650 was dissolved at 10 mM in dimethylformamide and added at 2:1 molar ratios to 86 μ M QSOX1 in 50 mM NaPO_4^{3-} , 150 mM NaCl, pH 8.0.

The mixture was incubated in the dark for one hour at room temperature on a rocker, and dialyzed to 50 mM Tris, 150 mM NaCl pH 8.0 overnight at 4° C. The labeling ratio was estimated using $\epsilon=250000 \text{ M}^{-1}\text{cm}^{-1}$ at 655 nm for DyLight 650 and $\epsilon=93110\text{M}^{-1}\text{cm}^{-1}$ at 280 nm for QSOX1, and found to be 1.1.

MST experiments were performed in a Monolith NT.115 (Nanotemper). Sixteen serial dilutions of SBI-183 (from 250 mM to .0076 mM) with 50 nM Dylight 650-labeled QSOX1 in 1x PBS, pH 7.4, 5% DMSO, and .05% Tween 20 were loaded into standard MST capillaries and scanned at MST power of 20% at 23°C. To obtain Kd, MST data were fitted using MO Affinity Analysis software (Nanotemper).

Small Molecule Docking

Docking for SBI-183 was performed using Glide (v. 5.6) within the Schrödinger software suite (Schrödinger, LLC) (163). Our modeling techniques have been described (164–170). Briefly, we started with conformation searches of the ligand via the method of Polak-Ribière conjugate gradient (PRCG) energy minimization with the Optimized Potentials for Liquid Simulations (OPLS) 2005 force field (171) for 5000 steps (or until the energy difference between subsequent structure was less than .001 kJ/mol-Å) (163). Our docking methodology has been described (164,169,172), and the scoring function utilized described elsewhere (173). Briefly, molecular refracting molecules were removed from the human QSOX1 crystal structure (PDB Codes: 3Q6O) (136). Schrödinger's SiteFinder module focused the grid on the active site region for QSOX1 (Figure 1C). Using this grid, initial placement for SBI-183 was docked using the Glide algorithm within the Schrödinger suite as a virtual screening workflow (VSW). The docking proceeded from lower precision through SP docking and Glide extra precision (XP)

(Glide, v. 5.6, Schrödinger, LLC) (170,174). The top poses were ranked for best score and unfavorable scoring poses were discarded. Multiple orientations were allowed in the site. Site hydroxyls were allowed to move with rotational freedom. Full docking scores are given in Appendix A (Table 5). This method provides the ideal conformation of ligand binding as utilized within Schrödinger suite, and the top docked pose represents the conformation of the ligand required to inhibit QSOX1. Hydrophobic patches were utilized within the VSW as an enhancement. XP descriptors were used to obtain atomic energy terms that result during the docking run (170,174). Molecular modeling for importing and refining the X-ray structure and generation of SBI-183, as well as rendering of figure images were completed with Maestro (Schrödinger, LLC).

Cellular Viability Assay

Cells were plated at optimized densities (1000 cells/well for 786-0 and RCJ-41T2; 750 cells/well for MDA-MB-231) (described below) in their respective media, and plated in Corning 3570 384-well white titerplates using a MultiFlo bulk dispenser (BioTek). The cells were allowed to adhere for 24 hours. Compound and assay controls diluted in 100% DMSO were added to the cells using an ATS Gen4 acoustic transfer system (EDC Biosystems). A 1:1000 compound:cell volume ratio was enforced to avoid DMSO toxicity. After 72 hour compound incubation, 25 μ L CellTiter Glo reagent (Promega, G7573) diluted 1:4 in MilliQ water was added to the plates using the Multiflo dispenser and luminescent signal was read per standard assay protocol using a Molecular Devices Paradigm multi-mode reader (TUNE cartridge, luminescent mode).

Prior to screening, assay optimization experiments were performed for each cell line in the assay conditions described above. Cell densities were titrated in control plates

containing negative and positive controls (DMSO and 10 μ M staurosporine, .1% DMSO in assay wells) to identify optimal seeding densities within linear ranges of luminescent signal, minimizing CVs (<10%) and maximizing Z' factors (>.5), per standard NIH assay guideline optimization criteria and methods. For primary screens, 20-point 2-fold serial dilutions of SBI-183 in 100% DMSO were prepared from a stock concentration of 40 mM in acoustic-compatible Aurora microplates (Ref ABA200100A); internal plate controls for live cells (100% viability) and dead cells (0% viability) were included in source plates. After 24 hour seeding time, compound was added acoustically as described above. Cellular viabilities for each test well were derived from raw luminescent signal by normalization to internal plate controls. Viability experiments were performed in triplicate, and normalized data points averaged per dose. Dose-response curves were calculated by logistic regression in TIBCO Spotfire (version 7.0.0).

Proliferation Assay

786-O, RCJ-41T2, MDA-MB-231, A549, and MIA PaCa2 were seeded in triplicate at 2.5×10^3 cells/well (786-O, RCJ-41T2, A549, and MIA PaCa2) or at 5.0×10^3 cells/well (MDA-MB-231) in phenol-red free 10% RPMI 1640 (786-O) or 10% DMEM (RCJ-41T2, MDA-MB-231, A549, and MIA PaCa2) in 96 well plates. Adhered cells were incubated with two-fold dilutions of SBI-183 starting at 20 μ M, or vehicle (.4% DMSO) for five days. Cell growth was determined at days 1, 3, and 5 in an MTT assay (Molecular Probes) following the manufacturer's directions.

Trans-well Invasion Assay

1.0×10^5 786-O, RCJ-41T2, MDA-MB-231, and A549 or 5.0×10^4 MIA PaCa2 cells were seeded in triplicate onto Matrigel-coated 24-well invasion 8 μ m pore-size

inserts (Corning) in serum-free media. Cells were allowed to adhere for 30 minutes prior to the addition of DMSO or SBI-183 giving a final concentration in the well of .2% DMSO vehicle or 20 μ M SBI-183. Inserts were incubated for 4-5 hours (786-O, RCJ-41T2, MDA-MB-231, and A549) or overnight (MIA PaCa2) at 37°C. Non-invading cells were removed, membranes were fixed in ice cold 100% methanol, and mounted on slides with DAPI (Vector Laboratories). Three unique fields were captured using the 4x objective and then automatically counted on a Cytation 5 microscope (BioTek). Images were edited using ImageJ.

3D Spheroid Invasion Assay

The following protocol was performed as described in Vinci *et al*, (2015) with slight modifications as stated (175). 786-O and RCJ-41T2 were seeded in triplicate at 1.25×10^3 cells/well in 200 μ L 10% RPMI 1640 or 5-10% DMEM respectively in Ultra Low Attachment (ULA) 96 well plates (Corning). MDA-MB-231, A549, and MIA PaCa2 were seeded at 1.25×10^3 - 2.5×10^3 cells/well in 5-10% DMEM. Plates were centrifuged at 1000xg for 3 minutes then incubated and allowed to form spheroids for 3 days. Plates were chilled to 4°C for 20 minutes and all but 50 μ L of media was removed. On ice, 50 μ L of Matrigel Matrix (Corning) was added. Plates were centrifuged at 300xg for 3 minutes at 4°C, then incubated for 1 hour at 37°C. Each well contained the following final concentrations of SBI-183 in complete media: 20 μ M, 10 μ M, 5 μ M, 2.5 μ M, or .4% DMSO vehicle. Cells were imaged on days 0, 2, 4, 6 (RCJ-41T2 and MDA-MB-231), and 8 (786-O). Invasion was quantified with ImageJ as total area of invaded cells. Subsequent experiments with SBI-183 analogs were initially screened at 1.25 μ M compound or .01% DMSO vehicle, final concentration. Compounds which had anti-

invasive properties were further screened at the following final concentrations: 1.25 μM , .625 μM , .3125 μM , .156 μM , or .01% DMSO vehicle control. Cells were imaged on day 0, 1, and 3, depending on cell line.

Rescue invasions were performed as stated above with the following modifications. To the 50 μL of media remaining in the wells, 50 μL of media containing either PBS or rQSOX1, and SBI-183 or DMSO was added. Final concentrations in the well were 2.5 μM SBI-183 and 5 μM rQSOX1 or .025% DMSO (786-O), 5 μM SBI-183 and 5 μM rQSOX1 or .05% DMSO (RCJ-41T2), and 2.5 μM SBI-183 and 2.5 μM rQSOX1 or .025% DMSO (MDA-MB-231). Matrigel was added as above at a 1:1 dilution.

Subsequent rescue invasions with SPX-009 were performed on MDA-MB-231, MIA PaCa2, and RCJ-41T2. The final concentrations in the well were .3125 μM SPX-009 and .625 μM – 1.25 μM rQSOX1 (cell line dependent).

Tyrosine kinase inhibitor profile

The “Other-2” Kinase Selectivity Profiling System and the accompanying ADP-Glo Assay were purchased from Promega (V6927) to assay eight kinases to determine possible off-target effects of SBI-183. Assay was performed in a white-bottom, 384 well plate (Corning). SBI-183 was assayed at 5 μM (a concentration at which all cell lines exhibited significant reduction in proliferation and invasion) in duplicate, following the manufacturers instructions. Luminescence was acquired on a SpectraMax M3 (Molecular Devices).

Animal Studies

786-O: Fox1^{nu/nu} mice were inoculated with 1.0×10^6 786-O cells in the right hind flank. Seven days post implant (study day 0) mice were dosed daily by oral gavage with 400 $\mu\text{g}/\text{mouse}/\text{day}$ SBI-183 dissolved in 100% DMSO. Control mice received 100% DMSO. Tumor length and width measurements were obtained using Vernier calipers.

RCJ-41T2: A part of RCJ-41T2 tumor was minced with a sterilized blade to slurry and mixed with equal volume of Matrigel. 100 μL of the resulting mixture was injected subcutaneously into 8-10 week old male NSG mice using 1 ml syringes equipped with a 16-gauge needle. When the tumor grew to approximately 1500 mm^3 , mice were sacrificed, the tumors were harvested and reimplanted into 18, male NSG mice as described above. When the average size of the tumors was $\sim 100 \text{ mm}^3$, mice were randomized into two groups: i) Vehicle: 20% DMSO + 80% PEG-400, gavage daily, ii) SBI-183, 100 mg/kg dissolved in the vehicle, oral gavage daily. Treatment was continued for 3 weeks. Then, mice were euthanized, and tumors and organs were harvested for further analysis.

MDA-MB-231-Luc: Twenty-four female CB.17 SCID mice aged 8 weeks were obtained from Charles River. Mice were inoculated with .1 mL of 50% Matrigel/50% Media containing 5×10^6 MDA-MB-231-Luc cells (Cell Biolabs) into the mammary fat pad. Seven days post implant (study day 1) daily oral administration of 100 mg/kg (n = 12) SBI-183 or vehicle control (n = 12) began. Primary endpoint was assessment of treatment effects on spontaneous distal lung metastases determined by ex-vivo bioluminescence imaging. SBI-183 was dissolved in DMA (10% total volume)/PEG400 (90% total volume). Stock solution was made fresh weekly and stored at -20°C .

Immunohistochemistry

RCJ-41T2 xenograft tumors from mice were mounted in paraffin on slides. Slides were deparaffinized, rehydrated, and then the antigen was retrieved with citrate buffer (pH 6.0, 125°C for 1 minute). Slides were incubated in 3% H₂O₂ for 10 minutes at room temperature. Rabbit anti-laminin α 4 antibody (Novus Biologicals) was added at 1:300 and incubated at 4°C overnight. HRP conjugated anti-rabbit secondary antibody (Vector Laboratories) was added and incubated for 30 minutes at room temperature. 3,3'-Diaminobenzidine (DAB) was used as the chromogen with Hematoxylin counter staining.

Three unique images from each of two tumors per group were obtained using the 10x objective on an Olympus BX51 microscope. DAB intensity was measured using Fiji (176).

Immunofluorescence

Cells grown on coverslips: Coverslips were coated for 1 hour with 50 μ g/mL collagen (Advanced BioMatrix) in .01 M HCl. Collagen was aspirated, coverslips were rinsed with PBS, and allowed to air dry under UV radiation for at least 30 minutes. Cells were plated in 500 μ L complete media at 2.5×10^4 cells/well in duplicate and allowed to adhere overnight. The next day, 2X DMSO and SBI-183 were added to give a final concentration per well of .2% DMSO and 20 μ M SBI-183. Cells were incubated for 24 hours. Cells were fixed in 4% formaldehyde for 10 minutes at 4°C and rinsed 3x with 1X PBS. Cells were permeabilized in .1% Triton X-100 in 1X TBS and incubated for 10 minutes at 4°C and rinsed 3x with 1X TBS. Blocking was performed using 2% BSA in 1X TBS-Tween (TBS-T) at room temperature for 30 minutes. Blocking buffer was

removed and monoclonal laminin α 4 antibody (R&D Systems) was added at 8 μ g/mL in blocking buffer and incubated for 2 hours at room temperature. Cells were rinsed 3x with TBS-T. AlexaFluor 488 goat anti-mouse IgG (Invitrogen) was added in blocking buffer at 1 μ g/mL and incubated for 45 minutes at room temperature protected from light. Cells were rinsed 2x with TBS-T, 1x with TBS, mounted in Prolong Gold Antifade + DAPI Mountant (Invitrogen), and imaged using the 63X oil objective on a Zeiss LSM 800 confocal microscope. Arithmetic mean intensity was quantified using Zen software (blue edition).

For 3D spheroids: 3D spheroids were plated as stated above and allowed to invade for 7 days. On the seventh day, spheroids in Matrigel were harvested, mounted in HistoGel (Thermo Fisher Scientific), fixed in 10% formalin, and mounted in paraffin on slides. Slides were deparaffinized, rehydrated, and then the antigen was retrieved with citrate buffer (pH 6.0). Slides were blocked in 10% Goat Serum (Invitrogen) (for primary antibodies against laminin α 4, nidogen, and fibronectin) or 2.5% horse serum (for primary antibody against versican) (Vector Laboratories). Primary antibody was added as follows: laminin α 4 at 10 μ g/mL (MAB7340, R&D Systems), nidogen at 10 μ g/mL (MAB2570, R&D Systems), fibronectin at 5 μ g/mL (MAB1918, R&D Systems), and versican at 10 μ g/mL (AF3054, R&D Systems). Primary antibodies were incubated for 1 hour at room temperature. Primary antibody was removed with three PBS washes, five minutes each. Secondary incubation was as follows: 1X Alexa Fluor 488 Phalloidin (Invitrogen) and Donkey α Mouse Alexa Fluor 647 (laminin α 4, nidogen, fibronectin) (Molecular Probes) or Donkey α Goat Alexa Fluor 647 (versican) (Invitrogen) at a 1:5000 dilution. Secondary antibody was incubated at room temperature in the dark for

one hour, followed by three PBS washes, five minutes each. Slides were mounted in ProLong Gold Antifade Mountant with DAPI (Invitrogen) and imaged using the 63X oil objective on a Zeiss LSM 800 confocal microscope. Treated and control cells were imaged at the same exposure. Mean intensity was quantified using Zen software (blue edition).

Statistical Analysis

Unless otherwise noted, all statistical analyses were performed using GraphPad Prism version 7.04 or 8 for Windows, GraphPad Software, La Jolla California USA, www.graphpad.com.

CHAPTER 3

MOLECULAR INHIBITOR OF QSOX1 SUPPRESSES TUMOR GROWTH IN VIVO

Fifield AL, Hanavan PD, Faigel DO, Sergienko E, Bobkov A, Meurice N, et al. Molecular Inhibitor of QSOX1 Suppresses Tumor Growth in vivo. *Mol Cancer Ther* [Internet]. 2019 Jan 1;molcanther.0233.2019. Available from: <http://mct.aacrjournals.org/content/early/2019/10/01/1535-7163.MCT-19-0233.abstract>

Overview:

Quiescin Sulphydryl Oxidase 1 (QSOX1) is an enzyme overexpressed by many different tumor types. QSOX1 catalyzes the formation of disulfide bonds in proteins. Since short hairpin knockdowns of QSOX1 have been shown to suppress tumor growth and invasion *in vitro* and *in vivo*, we hypothesized that chemical compounds inhibiting QSOX1 enzymatic activity would also suppress tumor growth, invasion, and metastasis. High throughput screening using a QSOX1-based enzymatic assay revealed multiple potential QSOX1 inhibitors. One of the inhibitors, known as “SBI-183”, suppresses tumor cell growth in a Matrigel-based spheroid assay and inhibits invasion in a modified Boyden chamber, but does not affect viability of non-malignant cells. Oral administration of SBI-183 inhibits tumor growth in two independent human xenograft mouse models of renal cell carcinoma. We conclude that SBI-183 warrants further exploration as a useful tool for understanding QSOX1 biology and as a potential novel anticancer agent in tumors that overexpress QSOX1.

Results:

SBI-183 inhibits QSOX1 enzymatic activity in vitro

SBI-183 emerged as a QSOX1 inhibitor from cell-free high throughput screening assays described previously (1). As shown in Figure 1A, SBI-183 inhibits rQSOX1 in a

dose-dependent manner in a fluorescence assay developed by Raje *et al.*(131). H₂O₂ produced by QSOX1 activity activates HRP to dimerize HVA resulting in fluorescence at 420 nm. The first bar in Figure 1A demonstrates that SBI-183 does not inhibit HRP, nor does it appear to scavenge H₂O₂, providing confidence that the target of SBI-183 is QSOX1.

SBI-183 binds to QSOX1 by Microscale Thermophoresis (MST)

Since SBI-183 appeared to inhibit the enzymatic activity of QSOX1, we wanted to determine if it bound to QSOX1. MST was performed in duplicate showing binding of SBI-183 to QSOX1 at a K_d of 20 μM (Figure 1B).

Computer modeling predicting binding location of SBI-183 with QSOX1 in silico

Since crystal structures of QSOX1 have been generated (135) and SBI-183 appeared to bind QSOX1, computer modeling was performed predicting the binding location of SBI-183. From a SiteFinder search, two sites (Site 1 and Site 2) were identified as possible binding locations on QSOX1, however Site 1 was optimal for SBI-183 binding (Figure 1C). Table 1 displays the results from our docking protocols. At Site 1, SBI-183 fits deep into a wedge-like crevice inside QSOX1 that includes the following residues within 6Å of SBI-183: C237, Y238, L239, V251, L252, M253, F258, Y259, Y262, and L263. Interaction pairs are formed between SBI-183 and QSOX1 with frequent ring-ring pi-clouds, H-bonds and charge-charge interactions participating in electrostatic interactions with the backbone carbonyls and hydroxyl residues, and transient pi-cloud interactions occurring with the phenyl-substituted Tyrosine rings (Figure 1D).

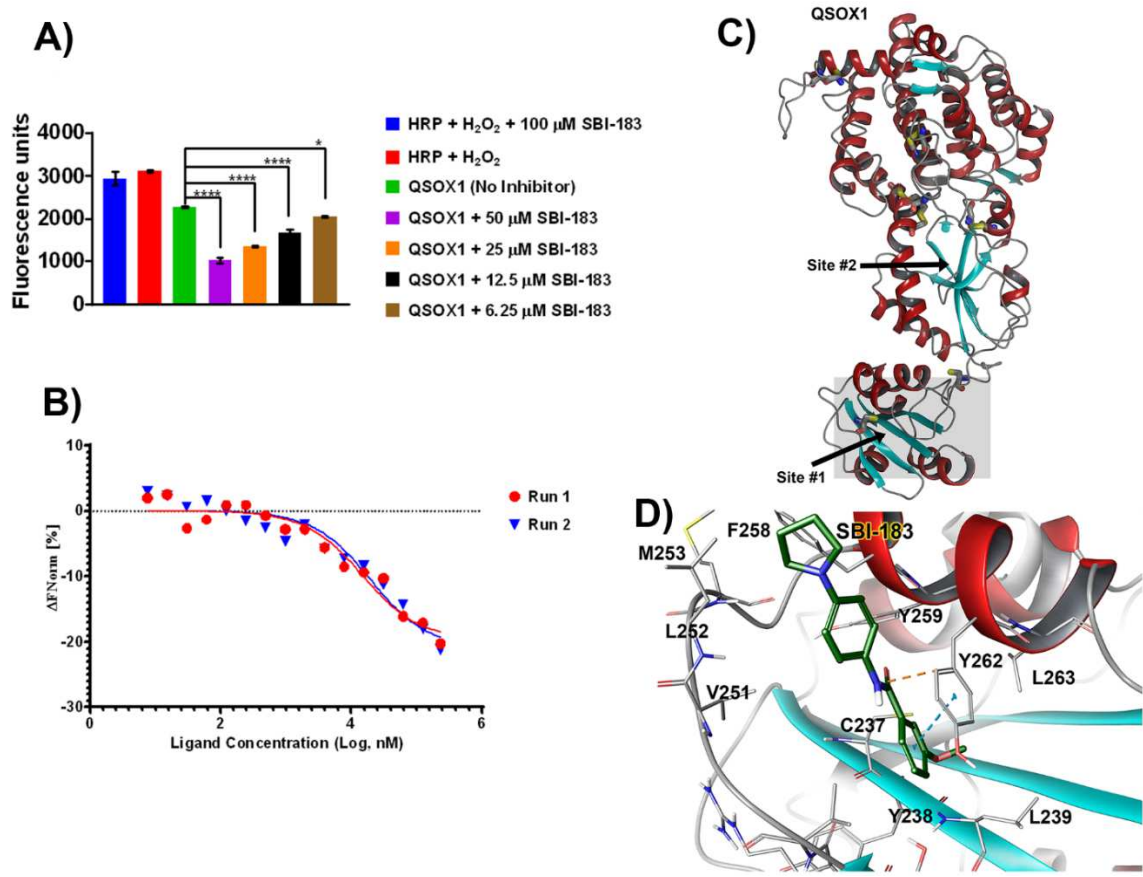


Figure 1. SBI-183 binds to and inhibits the enzymatic activity of QSOX1. A) Data were recorded in triplicate at time = 15 minutes (steady state) after addition of DTT substrate. Error represents SEM. Significance was determined by two-way ANOVA and * $p < .05$, *** $p < .0001$. B) MST titrations of rQSOX1 with SBI-183. Red and blue data sets represent two independent titrations of 50 nM Dylight650-labeled QSOX1 with increasing amounts of SBI-183 (.0076 to 250 μM). Fitting the data yielded $K_d = 20 \pm 7$ μM. C) QSOX1 is shown with predicted binding Sites 1 and 2 indicated by arrows. The boxed gray area for Site 1 is where SBI-183 was shown to bind and is zoomed into for panel D. Atom colors are by atom type (C-gray, N-blue, O-red, S-yellow, H-white) and ribbons are colored by secondary structure (red-helix, cyan-sheet, gray-random coil/loop). D) SBI-183 docked with QSOX1 is given. Key interacting residues within 6Å cutoff are labeled and shown in licorice stick rendering. Dashed lines indicating hydrogen bonds, pi-cloud interactions, or electrostatics are shown.

SBI-183 suppresses tumor cell growth in vitro

To determine if SBI-183 targets QSOX1 in tumor cells, we selected cell lines that were previously identified to express QSOX1. The ability of SBI-183 to inhibit viability

of tumor cells in a dose-dependent fashion was determined using the CellTiter Glo assay (Figure 11). Cells were treated with 2-fold dilutions of SBI-183 between 40 μ M and .076 nM (in triplicate), incubated for 72 hours and analyzed. As shown in Figure 11, inhibition of viability was observed for 786-O, RCJ-41T2, and MDA-MB-231 with IC₅₀'s of 4.6 μ M, 3.9 μ M, and 2.4 μ M respectively.

Because previous studies demonstrated reduced proliferation of tumor cells when QSOX1 was knocked down (KD) using shRNA (139,146,151), we hypothesized that a compound which inhibits QSOX1 would similarly decrease tumor growth *in vitro*. To test this, tumor cells were cultured for 5 days in the presence of SBI-183 or .4% DMSO vehicle control. An SBI-183 concentration-dependent reduction in cell growth was observed for each tumor cell line (Figure 2A-E). To determine if SBI-183 demonstrated selectivity for tumor cells, non-malignant adherent human fibroblasts and non-adherent PHA-stimulated PBMC from healthy human donors were incubated with SBI-183 for 5 days under the same conditions. No significant inhibition of cell growth was observed compared to vehicle control (Figure 2G & H). Table 2 lists percent growth for Figure 2A-D.

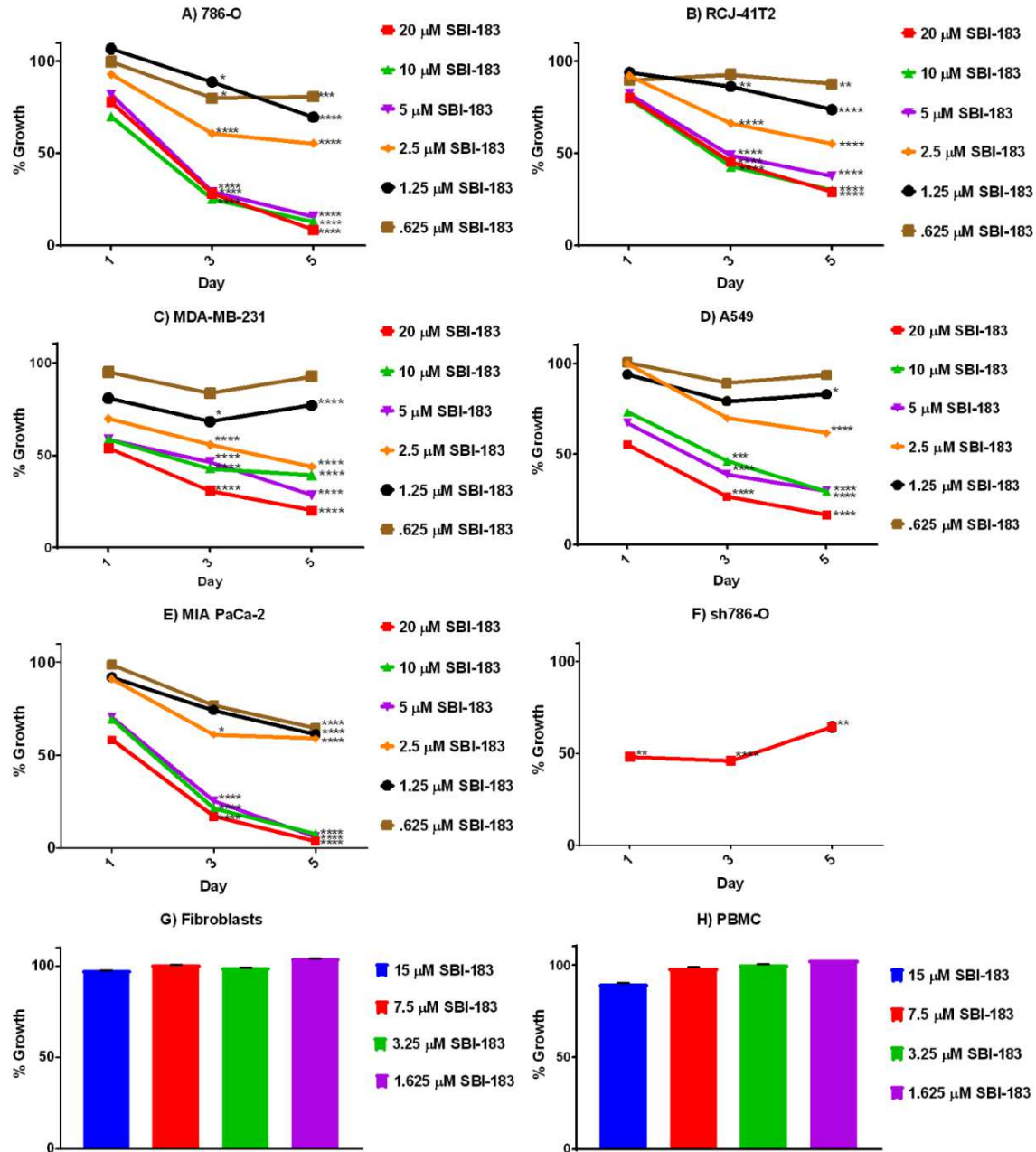


Figure 2. SBI-183 inhibits proliferation of tumor cells, but does not kill fibroblasts or rapidly proliferating PBMC. Inhibition of proliferation of A) 786-O, B) RCJ-41T2, C) MDA-MB-231, D) A549, and E) MIA PaCa2 with SBI-183 exhibits a dose response. This phenotype is similar to that seen in the QSOX1 stable KD cell line F) 786-O sh742.E11. Significance was determined by two-way ANOVA. No significant toxicity was observed when fibroblasts (G) or PHA-stimulated PBMC (H) were incubated with SBI-183 for 5 days. Significance was determined by one-way ANOVA, Kruskal-Wallis Test. Experiments were performed in triplicate and error represents SEM. Cells incubated with DMSO vehicle alone were used to calculate % growth with the following equation:

$((\text{Cells} + \text{SBI-183})/(\text{Cells} + .4\% \text{ DMSO})) \times 100$. % growth of QSOX1 sh742 KD was calculated against shScr and * $p < .05$, ** $p < .01$, *** $p < .001$, **** $p < .0001$.

SBI-183 inhibits tumor invasion in both 2D and 3D models

We previously reported that silencing QSOX1 expression with shRNA and inhibiting QSOX1 with the small molecule ebselen reduced the invasiveness of cancer cell lines *in vitro* (139,146,151). Similarly, we hypothesized that another small molecule inhibitor of QSOX1 would also suppress invasion. It is well known that 3D culture systems more closely recapitulate *in vivo* tumor phenotypes than 2D cultures. As seen *in vivo*, compounds may have difficulty diffusing to the center of a spheroid, or may be inhibited by hypoxia, leading to decreased efficacy, increased cellular survival, and reduced compound sensitivity (28–30). Therefore, in order to more closely mimic how naturally occurring tumors would be affected by SBI-183, we utilized a 3D invasion model. 786-O, RCJ-41T2, MDA-MB-231, A549, and MIA PaCa2 were grown as spheroids. After the addition of Matrigel, spheroids were imaged on the indicated days (Figure 3i, 3ii, 3iii, 3iv, and 3v). 786-O, RCJ-41T2, and A549 initially formed dense spheroids (Figure 3 panels C, F, & L) which expanded over the course of the experiment (Figure 3 panels A, D, & J). RCJ-41T2 formed wandering tendrils as it invaded the surrounding matrix (Figure 3 panel D). MDA-MB-231 and MIA PaCa2 initially formed loose, grape cluster-like spheroids (Figure 3 panel I & O). At the end of the experiment these clusters were greatly enlarged with projections from the main body, and single cells migrating from the spheroid (Figure 3 panel G & M). In each cell line tested, incubation with SBI-183 reduced invasion through Matrigel (Figure 3i, 3ii, 3iii, 3iv, and 3v panels B, E, H, K, N), similar to the reduction observed in QSOX1 stable KD cell line 786-O

sh742.E11 (Figure 3vi panel S). IC₅₀'s of 3D invasion were determined to be 1.5 μM for MDA-MB-231, 2.3 μM for MIA PaCa2, and 3.6 μM for RCJ-41T2 (Figure 12).

To ensure the observed decrease in invasion was not simply due to a decrease in proliferation due to the length of the 3D experiment, modified Boyden chamber invasion assays were also performed (Figure 3vii-xi). These invasion assays confirmed the 3D spheroid results.

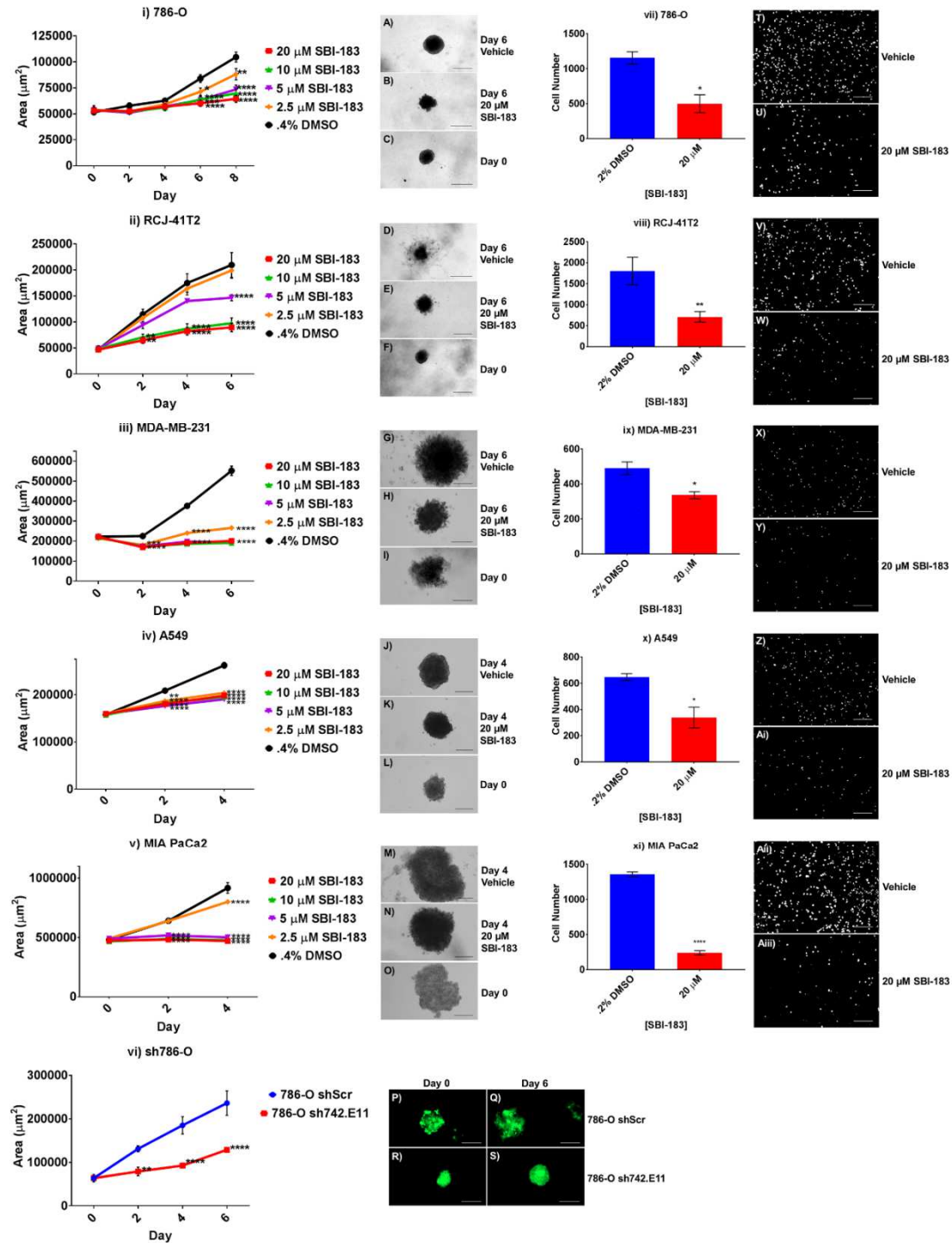


Figure 3. 3D & 2D Invasion of cells treated with SBI-183. Inhibition of invasion in 3D of (i) 786-O, (ii) RCJ-41T2, (iii) MDA-MB-231, (iv) A549, and (v) MIA PaCa2 exhibits a dose response relationship. This phenotype is similar to that seen in the QSOX1 stable KD cell line (vi) 786-O sh742.E11. Representative images of 3D invasion on day 0 (C, F,

I, L, O) and day 4 or day 6 (cell line dependent) with no compound (.4% DMSO vehicle only) (A, D, G, J, M), or 20 μ M SBI-183 (B, E, H, K, N). Images of 786-O cells transduced with GFP-expressing shRNA scramble (shScr) and QSOX1 KD (sh742.E11) on day 0 (P, R) or day 6 (Q, S). Data are representative of three experiments performed in triplicate. Scale bar = 300 μ m. 786-O sh742.E11 forms smaller spheroids than 786-O shScr. To account for this, 786-O shScr spheroids at all time points were normalized against 786-O sh742.E11 as follows:

(Calculated Area shScr) - (Average Area Day 0 shScr – Average Area Day 0 sh742.E11).

Invasion of all cell lines through a Matrigel coated membrane (2D) was significantly inhibited (vii, viii, ix, x, xi and T, U, V, W, X, Y, Z, Ai, Aii, Aiii)

Experiments were performed in triplicate. Error represents SEM. Significance was determined by two-way ANOVA and * $p < .05$, ** $p < .01$, *** $p < .001$, **** $p < .0001$.

SBI-183 reduces laminin α 4 deposition on cells.

QSOX1 has previously been shown to modulate deposition of laminin α 4 into the ECM (145). We hypothesized that inhibition of QSOX1 enzymatic activity with SBI-183 would similarly inhibit laminin α 4 deposition on cells grown *in vitro*. As seen in Figure 4, 24-hour incubation with 20 μ M SBI-183 resulted in decreased laminin α 4 deposition by immunofluorescence.

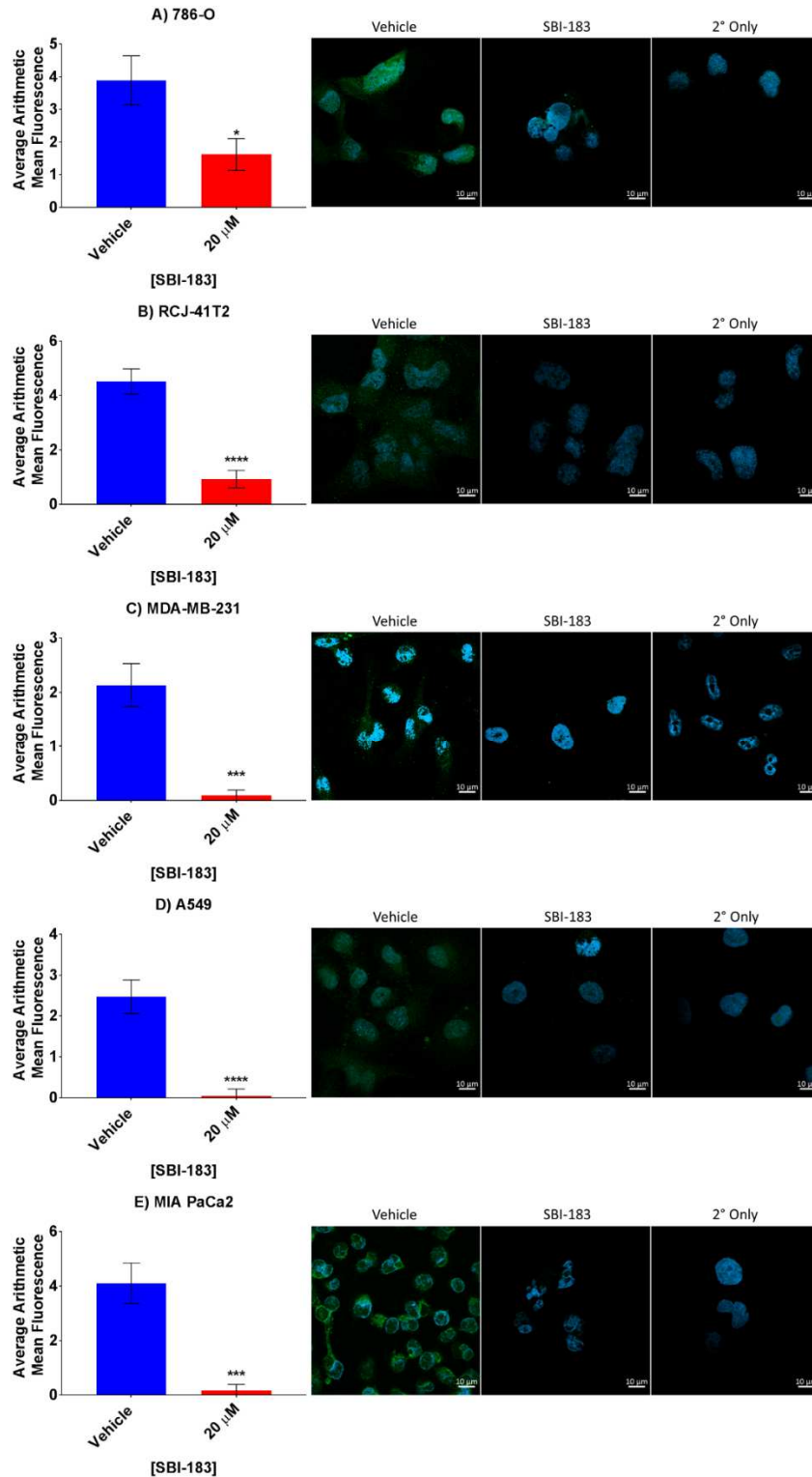


Figure 4. SBI-183 reduced deposition of laminin α 4 in tumor cell ECM by immunofluorescence. Treatment with SBI-183 resulted in a decrease of laminin α 4 deposition in the ECM of (A) 786-O, (B) RCJ-41T2, (C) MDA-MB-231, (D) A549, and

(E) MIA PaCa2 after 24 hours. Error bars represent SEM. Scale bars = 10 μ m. Significance was determined by one-way ANOVA and * $p < .05$, *** $p < .001$ **** $p < .0001$.

Exogenous addition of rQSOX1 partially rescues invasion induced by SBI-183

QSOX1 is overexpressed by tumor cells. It localizes to the Golgi and is secreted. Because SBI-183 inhibits the activity of QSOX1 resulting in a decrease in invasion, we added exogenous rQSOX1 to rescue the invasive phenotype (139,151). Addition of a 2-fold molar excess of rQSOX1:SBI183 to 786-O cells partially rescued invasion (Figure 5A). Addition of equimolar concentration of rQSOX1 partially rescued the invasive phenotype of both RCJ-41T2 cells (Figure 5B) and MDA-MB-231 cells (Figure 5C).

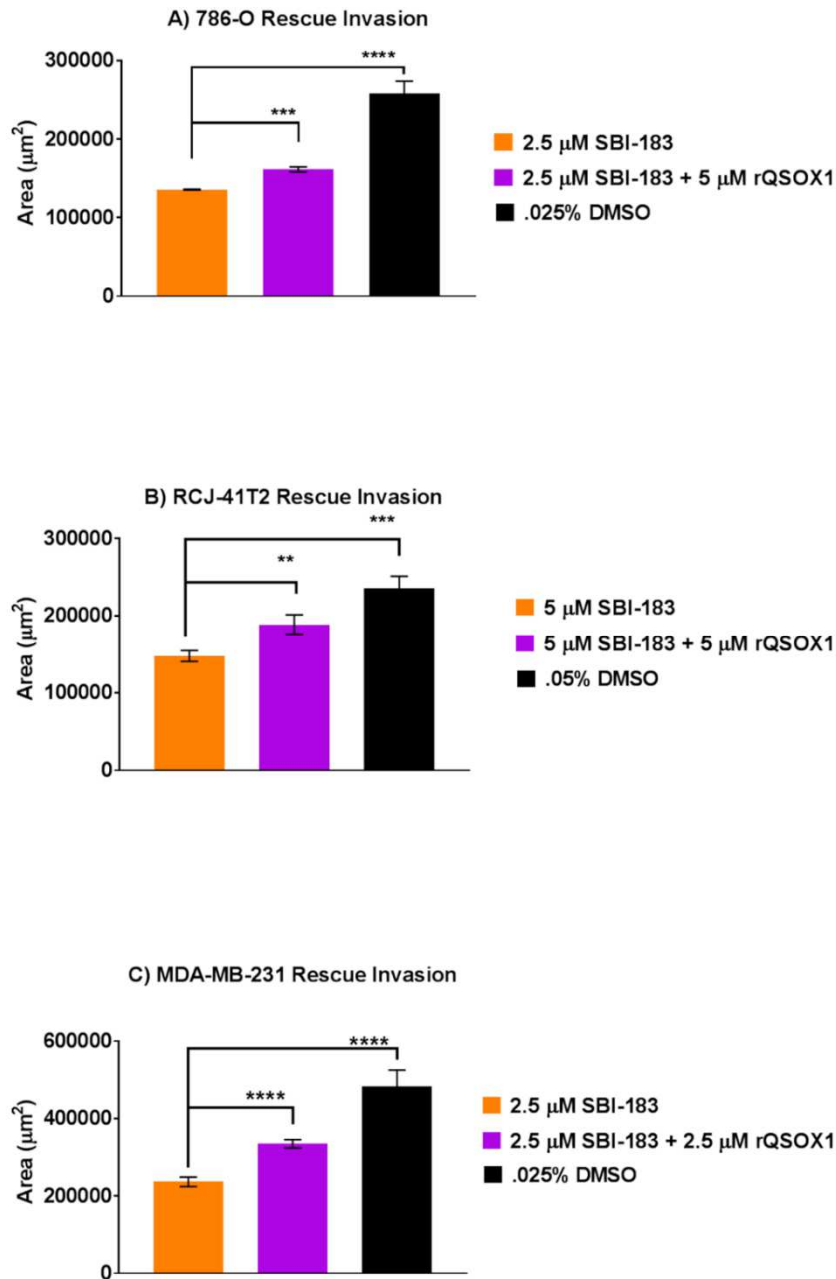


Figure 5. Partial rescue of invasive phenotype by addition of exogenous rQSOX1. Addition of 5 μM rQSOX1 increased invasion of 786-O (A) by 10% by day 6. By day 4, 5 μM rQSOX1 increased invasion of RCJ-41T2 (B) by 17% and increased invasion of MDA-MB-231 (C) by 20%. Experiment was performed in triplicate. Error represents SEM. Significance was determined by two-way ANOVA and ** $p < .01$, *** $p < .001$, **** $p < .0001$.

SBI-183 does not inhibit eight tested tyrosine kinase's.

Small molecules quite often interact with a number of targets within a cell (177). Because we observed statistically significant decreases in viability and invasion when cells were treated with SBI-183, we tested a panel of tyrosine kinases for inhibition of activity when in the presence of SBI-183. As seen in Figure 6, SBI-183 did not inhibit the activity of any of these potential cellular targets.

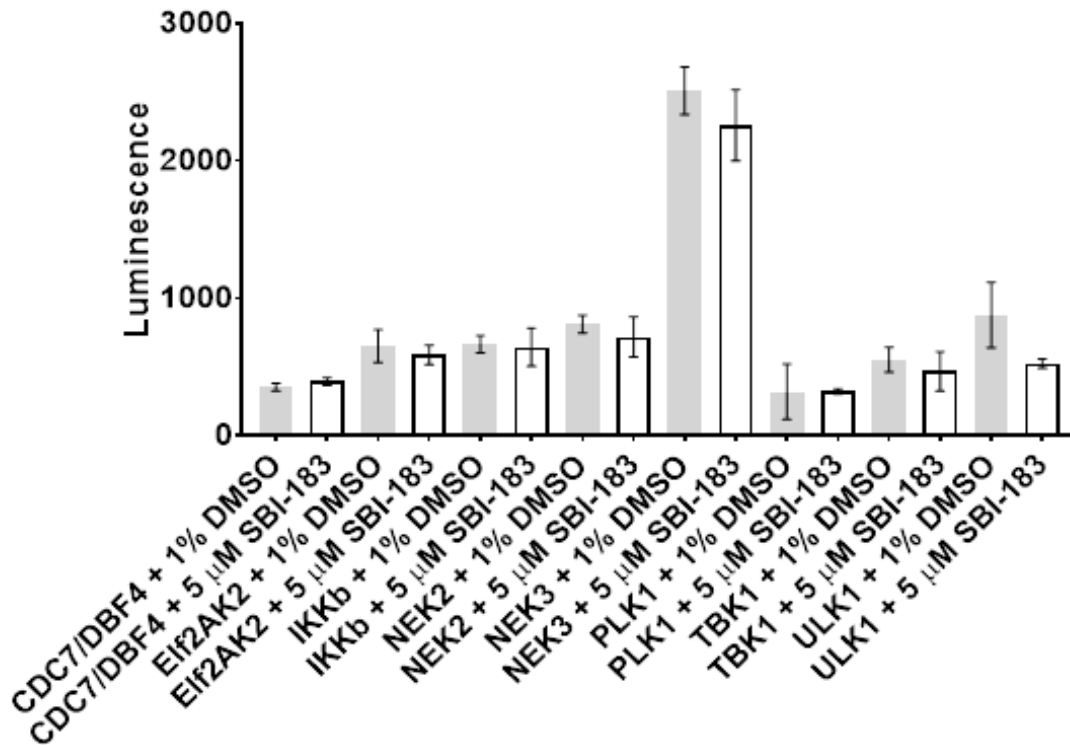


Figure 6. SBI-183 does not inhibit activity of eight tested tyrosine kinases. The eight tested kinases showed no inhibition of activity when treated with SBI-183. Significance was determined using Welch's t-test.

SBI-183 inhibits tumor growth of 786-O in-vivo

Since SBI-183 inhibits invasion *in vitro*, we tested the activity of SBI-183 in two independent RCC mouse xenografts. Tumor measurements were obtained at the intervals indicated in Figure 7. One mouse from the test group was terminated according to IACUC protocol on day 21. At the end of the experiment (day 41), SBI-183-treated 786-O xenografts had average tumor volumes that were 86% smaller than vehicle-treated mice. These results indicate that SBI-183 inhibits the growth of a RCC tumor cell line *in vivo*.

SBI-183 inhibits tumor growth of RCJ-41T2 in-vivo

Sarcomatoid RCC is associated with an aggressive, mesenchymal phenotype, and is intrinsically resistant to antiangiogenic therapy. To extend our findings to a sarcomatoid RCC line recently derived from a patient, 18 NSG mice were inoculated with minced RCJ-41T2 tumors obtained from patient-derived xenografts in 50% Matrigel and tumors were established for 10 days prior to dosage with 100 mg/kg SBI-183 or vehicle control. Data are from 9 control mice and 6 experimental mice (3 mice were lost in the experimental group due to an oral gavage problem, not due to the compound). Tumor volume was measured every seven days with calipers and volume was calculated using the following formula: Tumor volume = $.5 \times a \times b^2$ where a and b are the longest and shortest diameters respectively. Over the course of the experiment, treatment with SBI-183 resulted in an average 51% tumor volume reduction compared to control (Figure

7). No differences were observed in the overall body weight. These data suggest that SBI-183 inhibits the growth of a highly aggressive sarcomatoid RCC *in vivo*.

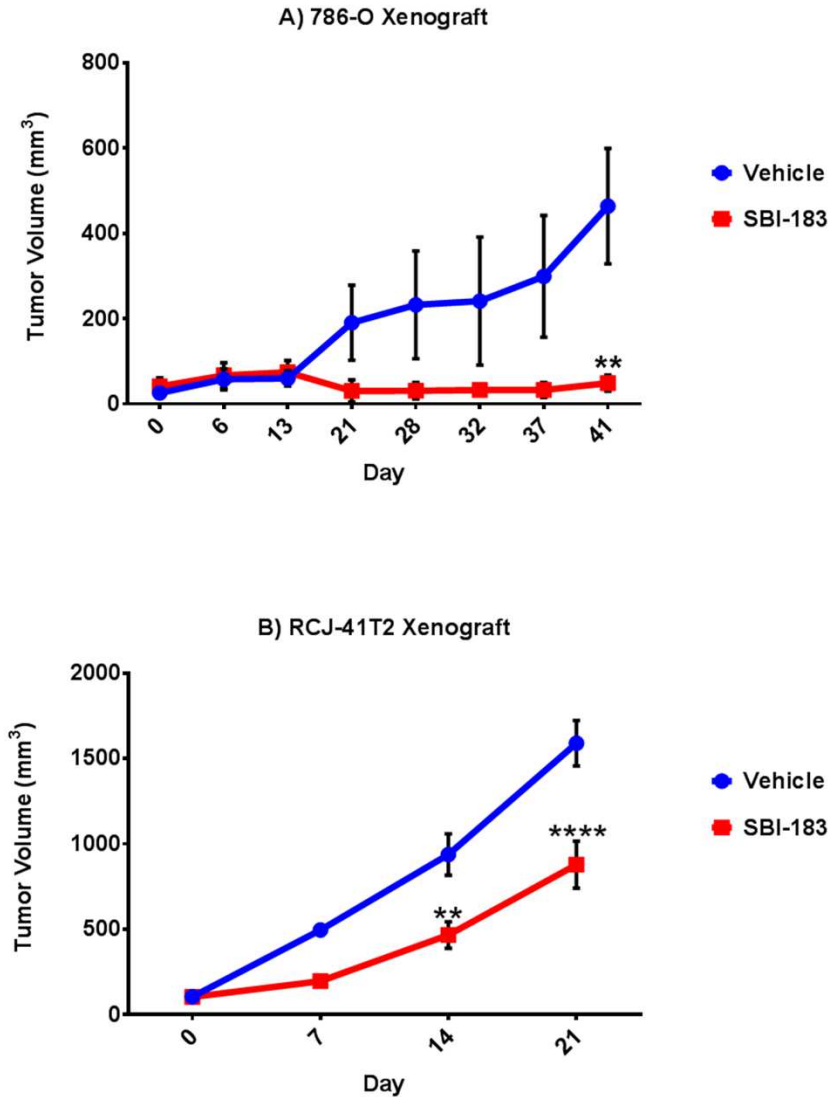


Figure 7. Treatment with SBI-183 suppresses 786-O and RCJ-41T2 growth in mice. A) 786-O cells were subcutaneously injected into 4 nude mice per group and tumors were established before initiation of daily oral gavage of 400 $\mu\text{g}/\text{mouse}/\text{day}$ SBI-183 or DMSO vehicle. Percentage of decrease was calculated with the following formula: $100 - ((\text{Average SBI-183})/(\text{Average Vehicle})) \times 100$. B) Daily treatment with SBI-183 suppresses RCJ-41T2 growth in NSG mice. Data are from 9 control mice and 6 experimental mice. Percentage decrease was calculated as above. Error bars represent SEM. Significance was determined by two-way ANOVA and $**p < .01$, $****p < .0001$.

SBI-183 reduces laminin α 4 deposition in RCJ-41T2 mouse xenografts

Because QSOX1 has previously been shown to be involved in the deposition of laminin α 4 in the ECM (145), we hypothesized that laminin α 4 deposition would be reduced in xenograft tumors from mice treated with SBI-183. DAB staining intensity due to laminin α 4 deposition was shown to be significantly reduced in SBI-183 treated mice compared to vehicle control (Figure 8).



Figure 8. Treatment with SBI-183 reduced laminin α 4 deposition in RCJ-41T2 mouse xenografts. DAB staining intensity (Log OD) due to laminin α 4 deposition was $.115 \pm .022$ for vehicle treated mice and $.088 \pm .008$ for SBI-183 treated mice ($p=.0101$). Optical density (OD) was estimated from three unique images from each of two tumors per group with the following formula: $OD = \text{Log}(\text{max intensity}/\text{mean intensity})$, where max intensity = 255 (178). Error represents SEM and was calculated in Microsoft Excel. Scale bar = 50 μm . Significance was determined using Welch's t-test.

Conclusions:

Despite systemic therapy, distant metastases are the major cause of cancer mortality. QSOX1 secreted from tumor and stromal cells is involved in ECM formation including laminin and fibronectin deposition (145,147), and post-translational activation of MMPs (146). Taken together, QSOX1 plays an important role in ECM-mediated

invasive processes. Since tumor-stroma-derived ECM is crucial for metastasis, targeting a potential master regulator of the ECM such as QSOX1 may affect multiple ECM proteins involved in invasion and metastasis. There are several lines of evidence supporting QSOX1 as a potential therapeutic target. First, QSOX1 is overexpressed in several malignancies (146,153–155,179) and is an indicator of poor relapse free and overall survival in luminal B breast cancer (150–152). Second, enzymatic inhibition of QSOX1 using either small molecules or Mabs interferes with ECM deposition and reduces tumor invasion (139,145,147). Since shRNA silencing of QSOX1 previously demonstrated suppression of tumor growth and the invasive phenotype (139,151), we embarked on a screening strategy to identify chemical probes to examine the effects of QSOX1 inhibition *in vitro* and *in vivo*. We demonstrate that the small molecule, SBI-183, (i) inhibits QSOX1 enzymatic activity *in vitro*, (ii) binds to QSOX1, (iii) inhibits tumor cell growth and invasion *in vitro*, and (iv) reduces tumor size in two independent mouse models.

We employed an enzymatic assay developed by Colin Thorpe's group (131) to screen for QSOX1 inhibitors in a library of ~50,000 compounds. SBI-183 was identified as a lead compound for the inhibition of QSOX1 enzymatic activity (Figure 1A). We previously reported that ebselen bound covalently to QSOX1 by LC-MS/MS analysis (139), but SBI-183 does not appear to bind covalently to QSOX1. Another measure of binding is MST which measures the motion of proteins along microscopic temperature gradients and is affected by changes in protein hydration, charge, and size originating from ligand binding. Incubation of serial dilutions of SBI-183 with QSOX1 demonstrated a temperature shift indicative of binding (Figure 1B). This physical interaction between

QSOX1 and SBI-183 supports computer models showing SBI-183 fitting into a crevice in QSOX1 at the C-terminal end of the second thioredoxin domain. The strong docking score via the SBI-183 benzyl-moiety and the tyrosine ring at Y262, along with the SBI-183 carbonyl oxygen electrostatic interactions at the nearby tyrosines (Y259, Y262) and various van der Waals interactions on the hydrophobic residues (V251, M253, L252, F258) with the alkane atoms of SBI-183 creates a solid anchored position for SBI-183 on QSOX1. Additionally, the area of interaction includes C237 within 6Å of SBI-183 binding (Figure 1D). C237 is one of two cysteines that covalently bound ebselen in our previous study (139). It is thought that C237 is not involved in QSOX1 enzymatic activity (129), however, it is interesting that two compounds which inhibit QSOX1 interact with it in this location. These data suggest that this region may be important for QSOX1 activity.

In addition to metastatic processes, the ECM is involved in signaling. SBI-183 suppressed growth in each tumor cell line tested in a concentration-dependent manner (Figure 2A-E), but no significant reduction in growth of fibroblasts or PHA-stimulated PBMC was observed (Figure 2G-H). This finding agrees with previously published immunohistochemistry results in a tumor tissue biopsy that show no QSOX1 protein expression in non-malignant tissue or infiltrating lymphocytes (123,140). Furthermore, Table 3 demonstrates that the maximal tolerated dose of SBI-183 in healthy nude mice is over 200 mg/kg and was limited by solubility of the compound, not toxicity. We do note, however, that SBI-183 has a high IC₅₀ in the tested cell lines (Figure 11). As such, while we did not observe inhibition of the tyrosine kinases we tested (Figure 6), it is still possible that there are other targets of SBI-183 *in vivo* that suppress tumor growth.

To further examine the cancer phenotype, we utilized a well-accepted model of 3D invasion of spheroids into Matrigel (175,180–182). Incubation with SBI-183 significantly reduced invasion in all five cell lines (Figure 3i-v). Our 3D results are consistent with reduced invasion observed in the trans-well invasion assay (Figure 3vii-xi). All invasion results are consistent with decreased invasion observed in cells stably expressing shRNA specific for QSOX1 (139,151), and could be at least partially due to a malformed ECM lacking laminin (as observed in Figure 4 and Figure 8), fibronectin (145,147), and reduced MMP-2 and MMP-9 activity (146). Furthermore, addition of exogenous rQSOX1 partially rescued SBI-183-induced invasion suppression observed in 786-O, RCJ-41T2, and MDA-MB-231 (Figure 5) (A549 and MIA PaCa2 were not tested). Rescue experiments are difficult to perform with small molecules because the small molecule can enter the cell while the target protein remains extracellular. A review of polypharmacology discusses that most drugs interact with five or more targets (177). In line with this, some VEGF tyrosine kinase inhibitors such as sunitinib, are known to also interact with other kinases (111). Similarly, while SBI-183 is active against QSOX1 (Figure 1A) it likely has various other targets in tumors, explaining why exogenous addition of rQSOX1 does not completely rescue the invasive phenotype. However, if QSOX1 is a master regulator of multiple disulfide-bonded proteins, even partial inhibition of QSOX1 may disrupt folding or proper association of proteins in the ECM.

To examine the *in vivo* effects of SBI-183 on tumor growth and metastasis, we inoculated mice with 786-O, RCJ-41T2 (Figure 7), and MDA-MB-231 (Figure 13). Mice bearing 786-O or RCJ-41T2 tumors that were treated with SBI-183 exhibited a statistically significant reduction in tumor volume compared to controls (Figure 7A & B).

Mice bearing the TNBC cell line MDA-MB-231-luc interestingly did not exhibit a reduction in primary tumor volume (Table 4) but rather exhibited a suppression of metastasis as evidenced by a reduction in mean lung radiance of 76% when compared to controls (Figure 13). This reduction, while striking, did not reach statistical significance, likely due to the death of two control mice. Our MDA-MB-231 *in vivo* data differs from our *in vitro* data in that SBI-183 slows tumor growth *in vitro*, but did not slow primary tumor growth in mice. However, MDA-MB-231 cells were inhibited from invading in the 3D spheroid and modified Boyden chamber models which are *in vitro* surrogates for metastasis. It should be noted that the effect of SBI-183 observed depends on the cell line tested, suggesting that cells depend differently on QSOX1 activity.

Our data show that both *in vitro* and *in vivo*, SBI-183 suppresses QSOX1 enzymatic activity which results in inhibition of tumor growth, invasion and possibly metastasis *in vivo*. Further, our data suggest that SBI-183 may be a useful tool to increase our understanding of the role of QSOX1 activity in the ECM of cancer and stromal cells during invasion and metastasis. Because metastasis is the main cause of death from cancer, even partial inhibition of this process may prolong patient survival. Finally, our study provides further evidence of QSOX1 as an anti-neoplastic target.

Chemical structure of SBI-183: $C_{18}H_{20}N_2O_2$

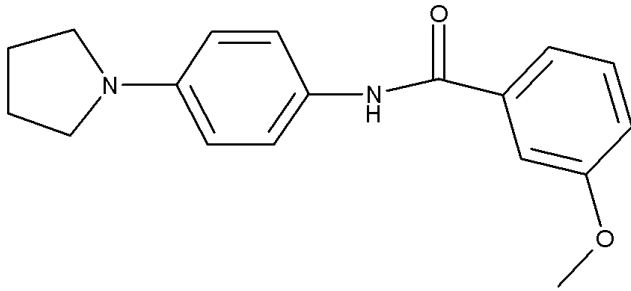


Figure 9. Chemical structure of SBI-183.

Verification of shRNA QSOX1 KD by qRT-PCR

Data are from three different experiments performed in triplicate and normalized against beta actin (ΔCt on the Y axis). Data are indicative of a 90% KD as indicated by the following formula: $(2^{-\Delta\Delta Ct}) = \text{fold change}$, then $(100 - (1/\text{fold change})) = \% \text{ KD}$.

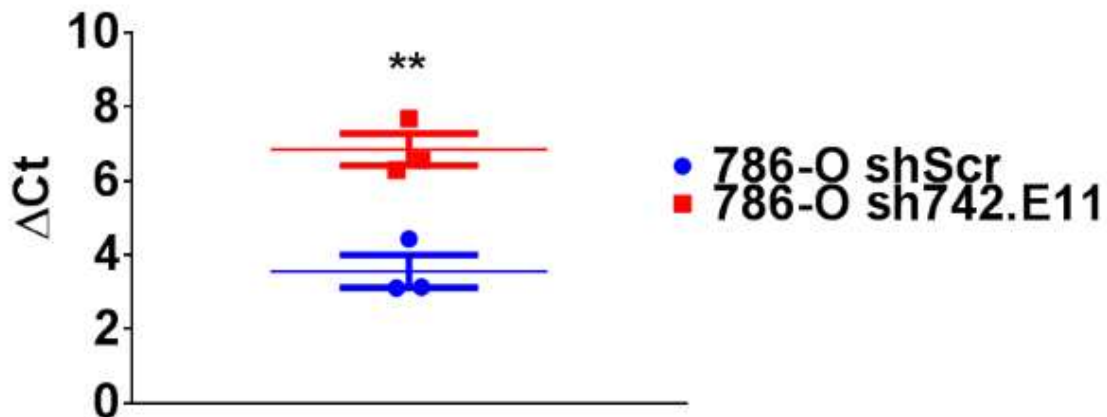


Figure 10. Stably transduced 786-O cells have reduced QSOX1 mRNA expression. Error represents SEM. Significance was determined by Welch's t-test. $**p < .01$.

Results from docking protocols

Compound	Rank	Docking Score	MW	Lipinski's Rule of 5 Violations	Total Polar Surface Area (Å ²)	Donor Hydrogen Bonds (possible)	Acceptor Hydrogen Bonds (possible)
SBI-183	2	-7.052	296.4	0	47.366	1	4

Table 1. Results from SBI-183 docking protocols.

Determination of IC₅₀'s by CellTiter Glo

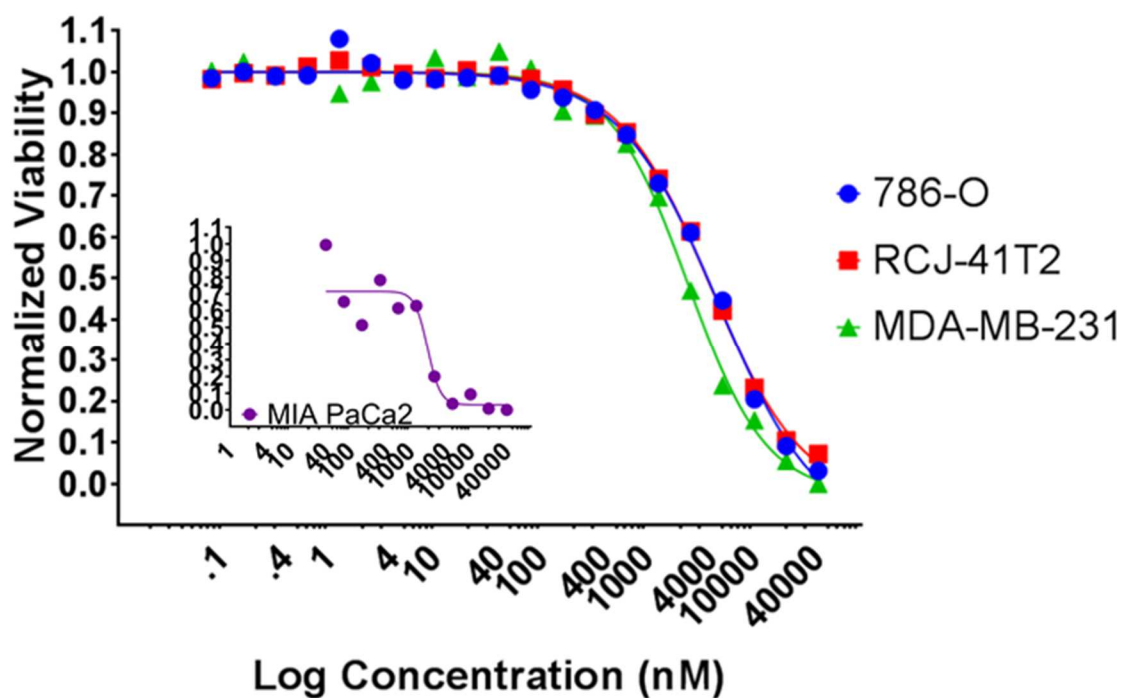


Figure 11. Viability Dose Response Curve. SBI-183 inhibits viability of RCC and TNBC with IC₅₀'s of 4.6 μM for 786-O, 3.9 μM for RCJ-41T2, and 2.4 μM for MDA-MB-231. Inset: Viability IC₅₀ determination for MIA PaCa2. MIA PaCa2 IC₅₀ was 1.9 μM and was determined using MTT. X axis = Log Concentration (nM), and Y axis = Normalized Viability. Data are also from 72 hours.

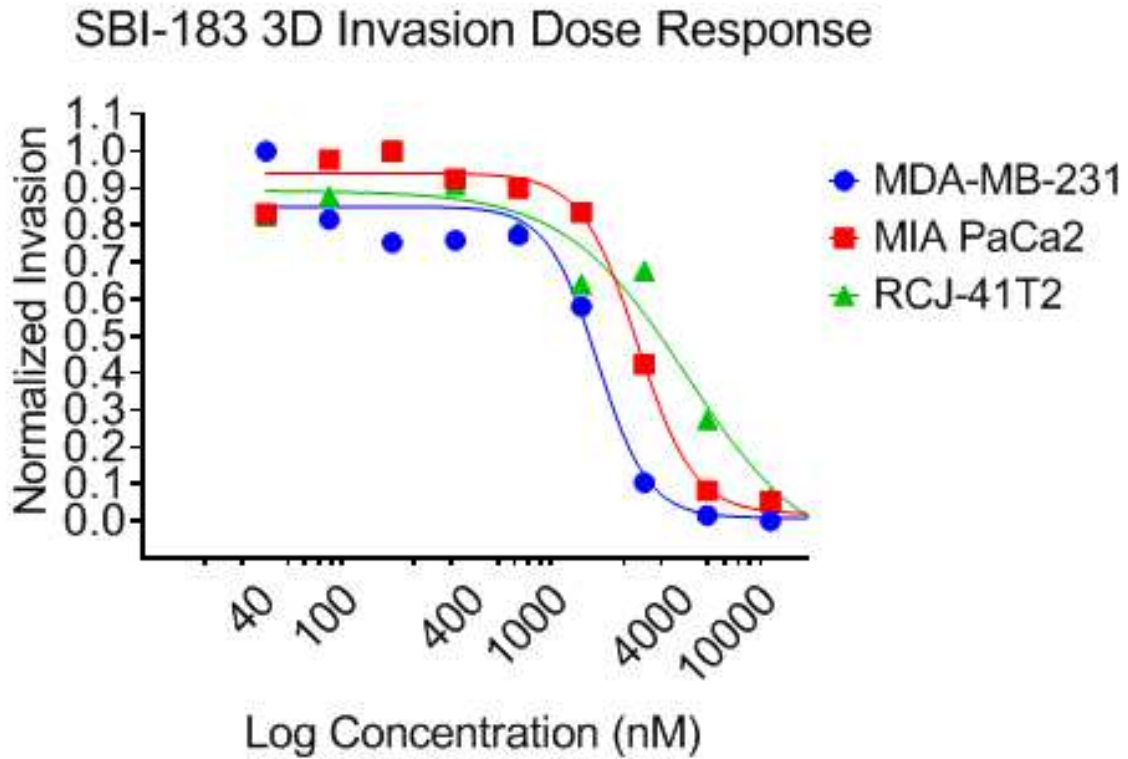


Figure 12. 3D invasion dose response curve for SBI-183. Cells were plated in replicates of six and dosed with two-fold dilutions of SBI-183 from 20 μM – 39.1 nM. Invasion area values from day 3 were normalized and GraphPad Prism was utilized to determine the IC₅₀'s. SBI-183 inhibits 3D invasion of TNBC, pancreatic cancer, and RCC with IC₅₀'s of 1.5 μM for MDA-MB-231, 2.3 μM for MIA PaCa2, and 3.6 μM for RCJ-41T2.

SBI-183 reduces proliferation

Cells were incubated with the indicated concentrations of SBI-183. The percent growth is indicated in the table below and is graphically represented in Figure 2.

Cell Line (Day 3)	20 μ M	10 μ M	5 μ M	2.5 μ M	1.25 μ M	.625 μ M	0 μ M
786-O	28%	28%	29%	61%	89%	91%	~
RCJ-41T2	45%	45%	49%	66%	86%	93%	~
MDA-MB-231	54%	56%	56%	58%	75%	84%	~
786-O sh742.E11	~	~	~	~	~	~	46%
Cell Line (Day 5)	20 μ M	10 μ M	5 μ M	2.5 μ M	1.25 μ M	.625 μ M	0 μ M
786-O	8%	13%	16%	55%	68%	81%	~
RCJ-41T2	29%	30%	38%	55%	73%	88%	~
MDA-MB-231	39%	31%	27%	42%	78%	99%	~
786-O sh742.E11	~	~	~	~	~	~	64%

Table 2. SBI-183 reduces proliferation. SBI-183 reduces proliferation of RCC and TNBC on days 3 and 5 at concentrations ranging from 20 μ M - .625 μ M.

SBI-183 is not toxic to athymic nude mice

Group	Frequency	Route	Pre-study Weight	Day 1 Weight	Day 2 Weight	Day 3 Weight
100mg/kg	Daily	Oral gavage	20.3 g	20.3 g	20.4 g	20.9 g
200mg/kg	Daily	Oral gavage	21.0 g	21.1 g	21.3 g	21.7 g

Table 3. SBI-183 is not toxic to athymic nude mice. SBI-183 solubilized in 10% dimethylacetamide (DMA) and 90% PEG400 was administered by oral gavage to 3 mice per group for 3 days. Neither 100 mg/kg, nor 200 mg/kg appeared to be toxic to athymic nude mice.

SBI-183 does not reduce primary tumor growth of MDA-MB-231 in vivo

Tumor growth was measured at the intervals indicated in Table 4. According to IACUC protocol, mouse 1 from the control group was humanely sacrificed on Day 25 due to tumor size. A second mouse (mouse 8) from the control group was found dead on Day 28.

Group		Tumor Volume (mm ³)												Median Tumor Volume (mm ³)
Day 1	0mg/kg	34	40	21	31	0	35	29	27	0	32	27	0	27.8
	100mg/kg	39	32	0	30	33	0	27	27	25	36	26	0	27.1
Day 13	0mg/kg	424	160	94	134	128	117	108	114	186	181	160	121	130.7
	100mg/kg	253	194	150	136	210	269	121	111	203	325	121	143	171.7
Day 28	0mg/kg	X	1514	790	875	841	883	1041	1012	1327	1320	1141	563	1012.2
	100mg/kg	1522	1405	1285	1352	1393	1908	1399	1244	1511	1970	1202	1995	1402.3

Table 4. SBI-183 does not reduce primary tumor growth of MDA-MB-231 *in vivo*. Daily treatment with SBI-183 (100 mg/kg) did not result in a decrease of primary tumor volume. Twelve mice per group were utilized for this experiment. X = moribund sacrifice.

SBI-183 inhibits metastasis of the triple negative breast cancer line MDA-MB-231.

MDA-MB-231 is a TNBC cell line that generates spontaneous lung metastases in mice after injection into the lymph nodes or mammary fat pad. Since our data suggests that QSOX1 plays a role in tumor-derived ECM and ECM genes are upregulated in metastases (183), we tested the activity of SBI-183 in a MDA-MB-231 TNBC mouse model. After luciferase expressing MDA-MB-231 tumors were established for 7 days, SBI-183 or vehicle control was orally administered to mice daily (100 mg/kg). Bioluminescence of lung metastases were quantified *ex vivo* upon termination of the experiment. In this metastatic model, there was no difference in primary tumor growth, but a 76% difference was observed in lung metastasis between vehicle and SBI-183-treated mice as measured by lung radiance (Figure 13). Additionally, on day 25 of the study, one mouse in the control group was moribund and humanely terminated, and another in the control group was found dead on day 28. These two mice were not analyzed for lung metastasis by mean lung radiance, but presumably died due to tumor growth. This result suggests that in the highly metastatic MDA-MB-231 model, SBI-183 suppresses lung metastasis of a triple negative breast cancer.

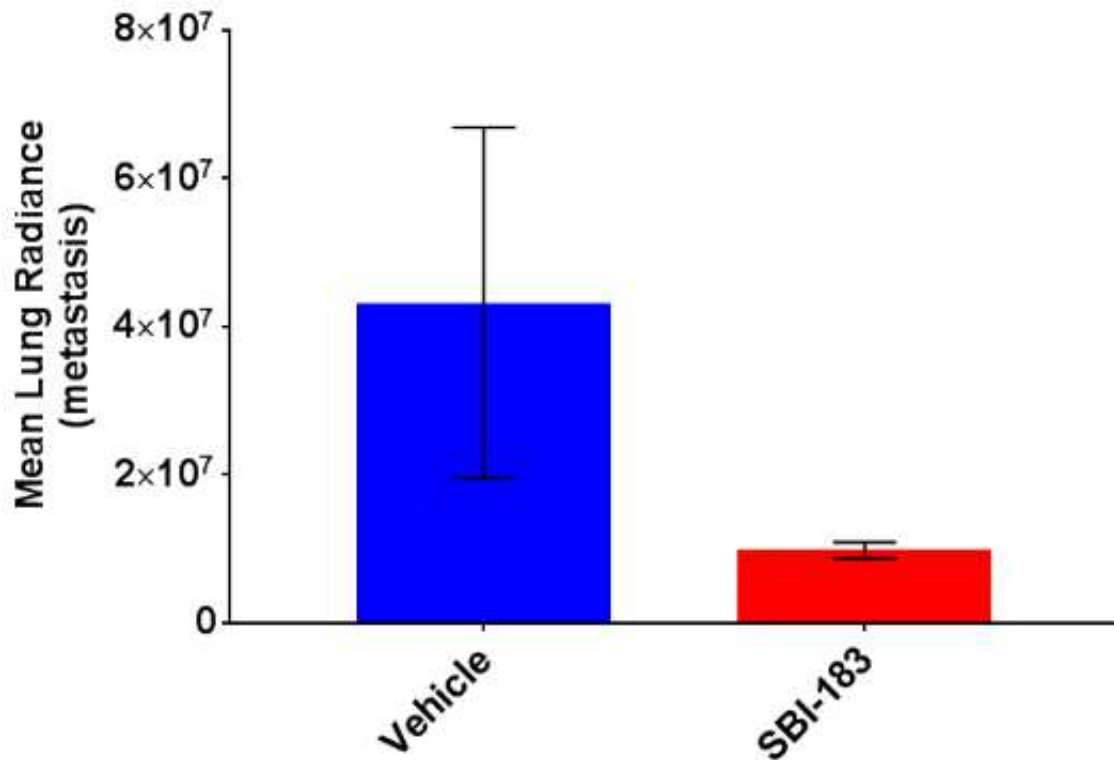


Figure 13. SBI-183 reduces lung metastasis *in vivo*. Daily treatment with SBI-183 (100 mg/kg) resulted in a 76% decrease in lung metastasis of triple negative MDA-MB-231 breast cancer cells as determined by bioluminescence imaging. Twelve mice per group were utilized for this experiment. In the Vehicle group, mouse 1 was a moribund sacrifice (day 25) and mouse 8 was found dead (day 28). Percentage of decrease was calculated with the following formula: $100 - ((\text{Average SBI-183}) / (\text{Average Vehicle})) \times 100$. Error bars represent SEM. Significance was determined using Welch's t-test. $P = .197$

CHAPTER 4
TARGETED MODIFICATIONS TO THE CHEMICAL STRUCTURE OF SBI-183
INCREASE INHIBITION OF BOTH QSOX1 ENZYMATIC ACTIVITY AND
INHIBITION OF TUMOR INVASION

Overview:

We previously identified the novel small molecule “SBI-183” as an inhibitor of QSOX1 enzymatic activity, leading to suppression of the cancer phenotype. Here we embarked on a two-pronged screening strategy to A) identify chemical analogs of SBI-183 with increased anti-tumorigenic effects, and B) to additionally utilize these analogs to elucidate the essential chemical moieties on the lead molecule important in QSOX1 mediated anti-tumorigenicity. Cell-free screening for inhibition of enzymatic activity identified seven potential analogs with inhibition equal to or slightly stronger than that observed in SBI-183. Of these, SPX-009 was identified as the top hit with 3.8 to 12-fold increased inhibitory potency (cell line dependent) in the 3D invasion assay. Western blot analysis was negative for an upregulation of three additional sulfhydryl oxidases in response to QSOX1 inhibition. Laminin $\alpha 4$ staining intensity on 3D invaded spheroids by immunofluorescence was reduced in shKnockdown cell lines as compared to shScramble control, but increased in SPX-009 treated cells, likely due to disorganization of the underlying f-actin cytoskeleton.

Results:

The pyrrolidine ring in SBI-183 chemotype series is vital for inhibition of QSOX1 enzymatic activity.

We previously reported that, at μM concentrations, SBI-183 inhibited QSOX1 enzymatic activity, tumor cell proliferation and invasion *in vitro*, and tumor growth and metastasis *in vivo* (27). We therefore hypothesized that chemical modifications to SBI-183 would allow insight into the structure-activity relationship between SBI-183 and QSOX1. We additionally hypothesized that a compound which more potently inhibited QSOX1 would also more effectively inhibit the tumor phenotype. Fifty-three chemical analogs of SBI-183 were purchased from ChemBridge and screened for inhibition of QSOX1 enzymatic activity in the HVA fluorescence assay (Figure 14A-D). An additional eighteen analogs were synthesized by our collaborators at Sapphire Biotech (San Diego, CA) (Figure 14E & F). Of the compounds from ChemBridge, seven analogs displayed inhibitory activity that was equivalent to or slightly better than that observed with SBI-183: SPX-009, SPX-010, SPX-011, SPX-025, SPX-026, SPX-029, and SPX-043 (Figure 14A & C). Of these seven, SPX-009 appeared to be the best candidate (indicated by the red star in Figure 14A), having the strongest inhibition of enzymatic activity and an H_2O_2 control profile similar to that of SBI-183. Four analogs which appeared to be inhibiting QSOX1 activity were observed to also inhibit HRP or scavenge H_2O_2 in the control: SPX-033, SPX-037, SPX-039, and SPX-042 (Figure 14B & D). The compounds synthesized by Sapphire Biotech were not tested in the cell-free assay further due to inhibition observed in the H_2O_2 control. However, to ensure we did not erroneously

discard a QSOX1 inhibitor that also happened to scavenge H₂O₂, these compounds were screened on cells.

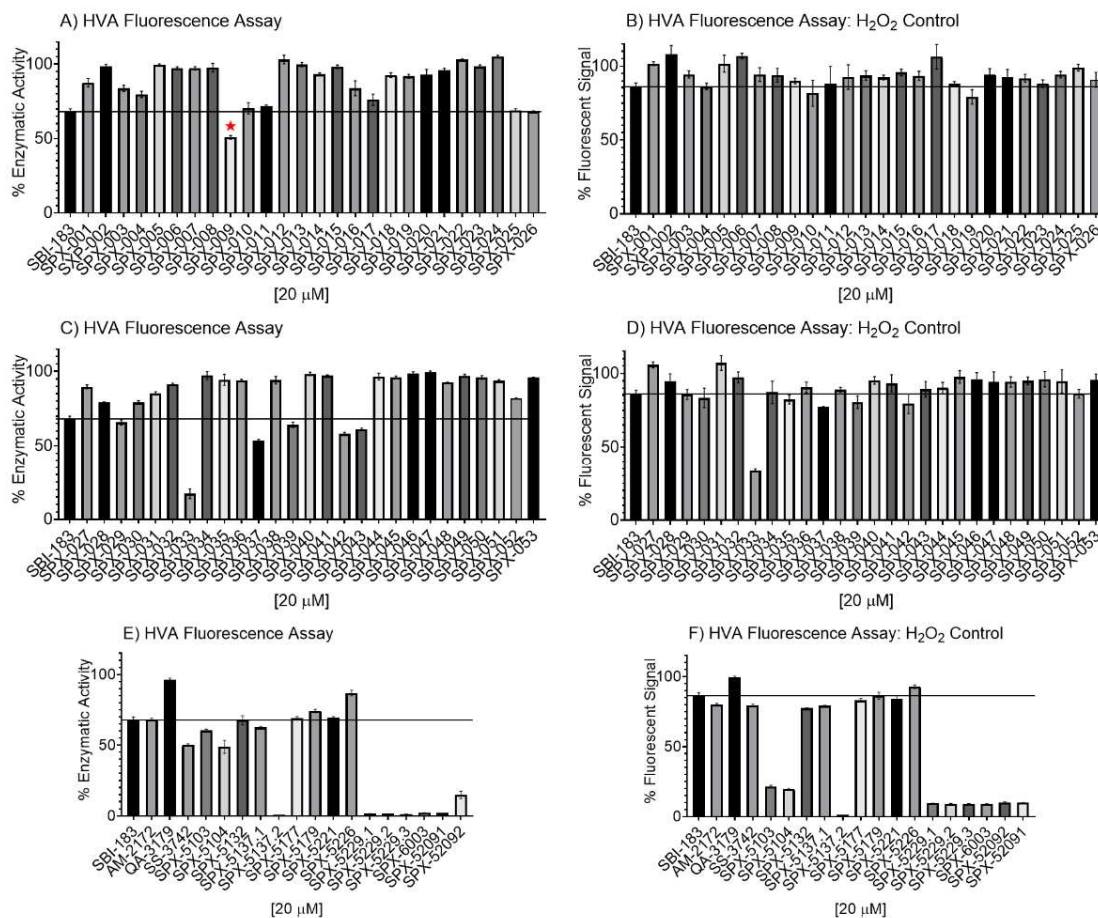


Figure 14. Screening chemical analogs of SBI-183 for inhibition of QSOX1 enzymatic activity with the HVA fluorescence assay. Compounds were screened at 20 μM for inhibition of QSOX1 enzymatic activity that was similar to or better than the inhibition observed with SBI-183 (A, C, & E). Data for SBI-183 is the average of 25 individual assays performed in triplicate. The red star (A) indicates the top hit, SPX-009. Figures B, D, & F are the no QSOX1, H₂O₂ control to verify that the observed decrease in fluorescent signal was due to QSOX1 inhibition and not inhibition of HRP or scavenging of H₂O₂. Experiments were performed in triplicate. Data were collected at time = 15 minutes (enzyme steady state). Percent signal was calculated as follows: ((Average Compound Signal/Average DMSO Vehicle Control Signal)*100). Error represents relative standard deviation and was calculated in Excel.

Top hits which did not exhibit scavenging of H₂O₂ or HRP inhibition were assayed at least two times to verify inhibition and to observe a dose response (Figure 15).

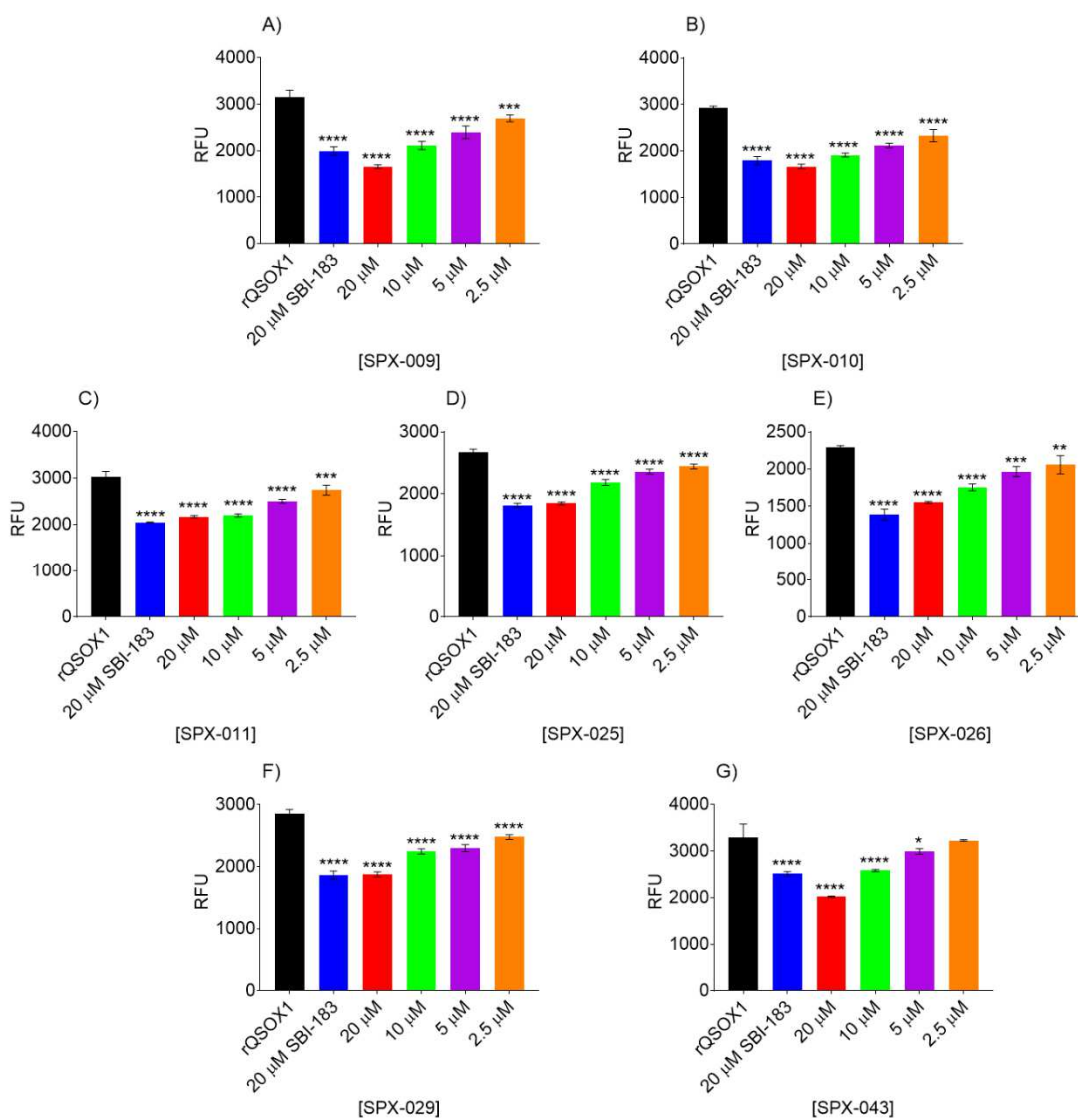


Figure 15. SBI-183 analogs demonstrate an inhibitory dose response in the HVA fluorescence assay. Top hits were assayed at least two times to confirm inhibition and dose response. Experiments were performed in triplicate. RFU = Relative Fluorescence Units. Data were collected at time = 15 minutes (enzyme steady state). Error represents standard deviation. Significance was determined by one-way ANOVA and * = $p < .05$, ** $p < .01$, *** $p < .001$, **** $p < .0001$.

Analysis of the structure of the ChemBridge compounds and the resultant inhibition of enzymatic activity revealed that any chemical additions to the pyrrolidine

ring of SBI-183 resulted in a loss of QSOX1 inhibition (Table 6). However, examination of SPX-5177, SPX-5179, and SPX-5221 reveal that removal of carbons or C-C bonding which are distal to the nitrogen of the pyrrolidine ring may not impair inhibitory activity (See Table 6). SBI-183 contains a “permissive benzene” (a benzene to which chemical changes can be made which may result in similar or increased inhibition of enzymatic activity), and a “variable benzene” (a benzene to which chemical changes can be made which may result in either the loss of enzymatic inhibition, or retention of enzymatic inhibition) (Table 6 & Figure 16). These results indicate that the pyrrolidine ring of SBI-183 is most important for inhibition of enzymatic activity and that targeted modifications to the permissive or variable benzenes can increase inhibitory activity. Further, these results implicate SPX-009 as a top candidate for further screening.

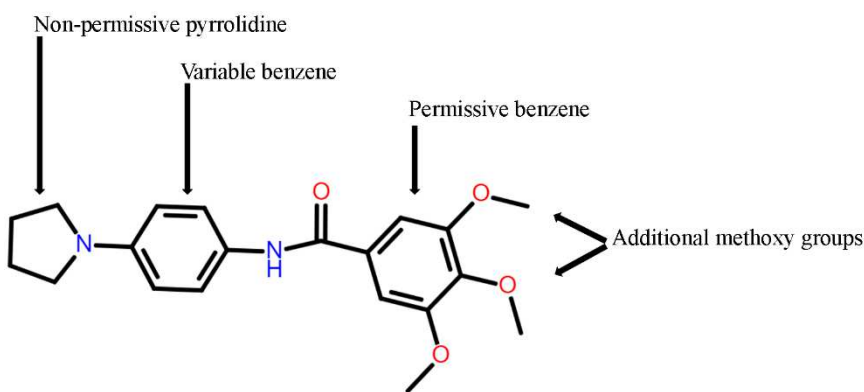


Figure 16. Chemical structure of SPX-009. Compared to SBI-183, SPX-009 contains the addition of 4, 5-methoxy on the permissive benzene. Labelling of “Non-permissive pyrrolidine”, “Variable benzene”, and “Permissive benzene” is based on the observed inhibition of QSOX1 enzymatic activity from the 53 chemical analogs of SBI-183 in the HVA assay.

SPX-009 inhibits 3D invasion.

Because invasion is an early step in the metastatic process, we next began a screening protocol of SPX-009 on tumor spheroids grown in 3D to mimic the *in vivo*

phenotype. MDA-MB-231, MIA PaCa2, and RCJ-41T2 were treated with concentrations of SPX-009 ranging from 10 μ M - 1.25 μ M. SBI-183 was incubated with the spheroids as a control at 10 μ M. Additionally, shKnockdown's were generated as described (27) in MDA-MB-231 and MIA PaCa2 as additional controls to further verify the QSOX1 invasive phenotype. Knockdown was verified by qRT-PCR (Figure 17F, G). SPX-009 inhibited 3D invasion of all three cell lines at each concentration tested to the same extent as SBI-183 at 10 μ M. Therefore, two-fold titrations of SPX-009 were performed beginning at 1.25 μ M to determine the limit of inhibition (Figure 17). Statistically significant inhibition was observed in MDA-MB-231 and MIA PaCa2 with dosages of SPX-009 down to 156.25 nM, while RCJ-41T2 was significantly inhibited down to 312.5 nM. As can be seen in Figure 17, panels D, E, & F, each of the three cell lines invaded into the surrounding Matrigel matrix in the .01% DMSO control by day 3. Conversely, invasion of cells treated with 1.25 μ M SPX-009 was statistically significantly inhibited on day 3, with only a few solitary cells invading into the surrounding matrix (Figure 17G, H, I). A similar reduction in invasion was observed in both shQSOX1-transduced MDA-MB-231 and shQSOX1-transduced MIA PaCa2 (Figure 17D-E2). Interestingly, while shKnockdown inhibition of invasion was statistically significant, it was not as robust as that observed with SPX-009 in these cell lines. In all cell lines, 1.25 μ M SPX-009 more potently inhibited 3D invasion than did the same concentration of SBI-183.

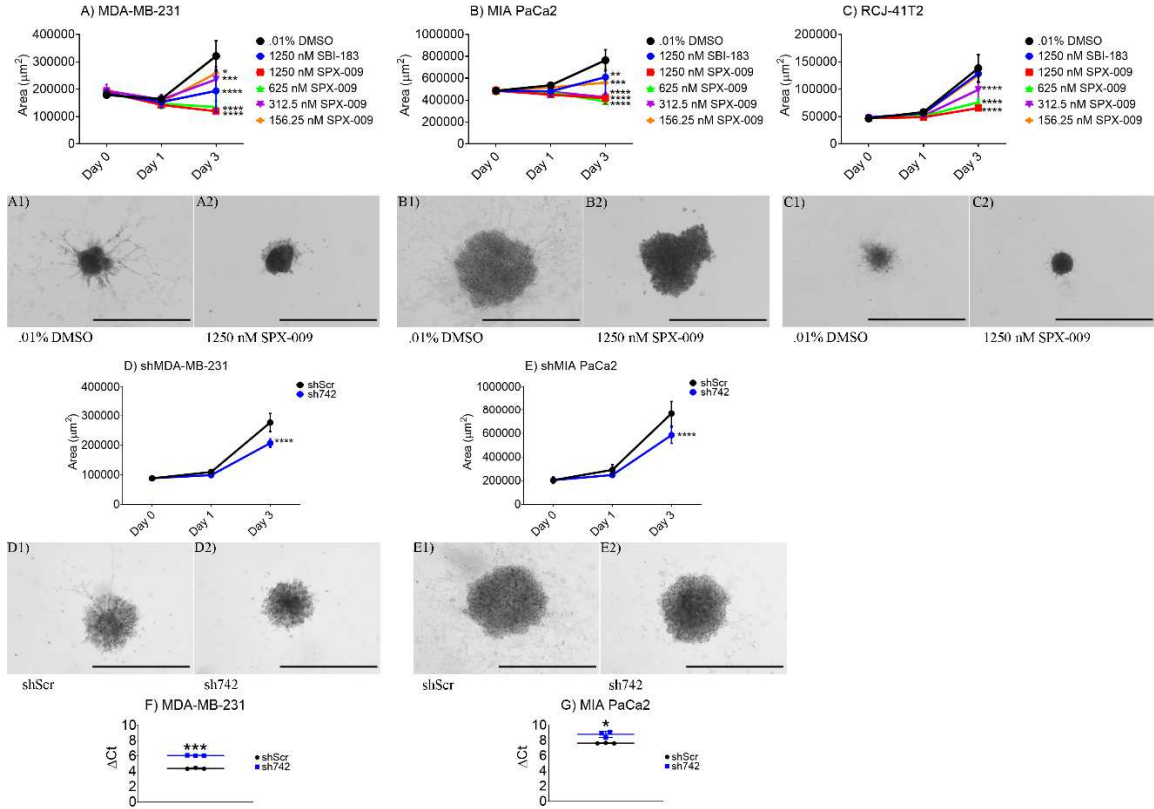


Figure 17. SPX-009 inhibits 3D invasion in a dose dependent manner. Two-fold dilutions of SPX-009 beginning at 1250 nM resulted in dose dependent inhibition of 3D invasion (A-C). Percentage of invasion decrease at 1250 nM was 63% in MDA-MB-231, 45% in MIA PaCa2, and 53% in RCJ-41T2. Representative images of the spheroids taken on day 3 of .01% DMSO control (A1, B1, C1) or treated with 1.25 μ M SPX-009 (A2, B2, C2). In MDA-MB-231 and MIA PaCa2, shKnockdown of QSOX1 results in a reduction in invasion as compared to the shScr control (D & E). Percentage of invasion decrease for sh742 as compared to shScr was 26% for MDA-MB-231, and 24% for MIA PaCa2. Representative images of shScr invaded spheroid (D1, E1) versus sh742 knockdown (D2, E2). Scale bar = 1000 μ m. SPX-009 experiments were performed in replicates of six. Short hairpin experiments were performed in replicates of twelve. Percentage of invasion decrease was calculated as follows: $(100 - (\text{Average Compound} / \text{Average Vehicle Control}) * 100)$. Error represents standard deviation. Significance was determined by two-way ANOVA and * = $p < .05$, ** $p < .01$, *** $p < .001$, **** $p < .0001$. Short hairpin knockdown was verified by qRT-PCR (F, G). Error represents standard deviation. Significance was determined by Welch's t-test. * $p < .05$, *** $p < .001$.

IC₅₀ for SPX-009 invasion was calculated as 395 nM for MDA-MB-231, 178.8 nM for MIA PaCa2, and 304.7 nM for RCJ-41T2 (Figure 18).

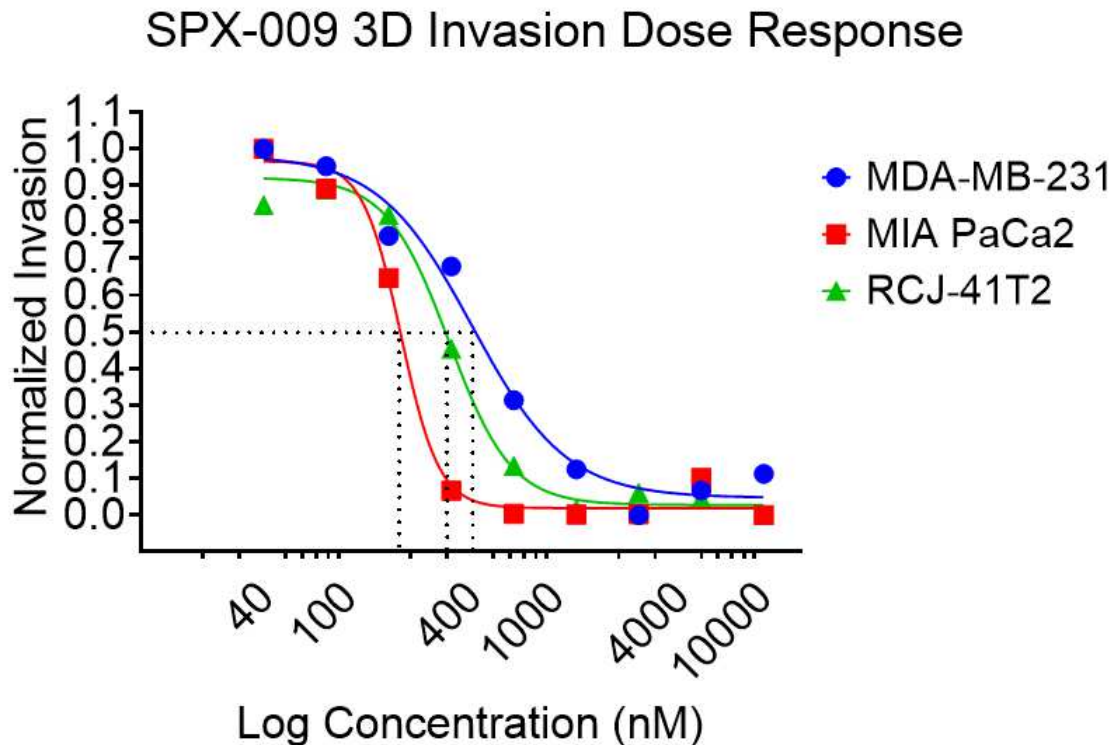


Figure 18. Determination of SPX-009 3D Invasion IC₅₀. Cells were plated in replicates of six and dosed with two-fold dilutions of SPX-009 from 10 μ M – 39.1 nM. Invasion area values from day 3 were normalized and GraphPad Prism was utilized to determine the IC₅₀'s of MDA-MB-231 (395 nM), MIA PaCa2 (178.8 nM), and RCJ-41T2 (304.7 nM).

Because SPX-009 robustly inhibited 3D invasion in all cell lines at 1.25 μ M, the remaining top hits from the HVA fluorescence assay were screened at the same concentration and compared to SPX-009 and SBI-183 (Figure 19). SPX-009 inhibited 3D invasion more vigorously than all other compounds. Additionally, it was the only compound (with the exception of SBI-183) with consistent anti-invasive properties across the three cell lines.

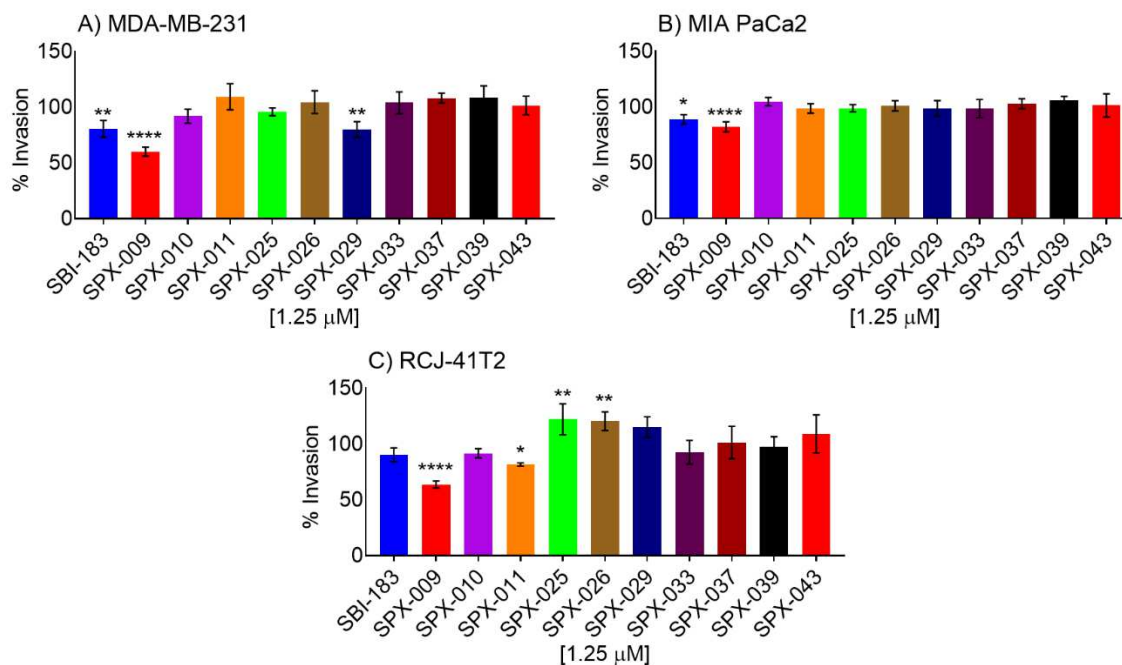


Figure 19. SPX-009 is the strongest inhibitor of 3D invasion. The top hits from the fluorescence assay were screened at a concentration of 1.25 μM in the 3D invasion assay. Assays were stopped once statistical significance was reached for SPX-009: Day 1 (A), and Day 3 (B & C). Experiments were performed in replicates of six. % Invasion = ((Average Compound/Average Vehicle Control)*100). Error represents relative standard deviation and was calculated in Excel. Significance was determined by one-way ANOVA and * = p<.05, **p<.01, ***p<.001, ****p<.0001.

SPX-009 inhibits 2D Boyden Chamber Invasion.

Because the 3D invasion assay in Figure 17 was performed over the course of three days, it was possible that the observed decrease in invasion was due to inhibition of cell proliferation instead of suppression of invasion. To address this possibility, we performed a 2D Boyden Chamber invasion assay to verify our results, in which invasion was stopped at 18-24 hours after plating. Since one cell division takes at least 24 hours, cell proliferation is not a concern in the 2D invasion assay. As can be seen in Figure 20, inhibition of invasion with SPX-009 was statistically significant in MDA-MB-231, MIA PaCa2, and RCJ-41T2.

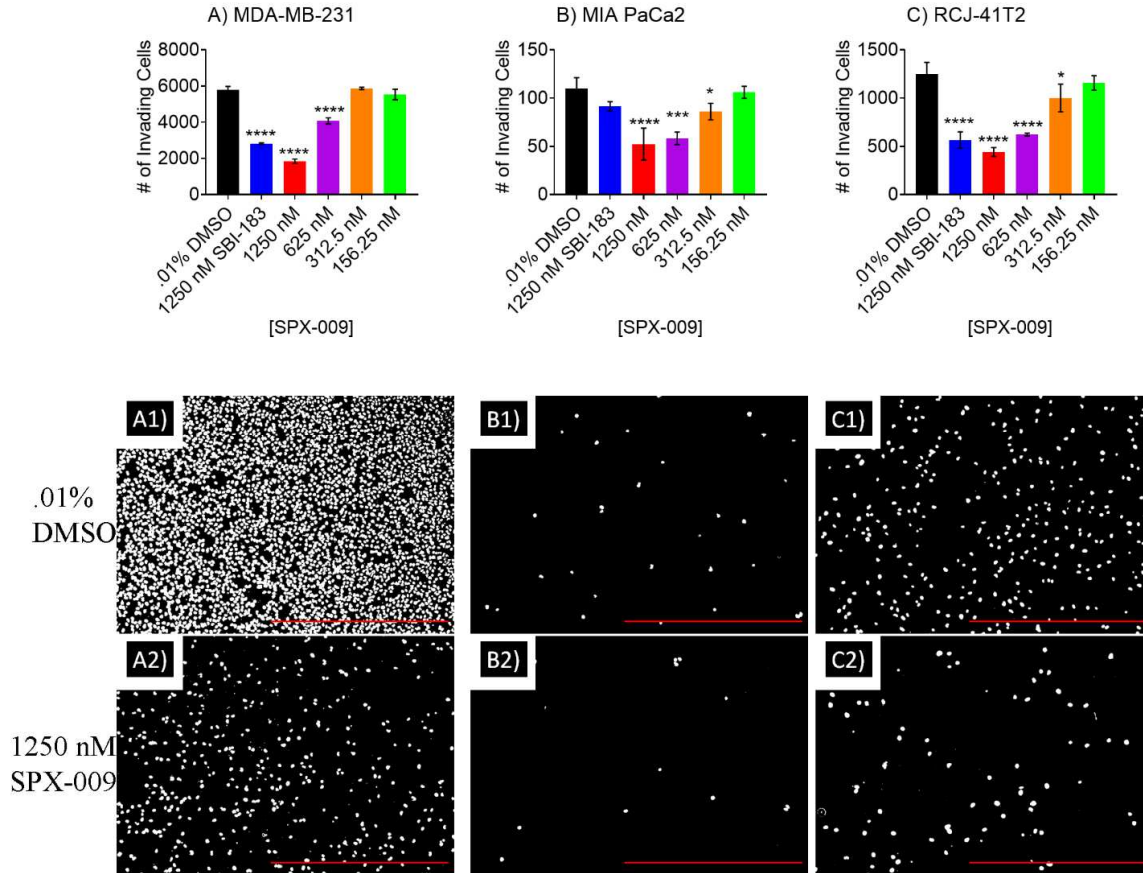


Figure 20. SPX-009 inhibits 2D Boyden Chamber invasion in a dose dependent manner. Two-fold dilutions of SPX-009 beginning at 1.25 μM resulted in dose dependent inhibition of 2D invasion (A-C). Percentage of invasion decrease at 1250 nM SPX-009 was 68% in MDA-MB-231, 52% in MIA PaCa2, and 65% in RCJ-41T2. Representative images of invaded, DAPI-stained nuclei of cells treated with .01% DMSO (A1, B1, C1) or 1250 nM SPX-009 (A2, B2, C2). Images were edited for clarity using ImageJ. Scale bar = 1000 μm. Experiments were performed in triplicate. Percentage of invasion decrease was calculated as follows: $(100 - (\text{Average Compound} / \text{Average Vehicle Control}) * 100)$. Error represents standard deviation. Significance was determined by one-way ANOVA and * = $p < .05$, **** $p < .0001$.

Addition of exogenous rQSOX1 partially rescues the invasive phenotype.

To provide further support for our hypothesis that cellular QSOX1 is the target of SPX-009, we performed 3D rescue invasions in which rQSOX1 was added to cells exogenously. Similar to SBI-183, addition of exogenous rQSOX1 partially rescued the invasive phenotype (27). We incubated SPX-009 with exogenous rQSOX1 on 3D

spheroids. Addition of a four-fold molar excess of rQSOX1 partially rescued the invasive phenotype of MDA-MB-231 (Figure 21A), while a two-fold molar excess of rQSOX1 partially rescued the invasive phenotype of MIA PaCa2 and RCJ-41T2 (Figure 21B & C). These data further support QSOX1 as a cellular target of SPX-009.

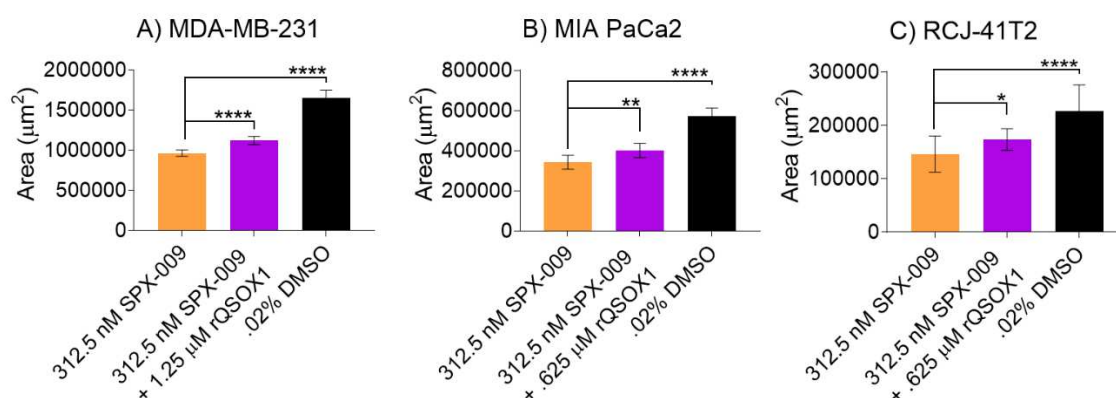


Figure 21. Addition of exogenous rQSOX1 partially rescues 3D invasion. Incubation of 312.5 nM SPX-009 with exogenous rQSOX1 resulted in a partial rescue of 3D invasion by day 3 in each cell line. Addition of a four-fold molar excess of rQSOX1:SPX-009 resulted in a 16% increase in 3D invasion as compared to SPX-009 alone (A). Addition of a two-fold molar excess of rQSOX1:SPX-009 to MIA PaCa2 and RCJ-41T2 resulted in 17% (B) and 19% (C) increase in invasion respectively when compared to SPX-009 alone. Experiments were performed in replicates of six. Error represents standard deviation. Significance was determined by two-way ANOVA and * = $p < .05$, ** $p < .01$, **** $p < .0001$.

Verification of lack of cellular activity with SPX-006 & SPX-007.

It was observed that SPX-006 and SPX-007 both contained the substitution of a piperidine ring for the pyrrolidine ring of SBI-183. SPX-006 additionally contained the substitution of a benzyloxy moiety in place of the methoxy group on the permissive benzene. In addition to the piperidine ring, SPX-007 contained a fluorine at the ortho position on the variable benzene (See Table 6). These modifications resulted in a loss of inhibition of QSOX1 enzymatic activity (Figure 14A). Therefore, it was hypothesized that SPX-006 and SPX-007 would not inhibit 3D invasion as strongly as SBI-183. At a

concentration of 10 μM , SPX-006 and SPX-007 both exhibited a statistically significant reduction in 3D invasion inhibition in each cell line tested when compared to SBI-183 (Figure 22). Interestingly, substitution of the bulky benzyloxy group on the permissive benzene of SPX-006 reduced inhibition of 3D invasion more than the addition of the fluorine on the variable benzene of SPX-007. Because the targeted modifications made to SPX-006 and SPX-007 resulted in a loss of activity in the HVA assay and a reduction in inhibition of the cancer phenotype, these results support the role of QSOX1 in cancer and further support QSOX1 as a cellular target of SPX-009.

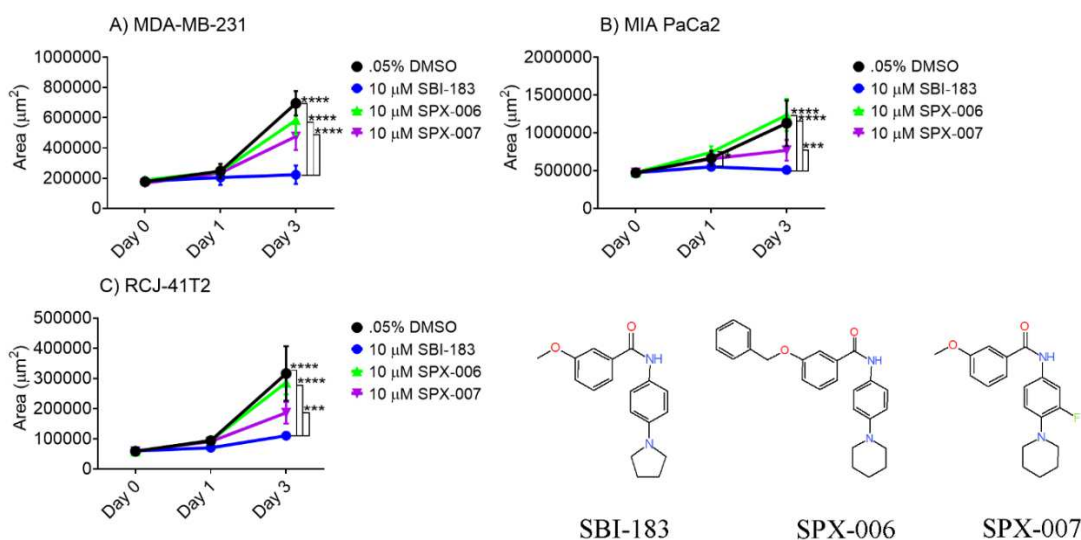


Figure 22. Alterations to the chemical structure of SBI-183 resulting in a loss of QSOX1 enzymatic activity also resulted in a loss of inhibition of 3D invasion. Spheroids were dosed with SPX-006 and SPX-007 at a concentration of 10 μM and compared to the same concentration of SBI-183 in MDA-MB-231 (A), MIA PaCa2 (B), and RCJ-41T2 (C). In each cell line, both compounds were less potent than SBI-183 by day 3. Incubation of tumor cell lines with SPX-006 increased invasion over incubation with SBI-183 by 261% in MDA-MB-231, by 163% in MIA PaCa2, and by 191% in RCJ-41T2. Incubation with SPX-007 increased invasion over incubation with SBI-183 by 213% in MDA-MB-231, by 129% in MIA PaCa2, and by 144% in RCJ-41T2. Experiments were performed in replicates of six. Percentage of invasion increase was calculated as follows: ((Average SPX Compound/Average SBI-183)*100). Error represents standard deviation. Significance was determined by two-way ANOVA and *** $p < .001$, **** $p < .0001$.

Targeted modifications to SBI-183 begin to reveal compound functionality.

Because SPX-009 was our best inhibitor of QSOX1 enzymatic activity in the HVA fluorescence assay and was active at inhibiting 3D invasion, our collaborators at Sapphire Biotech synthesized a number of additional SBI-183 analogs with targeted modifications (Table 6). As with the compounds purchased from ChemBridge, these compounds were screened in the HVA fluorescence assay (Figure 14E & F). All of the compounds except SPX-5226 appeared to have a similar activity profile to SBI-183, however most also scavenged H₂O₂ or inhibited HRP (Figure 14F). Therefore, to ensure we did not erroneously discard a QSOX1 inhibitory compound, these compounds were further screened in the 3D invasion assay. AM-2172 (addition of a fluorine adjacent to pyrrolidine ring on the variable benzene, used in F19 NMR studies) displayed an anti-invasive profile similar to SPX-009 (Figure 23A, C, E), further supporting our previous conclusions that targeted modification can be made to this benzene and activity retained. SPX-5179 (removal of C-C bond between carbons 3-4 of pyrrolidine ring) had activity similar to SBI-183 (Figure 23A, C, E). This was the first SBI-183 analog screened containing a change to the pyrrolidine ring which did not eradicate activity. Interestingly, in the compounds purchased from Chembridge, modifications to the pyrrolidine ring constituted additional chemical groups, making the ring larger and bulkier. These results with SPX-5179 indicate that with direct SBI-183 analogs, modification of the pyrrolidine ring which result in a smaller or more flexible structure, are possible and still retain activity. In contrast, SPX-5177 has the same modification to carbons 3-4 on the pyrrolidine ring but otherwise has the same structure as SPX-009, and it was not active in the 3D invasion assay (Figure 23A, C, E). Similarly, SPX-5221, also a direct SPX-009

analog, no longer contains carbons 3-4 of the pyrrolidine ring, and has no activity in the 3D invasion assay (Figure 23A, C, E). These results indicate that targeted modifications to the ring which make it smaller or more flexible are possible with direct SBI-183 analogs, but are not possible with SPX-009 analogs.

SBI-183 and SPX-009 contain an amide bond. Because amide bonds are easily cleaved *in vivo* (184), Sapphire Biotech synthesized sulfonamides, eliminating this amide bond. SPX-5229.1, 5229.2, 5229.3, 6003, 52091, and 52092 (Table 6) were synthesized and screened for anti-QSOX1 activity (Figure 14E & F) and in the 3D invasion assay (Figure 23B, D, F). Because SBI-183 was most active on cells at 20 μ M, this concentration was used in the initial screenings of the sulfonamides, however, each of the sulfonamides scavenge H₂O₂ or inhibit HRP (Figure 14F). As can be seen in Figure 23, panels B, D, & F, SPX-52091 was the only sulfonamide tested that was consistently active on cells, but it was not as active as SBI-183.

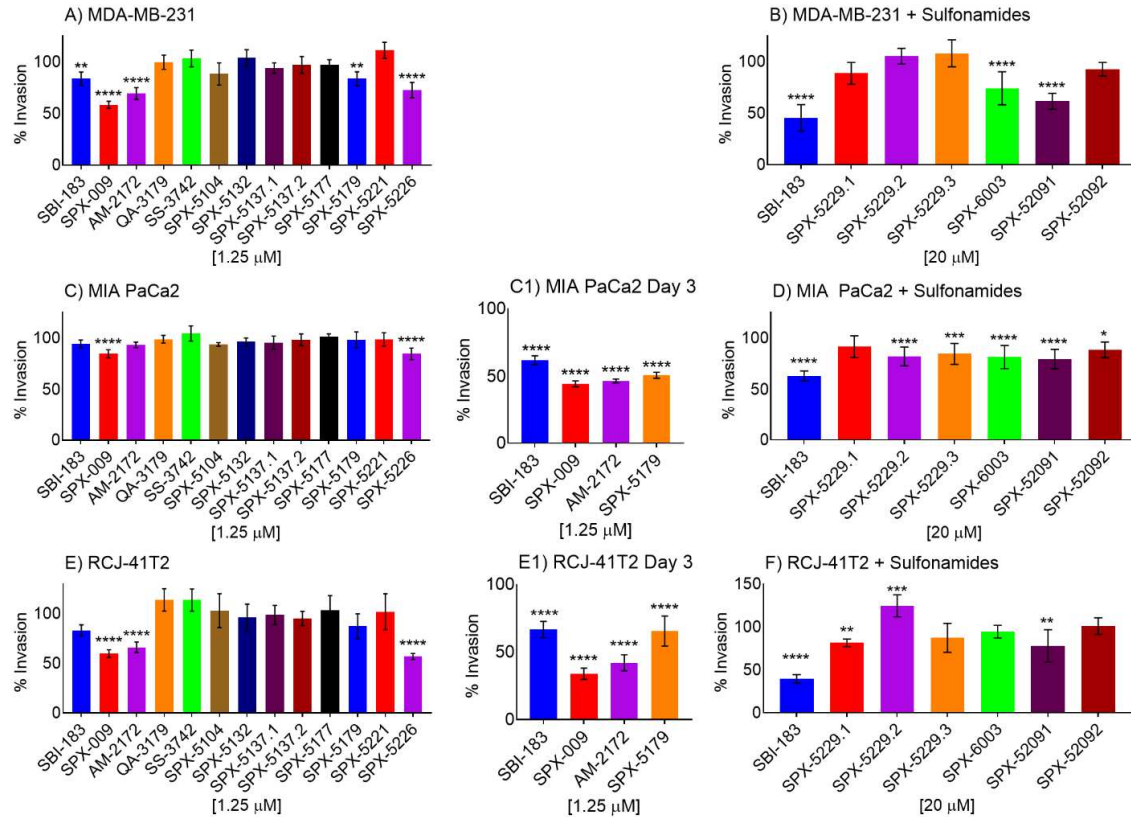


Figure 23. Targeted modifications to SBI-183 inhibit 3D invasion. The compounds were synthesized by Sapphire Biotech and screened in the 3D invasion assay at 1.25 μM. By day 1, MDA-MB-231 and RCJ-41T2 were inhibited by AM-2172 and SPX-5226 (A & E). MDA-MB-231 was additionally inhibited by SPX-5179 (A). MIA PaCa2 was inhibited by SPX-5226 by day 1 (C). By day 3, MIA PaCa2 was also inhibited by AM-2172 and SPX-5179 (C1), while RCJ-41T2 was additionally inhibited by SPX-5179 (E1). SBI-183 sulfonamide analogs were screened at 20 μM and data are from day 1 (B, D, F). Aside from SBI-183, SPX-52091 was the only sulfonamide analog to consistently inhibit 3D invasion. Experiments were plated in replicates of six. % Invasion = ((Average Compound/Average Vehicle Control)*100). Error represents relative standard deviation and was calculated in Excel. Significance was determined by two-way ANOVA and *p<.05, **p<.01, ***p<.001, ****p<.0001.

SPX-009 modulates spheroid formation.

Cells grown in 3D form tumoroids and exhibit a more natural ECM than those grown in 2D (6,28,32). Further, QSOX1 modulates the structure of cancer ECM (27,144–148). We therefore hypothesized that SPX-009, which inhibits QSOX1, would inhibit the

ability of tumor cell lines to form spheroids. Cells were plated as for a 3D invasion assay, but in the presence of .01% DMSO (vehicle control), 1.25 μ M SBI-183, or 1.25 μ M SPX-009. In contrast to the 3D invasion assay, no Matrigel was added to the cells. Instead, on day three, the tumoroids were imaged in media alone and area was quantified. It was expected that all cell lines would form looser spheroids. Surprisingly, we observed that the cell lines which initially formed loose, grape-like clustered spheroids, MDA-MB-231 and MIA PaCa2, both formed smaller spheroids in the presence of SBI-183 and SPX-009 (Figure 24A-A3, B-B3). The cell lines which initially formed dense spheroids, RCJ-41T2, A549, and Panc1, formed the looser spheroids, as expected in the presence of SPX-009, but were not affected by the presence of SBI-183 (Figure 24C-C3, E-E3).

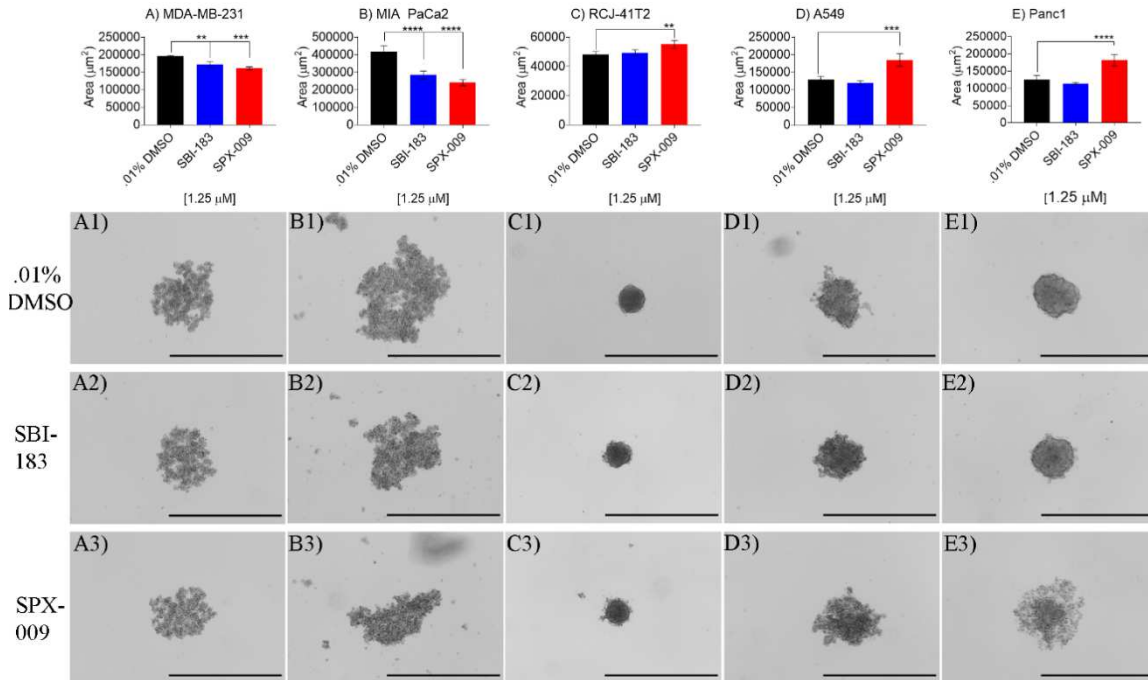


Figure 24. SPX-009 modulates spheroid formation. Cells were plated in replicates of four in the presence of 1.25 μ M SBI-183 or SPX-009 and allowed to form spheroids for 3 days. Data are from day 3. MDA-MB-231 and MIA PaCa2, cell lines which initially form loose, grape-like spheroids formed smaller, denser spheroids in the presence of SBI-183 and SPX-009 (A-A3, B-B3). RCJ-41T2, A549, and Panc1, cell lines which initially form dense spheroids, formed looser spheroids in the presence of SPX-009. Scale bar = 1000 μ m. Error represents standard deviation. Significance was determined by one-way ANOVA and ** = $p < .01$, *** $p < .001$, **** $p < .0001$.

SPX-009 inhibits proliferation by MTT by day 5, but not by day 3.

We next wanted to determine if the smaller spheroids formed by MDA-MB-231 and MIA PaCa2, were due to inhibition of proliferation. Additionally, while we knew from the 2D Boyden Chamber invasion assay that SPX-009 does inhibit invasion, we wanted further clarification on the time course of inhibition. Therefore, we performed MTT assays on days 1, 3, and 5 to measure proliferation. These results revealed that while inhibition with SPX-009 was statistically significant by day 3 in MIA PaCa2 at the highest dosage (Figure 25B & B1) it did not inhibit proliferation by day 3 in MDA-MB-

231 or RCJ-41T2 (Figure 25A, A1, C, C1). By day 5, statistically significant inhibition of proliferation was observed in all 3 cell lines. Inhibition of proliferation of normal fibroblasts (Figure 25F) was statistically significant at 625 nM, but not at 1250 nM on day 3, but by day 5 both concentrations were statistically significant. Interestingly, shKnockdown of QSOX1 in MDA-MB-231 and MIA PaCa2 did not display any inhibition of proliferation at any time point (Figure 25D & E).

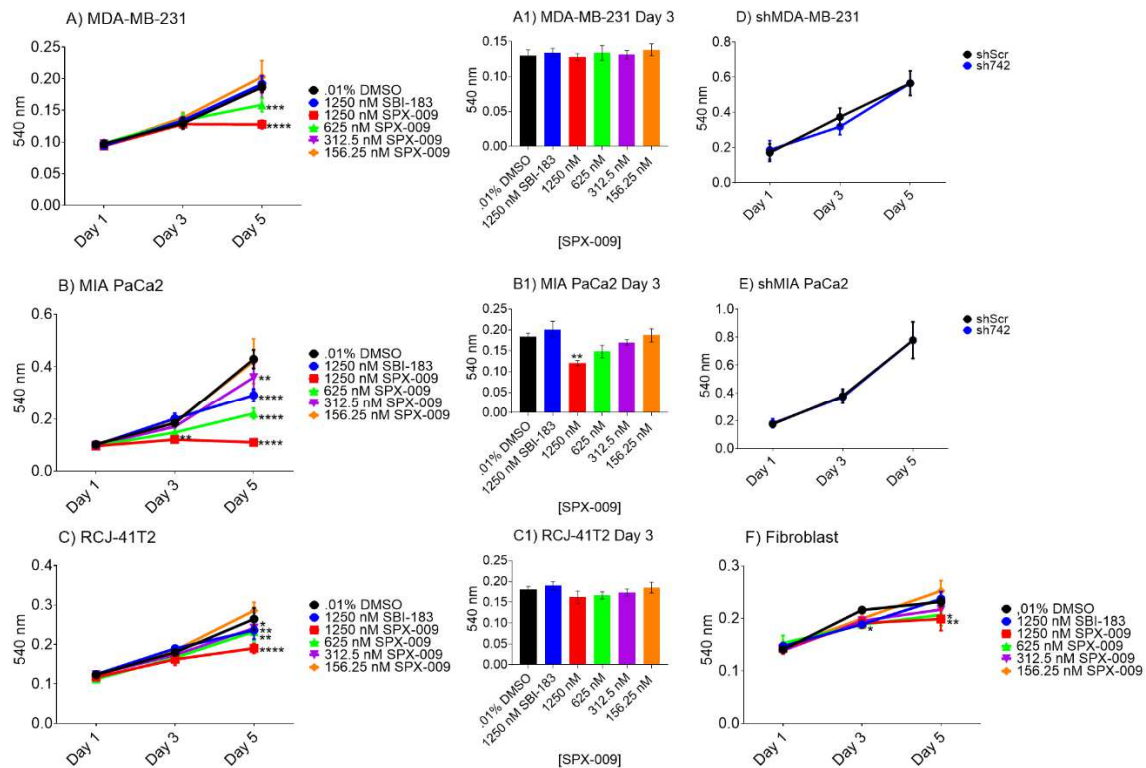


Figure 25. SPX-009 inhibits proliferation by day five, but not by day three by MTT. Cell lines were incubated with the indicated concentration of SBI-183 or SPX-009 in replicates of six for 1, 3, and 5 days. By day 3, some statistically significant inhibition was observed in MIA PaCa2 at the highest dosage of SPX-009 (B and B1), and in normal Fibroblasts at 625 nM SPX-009 (F) but no statistically significant inhibition was observed at other dosages or in other cell lines (A, A1, C, C1). By day 5, statistically significant inhibition of proliferation was observed in all cell lines (A, B, C, F). Percentage of proliferation decrease on day 5 at 1250 nM SPX-009 was 32% in MDA-MB-231, 74% in MIA PaCa2, 28% in RCJ-41T2, and 14% in normal Fibroblasts. Percentage of proliferation decrease was calculated as follows: $(100 - (\text{Average}))$

Compound/Average Vehicle Control)*100). Short hairpin knockdown of QSOX1 in MDA-MB-231 and MIA PaCa2 (D & E) did not result in inhibition of proliferation at any time point tested. Error represents standard deviation. Significance was determined by two-way ANOVA and * = $p < .05$, ** = $p < .01$, *** $p < .001$, **** $p < .0001$.

IC₅₀ was determined by dosing the cells with two-fold dilutions of SPX-009 from 10 μM to .039 μM (Figure 26) and was calculated as 1.3 μM for MDA-MB-231, .87 μM for MIA PaCa2, and 1.0 μM for RCJ-41T2. While some of the inhibition of 3D invasion that is observed with SPX-009 in MIA PaCa2 could be at least partially due to inhibition of proliferation at 1250 nM SPX-009, the full dose-response observed in Figure 17 is indeed due to inhibition of invasion. Additionally, while the smaller spheroids formed by MIA PaCa2 in the presence of SPX-009 are likely due to inhibition of proliferation, the smaller spheroids formed by MDA-MB-231 in the presence of SPX-009 were not due to inhibition of proliferation (Figure 24). Finally, for all cell lines, these results indicate that the observed inhibition of 3D invasion is not due to suppression of proliferation.

SPX-009 Viability Dose Response

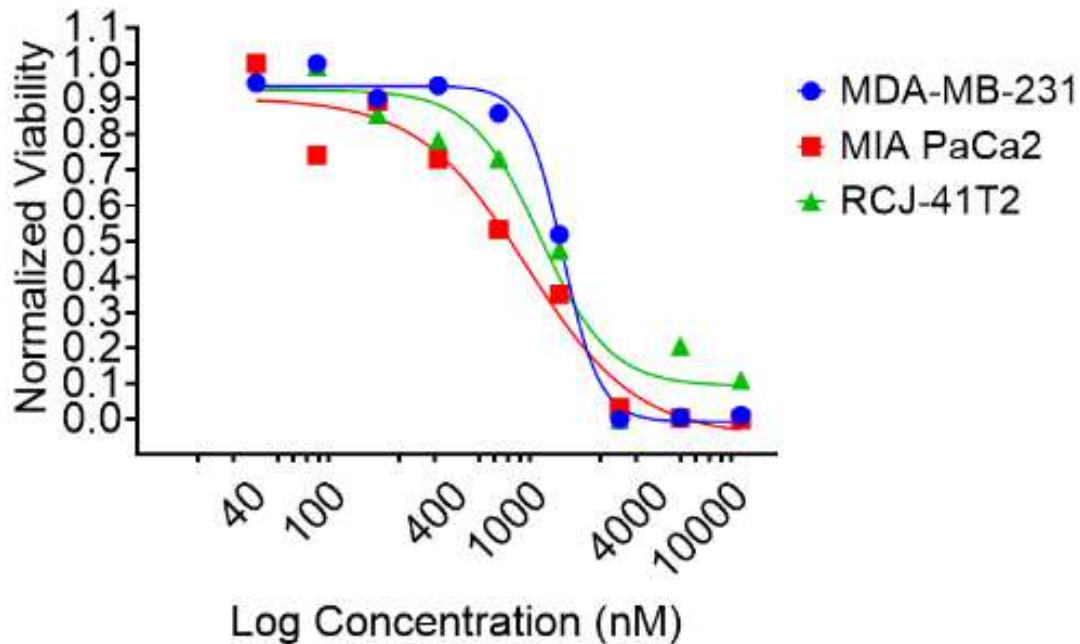


Figure 26. Determination of SPX-009 viability IC_{50} . Cells were plated in replicates of six. MTT values from day 3 were normalized and GraphPad Prism was utilized to determine the IC_{50} 's of MDA-MB-231 (1.3 μ M), MIA PaCa2 (.87 μ M), and RCJ-41T2 (1.0 μ M).

QSOX1 levels increase over time.

We next questioned why we did not observe inhibition of proliferation by day 3 in the MTT assay. We hypothesized that tumor cells continuously secrete QSOX1, therefore, QSOX1 levels in tumor supernatant would increase over time. Cells were plated at 4×10^4 cells/well in a six-well plate. Western blot analysis with the α NEQ antibody (long form) on tumor supernatants collected on days three and nine revealed that QSOX1-L levels do indeed increase the longer the supernatant is on the cells (Figure 27A, B, C). While very faint expression of QSOX1-L can be detected by western blot on day 3, much more robust expression is detected on day nine in all three cell lines.

Because the cells were 100% confluent by day nine, we next questioned if QSOX1-L expression was due to cell number or cell-cell contact. Cells were plated in a T225 flask at 10×10^6 cells/flask (large amount of cells, cell-cell contact) and at 1×10^6 cells/flask (large amount of cells, no cell-cell contact) and supernatant from day 3 was again collected. Probing these supernatants with the α NEQ antibody revealed clear and robust expression of QSOX1-L in all three cell lines under both conditions (Figure 27D), indicating cell-cell contact is not required for QSOX1-L expression in tumor cells. To determine if QSOX1-L is involved in cell adhesion, 10×10^6 cells were plated in a T225 and then a capture ELISA specific for both QSOX1-S and QSOX1-L was performed on supernatant collected after 2 (cells loosely adhered), 4 (cells more firmly adhered), 8 (cells adhered), and 24 hours. As can be seen in Figure 27, graph E, total QSOX1 levels in the supernatant are steady within the first two time points (collections each separated by 2 hours), then levels increase at the eight hour (on cells for 4 hours) and 24 hour time points (on cells for 16 hours). Because very low levels of QSOX1 which are undetectable by ELISA may play an important role in cell adhesion, and therefore in the tumor microenvironment, these results cannot rule out a role for QSOX1 in cell adhesion. However, these results do agree with our western blot data indicating that QSOX1 accumulates in supernatant over time. Finally, we questioned if the increased levels of QSOX1 protein in the supernatant correlated with increased mRNA expression. Total QSOX1 mRNA levels, normalized to β -actin, revealed steady mRNA expression for all cell lines on days 1-7 when compared to day 1 (Figure 27F). Compared to day 1, on day 9 a statistically significant increase in QSOX1 mRNA expression was observed in MIA PaCa2, but not in MDA-MB-231 or RCJ-41T2. Taken together, these results reveal that

QSOX1 protein in supernatant accumulates over time. In our MTT, low levels of QSOX1 on the day 1 and day 3 time points could explain why no statistically significant inhibition of proliferation was observed.

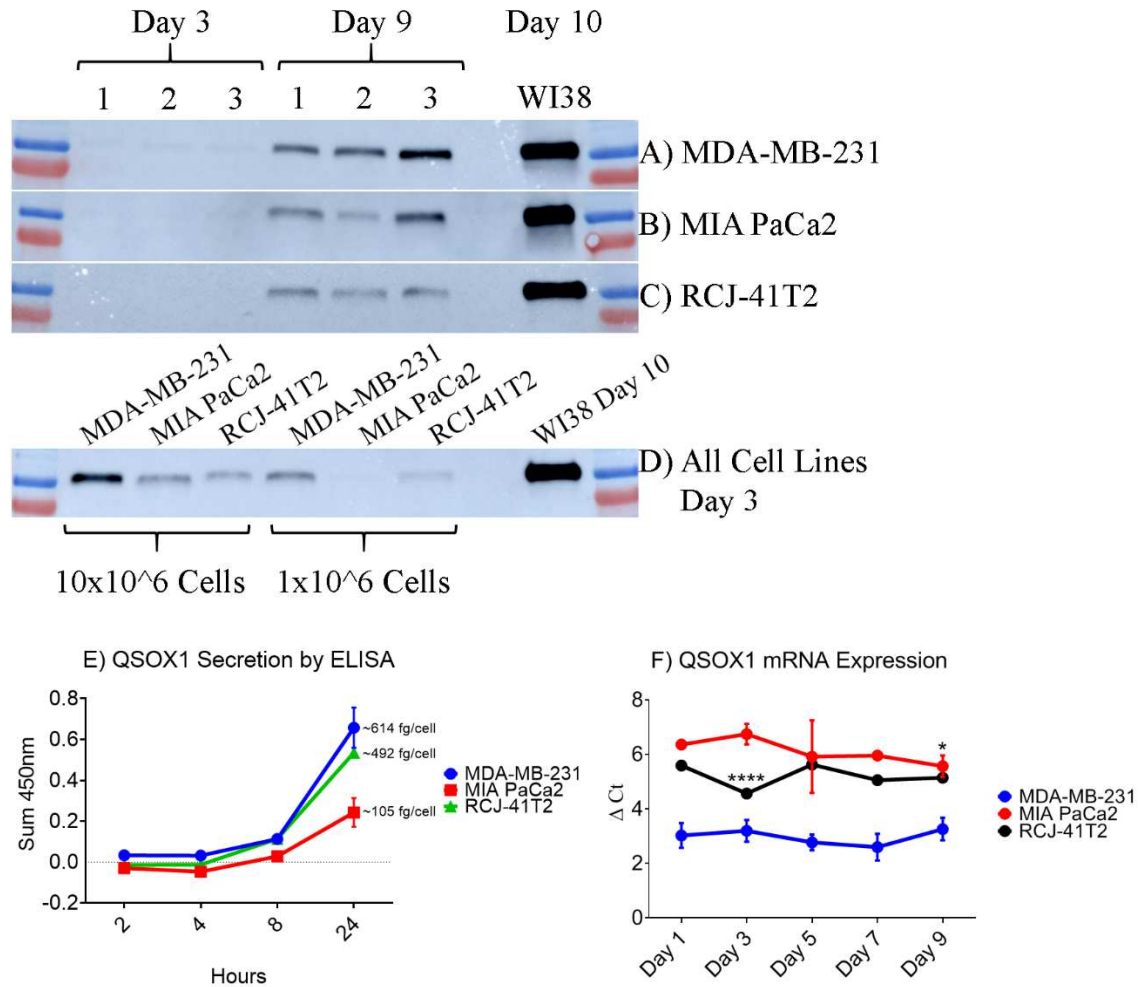


Figure 27. QSOX1 levels in supernatant increase over time. Cells were plated in triplicate at 4×10^4 cells/well in a six well plate. Media from days 3 and 9 were TCA-precipitated and protein concentration was estimated using the BCA method. 20 μ g total protein was loaded/lane. Probing with the α NEQ antibody revealed very faint expression of QSOX1-L on day 3, and much more robust expression was observed by day 9 (A, B, C) for each cell line. WI38 supernatant collected after ten days on cells was included as a positive control. Collection of day 3 supernatant from cells plated at 10×10^6 cells in a T225 flask revealed that the amount of QSOX1-L in supernatant is directly related to the number of cells (D). Collection of day 3 supernatant from cells plated at 1×10^6 cells in a T225 flask revealed that cancer cell expression of QSOX1-L is not contingent upon cell-cell contact. A capture ELISA specific for both QSOX1-S and QSOX1-L indicated that

QSOX1 accumulates in supernatant over time (E). QSOX1 mRNA levels normalized against β -actin were steady for MDA-MB-231 and MIA PaCa2 on days 1-7 (F). RCJ-41T2 QSOX1 mRNA levels were steady except for an increase on day 3, which leveled back out by day 5. A statistically significant increase of mRNA expression was observed in MIA PaCa2 on day 9 as compared to day 1, but no similar increases were observed in MDA-MB-231 or RCJ-41T2.

Inhibition of QSOX1 does not increase expression of PDI, ERO1 α , or ALR.

QSOX1^{-/-} mice were found to overexpress ERO1 α in their heart tissue. Because sulfhydryl oxidase activity is required for proper protein folding and function, we hypothesized that when QSOX1 activity is inhibited, other sulfhydryl oxidases would be upregulated in compensation. While there are many sulfhydryl oxidases, we chose three which share some similarity to QSOX1: PDI (contains two CxxC motifs), ERO1 α (contains FAD moiety, reoxidizes PDI), and ALR (contains a CxxC motif and a FAD moiety). Levels of PDI (Figure 28A) under all conditions appeared similar, with no clear increase in band intensity. Levels of ERO1 α (Figure 28B) appeared slightly variable under the different conditions with a decrease in band intensity in short hairpin transduced MIA PaCa2 compared to control (Figure 28B-D3 & 4), which was not mimicked in the MIA PaCa2 compound-treated conditions (Figure 28B-G5, 6, & 7). Similar inconsistency was observed in ALR (Figure 28C) in which 2.5 μ M SBI-183 treated MDA-MB-231 (Figure 28C-F6) appeared to have slightly stronger band intensity than the .01% DMSO control, but the short hairpin transduced MDA-MB-231 did not display this difference (Figure 28C-D1 & 2). Finally, levels of all three sulfhydryl oxidases appeared the same between HAP-1 parental (Figure 28E1) and HAP-1 KO (Figure 28E2). While it is possible that a sulfhydryl oxidase is upregulated in response to

inhibition of QSOX1, these results indicate that PDI, ERO1 α , and ALR are not upregulated in compensation of inhibition of QSOX1 activity in tumor cells.

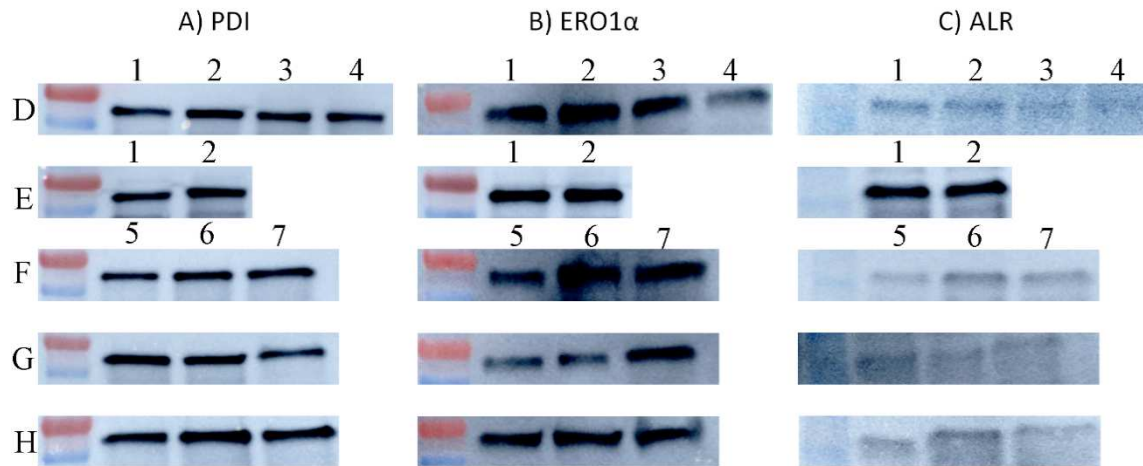


Figure 28. Inhibiting QSOX1 does not increase expression of three sulfhydryl oxidases in compensation. Total protein of cell lysate was estimated using BCA and 10 μ g total protein was loaded into gel. After transfer to PVDF membrane, blots were probed with antibody against PDI (A), ERO1 α (B), or ALR (C). Lanes are as follows: MDA-MB-231 shScr is D1, MDA-MB-231 sh742 is D2, MIA PaCa2 shScr is D3, MIA PaCa2 sh742 is D4. E1 is HAP-1 parental, E2 is HAP-1 KO. Columns 5, 6, and 7 are .01% DMSO vehicle control, 2.5 μ M SBI-183, and 1.25 μ M SPX-009 respectively. Rows F, G, and H are MDA-MB-231, MIA PaCa2, and RCJ-41T2 respectively. No consistent changes in band intensity were observed under any condition.

Inhibition of QSOX1 causes disruption to the ECM via laminin α 4 deposition.

QSOX1 is involved in fibronectin organization and incorporation of laminin α 4 into the ECM of fibroblasts and cancer cells grown in 2D or in mouse models (27,145,147,148).

We hypothesized that tumor cells grown in the 3D model would show similar ECM impairment when treated with the small molecule SPX-009. To study the ECM in this model, we chose to probe for the following proteins: laminin α 4, fibronectin, nidogen, and versican. Laminin α 4 and fibronectin were chosen for the reasons listed above.

Nidogen was chosen because of its well-known interaction with laminin α 4 (185,186).

Versican, which is involved in tumor progression, invasion, and EMT (187,188) was also chosen due to QSOX1's involvement in the same (27,139,148).

Cells were grown as described for a 3D invasion assay and allowed to invade for seven days. Short hairpin knockdown of QSOX1 in MDA-MB-231 and MIA PaCa2 resulted in a decrease in laminin α 4 fluorescence intensity, as did a complete KO of QSOX1 in HAP-1, when compared to the shScramble (MDA-MB-231, MIA PaCa2) or Parental (HAP-1) controls (Figure 29A, B, E, F, I, J, K, white arrows). This decrease in laminin α 4 intensity agrees with previous work (27,145). A surprising observation was made, however, on the cells treated with 312 nM SPX-009 when compared to their vehicle (DMSO) controls; an increase in laminin α 4 chain intensity was observed (Figure 29C, D, G, H, K, white arrows).

Laminin $\alpha 4$

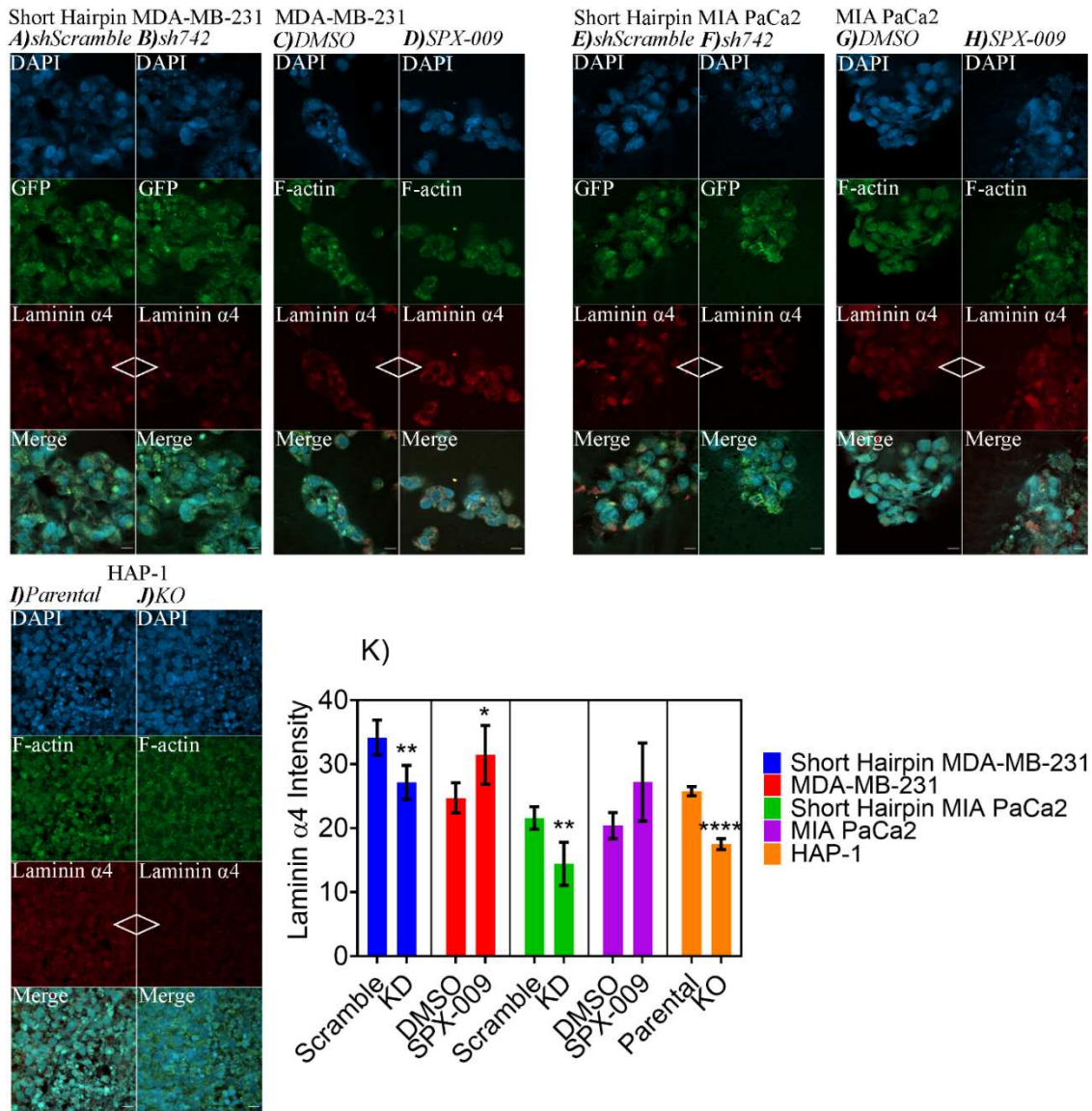


Figure 29. Genetic Knockdown or KO of QSOX1, or inhibition of QSOX1 with SPX-009, modulates ECM formation via deposition of laminin $\alpha 4$ in 3D invaded cells. Cells grown in 3D and invaded into Matrigel were formalin-fixed, paraffin embedded, and mounted on slides. Subsequent immunostaining for laminin $\alpha 4$ revealed that shKnockdown of QSOX1 in MDA-MB-231 and MIA PaCa2 resulted in a decrease in laminin $\alpha 4$ staining intensity compared to shScramble controls (A, B, E, F, K). The shlentiviral constructs contained a GFP marker. QSOX1 KO in HAP-1 also resulted in a reduction in laminin $\alpha 4$ staining intensity (I, J, K). Treatment of MDA-MB-231 and MIA PaCa2 with 312 nM SPX-009 resulted in an increase in laminin $\alpha 4$ staining intensity (C, D, G, H, K). All cell lines which were not treated with shRNA were counterstained with phalloidin Alexa Fluor-488 to visualize F-actin organization. Images were obtained on a Zeiss LSM 800 confocal microscope on the 63X oil objective. Treated cells versus their

controls were imaged at the same fluorescent intensity. Scale bar = 10 μm . Graphical representation of intensity is from five unique images. Error equals standard deviation.

Examination of the deposition pattern of laminin $\alpha 4$ in the SPX-009 treated cells revealed disorganization of laminin $\alpha 4$ ECM assembly (Figure 30). Specifically, vehicle treated cells (Figure 30A, B) displayed a smooth deposition pattern. MDA-MB-231 with vehicle showed some concentration of laminin $\alpha 4$ along the edges of some cells, but this concentration appeared regular. MIA PaCa2 vehicle treated cells displayed continuous laminin $\alpha 4$ staining. Observation of the SPX-009 treated cells, in contrast, showed discontinuous concentration of laminin $\alpha 4$ deposition across the cells (Figure 30C, D, white arrows) in a whirl pattern in some areas, and strong concentration in others.

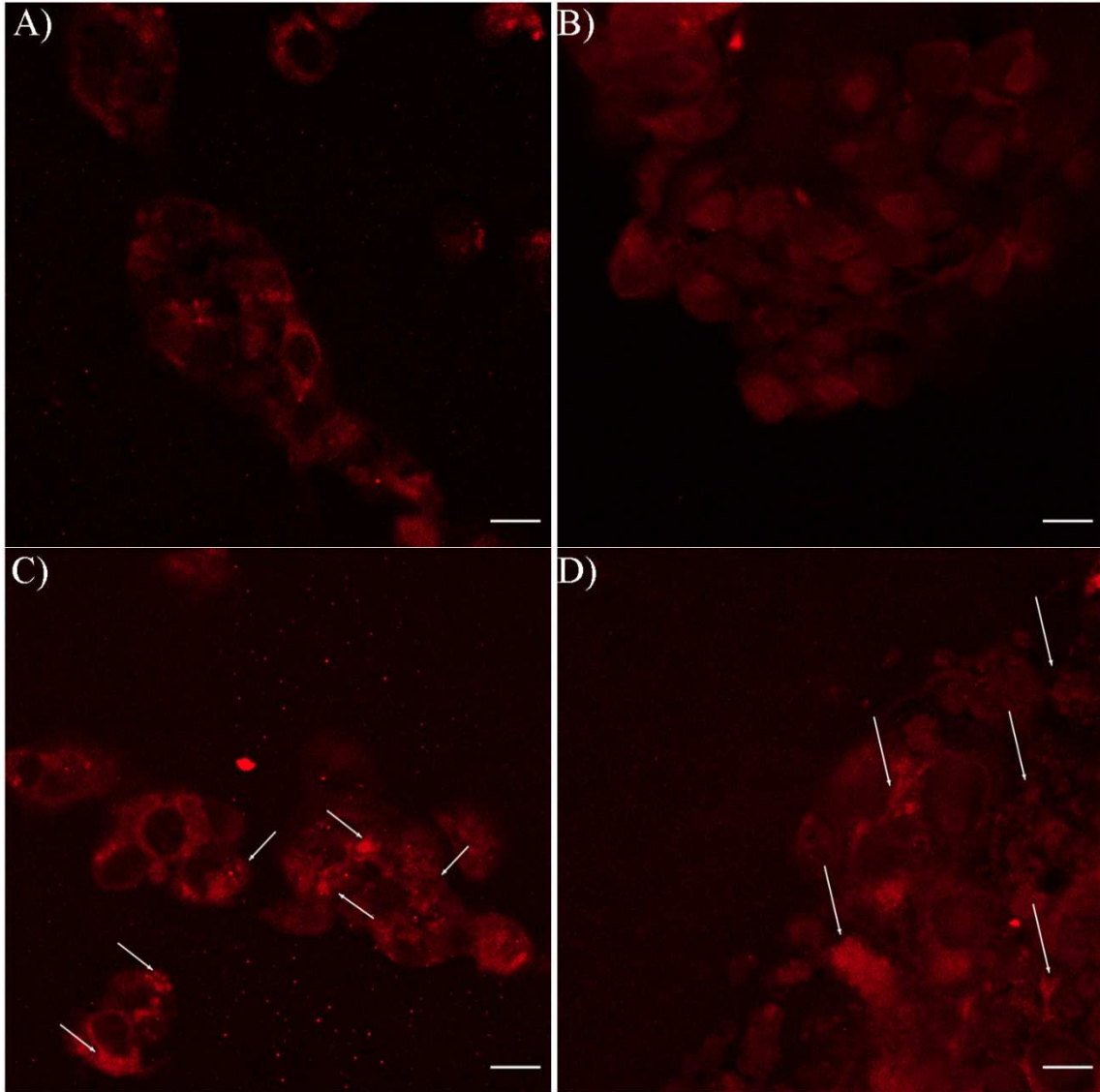


Figure 30. 3D invaded cells treated with SPX-009 display disorganization of Laminin $\alpha 4$. Images are from Figure 29, enlarged to show detail of laminin $\alpha 4$ deposition in MDA-MB-231 vehicle (A) versus 312 nM SPX-009 treated cells (C), and MIA PaCa2 vehicle (B) versus 312 nM SPX-009 treated cells (D). White arrows indicate areas of differential laminin $\alpha 4$ staining (concentration, whirl patterning). Scale bar = 10 μm .

Observation of the F-actin cytoskeleton revealed a similar patterning in the SPX-009 treated cells which was especially pronounced in MIA PaCa2 (Figure 31C, D, white arrows marked with “w”).

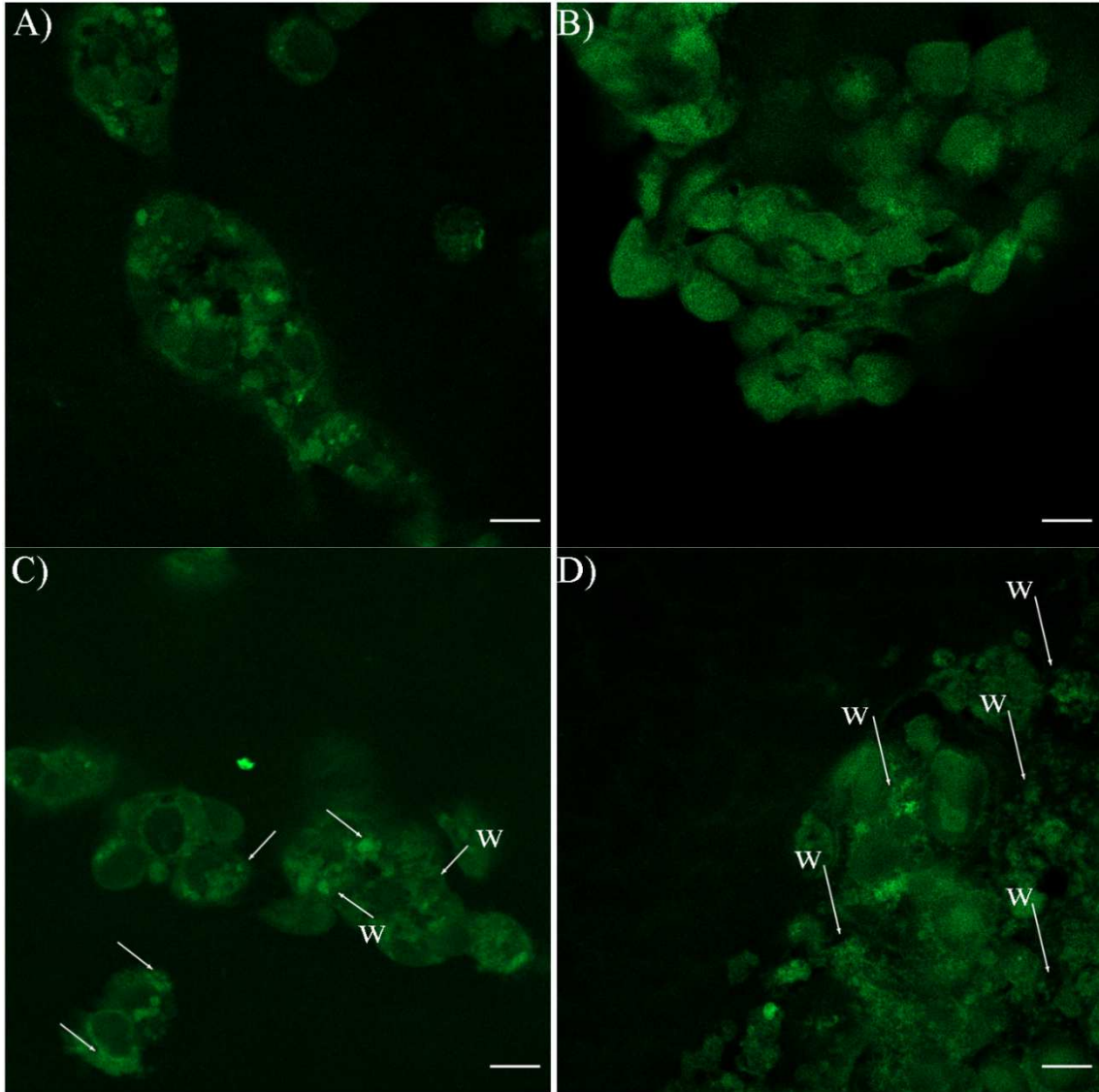


Figure 31. Treatment with SPX-009 causes disorganization of F-actin in 3D invaded cells. Images are from Figure 29, enlarged to show detail of F-actin organization in MDA-MB-231 vehicle (A) versus 312 nM SPX-009 treated cells (C), and MIA PaCa2 vehicle (B) versus 312 nM SPX-009 treated cells (D). White arrows indicate areas of differential laminin α 4 staining from Figure 30, while the addition of a “w” indicates differential whirling pattern. Scale bar = 10 μ m.

Observation of intensity and organization of the three remaining ECM proteins fibronectin, nidogen, and versican, did not yield any consistent differences in the treated versus the controls. Fibronectin intensity was statistically significantly higher in MIA

PaCa2 SPX-009 treated cells compared to vehicle control, and in HAP-1 KO versus Parental control, but no differences were observed in the other cell lines (Figure 32).

Fibronectin

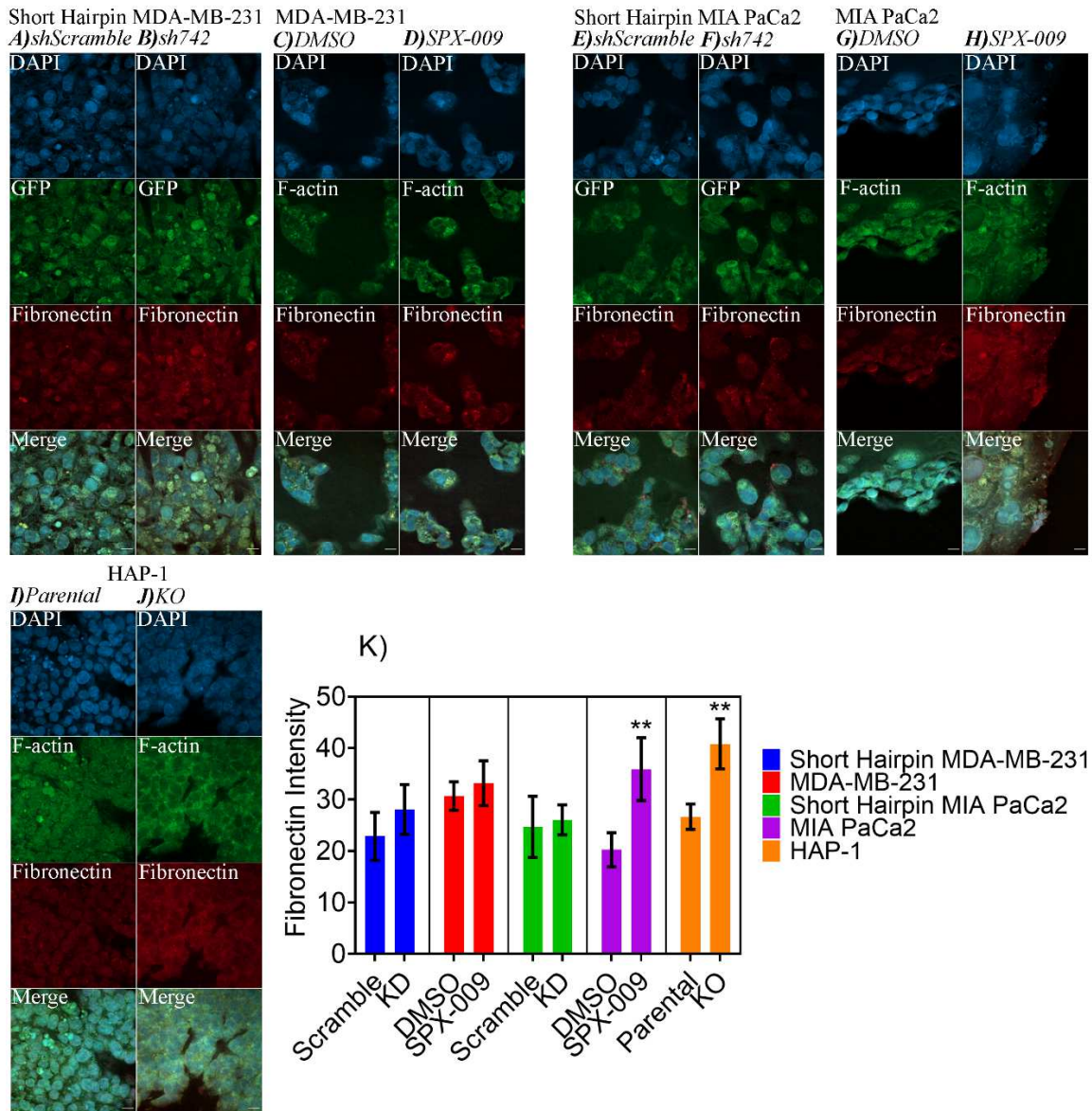


Figure 32. Immunostaining of fibronectin on 3D invaded cells does not yield any consistent changes in intensity or organization between conditions/cell lines. Cells grown in 3D and invaded into Matrigel were formalin-fixed, paraffin embedded, and mounted on slides. Subsequent immunostaining for fibronectin revealed no changes in shKnockdown of QSOX1 in MDA-MB-231 and MIA PaCa2 compared to shScramble controls (A, B, E, F, K). The shlentiviral constructs contained a GFP marker. QSOX1 KO in HAP-1 resulted in an increase in fibronectin intensity (I, J, K). Treatment of MDA-MB-231 with 312 nM SPX-009 resulted in no changes in fibronectin intensity (C, D, K), but the same treatment in MIA PaCa2 resulted in an increase in intensity (G, H, K). All cell lines which were not treated with shRNA were counterstained with phalloidin Alexa Fluor-488 to visualize F-actin organization. Images were obtained on a Zeiss LSM 800

confocal microscope on the 63X oil objective. Treated cells versus their controls were imaged at the same fluorescent intensity. Scale bar = 10 μ m. Graphical representation of intensity is from five unique images. Error equals standard deviation.

Immunostaining for nidogen yielded consistently higher intensity signal in the shKnockdown cells and the SPX-009 treated cells versus controls in MIA PaCa2 (Figure 33). The other cell lines did not display a similar increase.

Nidogen

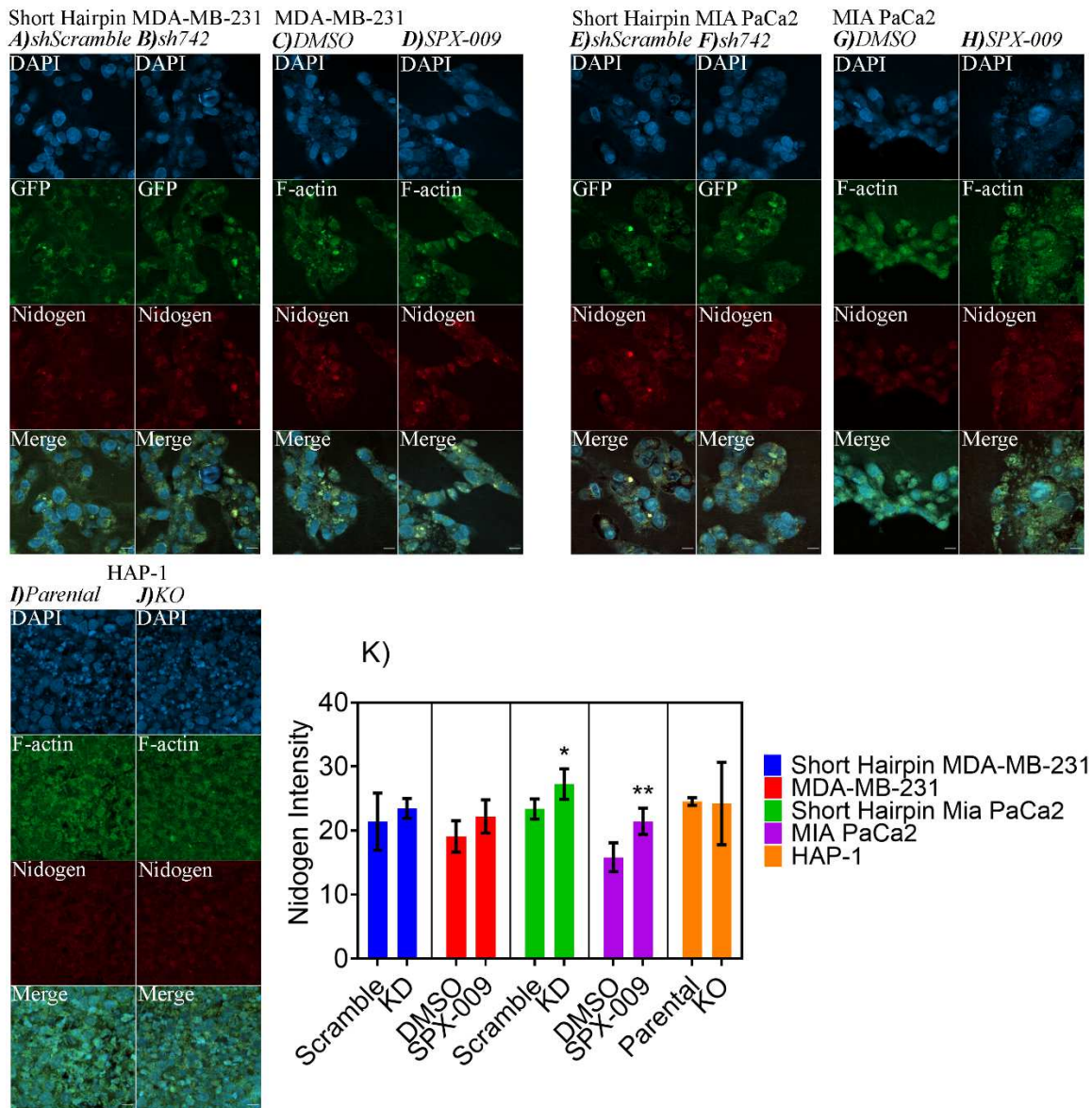


Figure 33. Immunostaining of nidogen on 3D invaded cells causes an increase in nidogen intensity in MIA PaCa2, but no changes in other cell lines. Cells grown in 3D and invaded into Matrigel were formalin-fixed, paraffin embedded, and mounted on slides. Subsequent immunostaining for nidogen revealed no changes in MDA-MB-231 (A, B, C, D, K) or in HAP-1 (I, J, K). MIA PaCa2 revealed a consistent increase in nidogen intensity in both the sh742 QSOX1 knockdown cells and 312 nM SPX-009 treated cells versus controls (E, F, G, H, K). The shlentiviral constructs contained a GFP marker. All cell lines which were not treated with shRNA were counterstained with phalloidin Alexa Fluor-488 to visualize F-actin organization. Images were obtained on a Zeiss LSM 800 confocal microscope on the 63X oil objective. Treated cells versus their controls were

imaged at the same fluorescent intensity. Scale bar = 10 μm . Graphical representation of intensity is from five unique images. Error equals standard deviation.

Immunostaining for versican yielded a statistically significant increase in intensity in MDA-MB-231 sh742 cells compared to the shScramble controls, but no other cell lines mimicked this change (Figure 34).

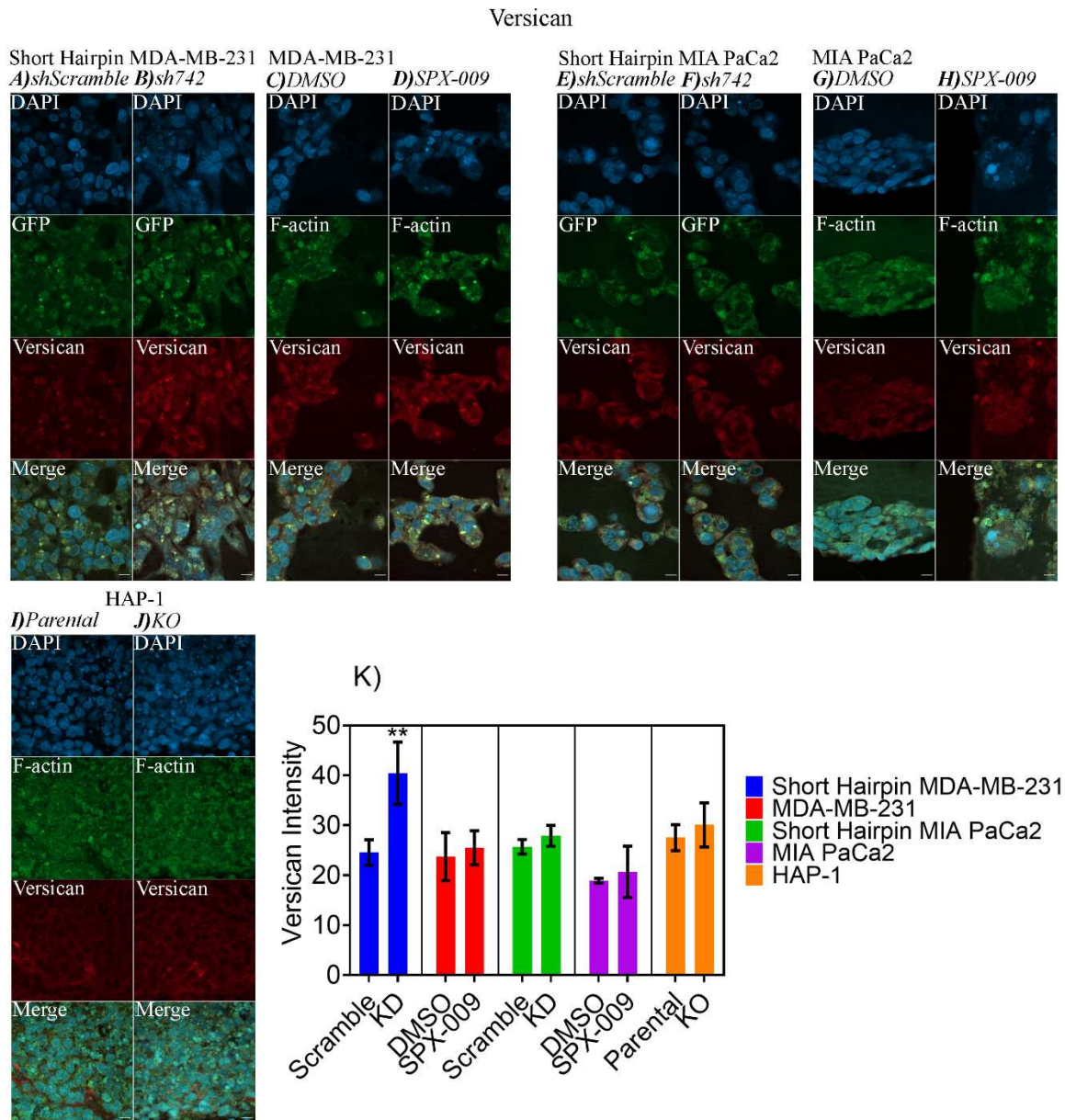


Figure 34. Immunostaining of versican on 3D invaded cells resulted in no consistent changes between condition/cell lines. Cells grown in 3D and invaded into Matrigel were formalin-fixed, paraffin embedded, and mounted on slides. Subsequent immunostaining for versican revealed no changes in any treated cells versus controls except in shKnockdown MDA-MB-231. Here an increase in versican intensity was observed in the knockdown versus the shScramble control (A, B, K). This change was not mimicked in the 312 nM SPX-009 treated cells versus vehicle control (C, D, K). The shlentiviral constructs contained a GFP marker. All cell lines which were not treated with shRNA were counterstained with phalloidin Alexa Fluor-488 to visualize F-actin organization. Images were obtained on a Zeiss LSM 800 confocal microscope on the 63X oil objective. Treated cells versus their controls were imaged at the same fluorescent intensity. Scale

bar = 10 μm . Graphical representation of intensity is from five unique images. Error equals standard deviation.

Alexa-fluor 647 α Mouse (laminin α 4, fibronectin, nidogen) and α Goat (versican) secondary only can be viewed in Figure 35 (all MDA-MB-231 & MIA PaCa2) and Figure 36 (all HAP-1).

2° Only Control

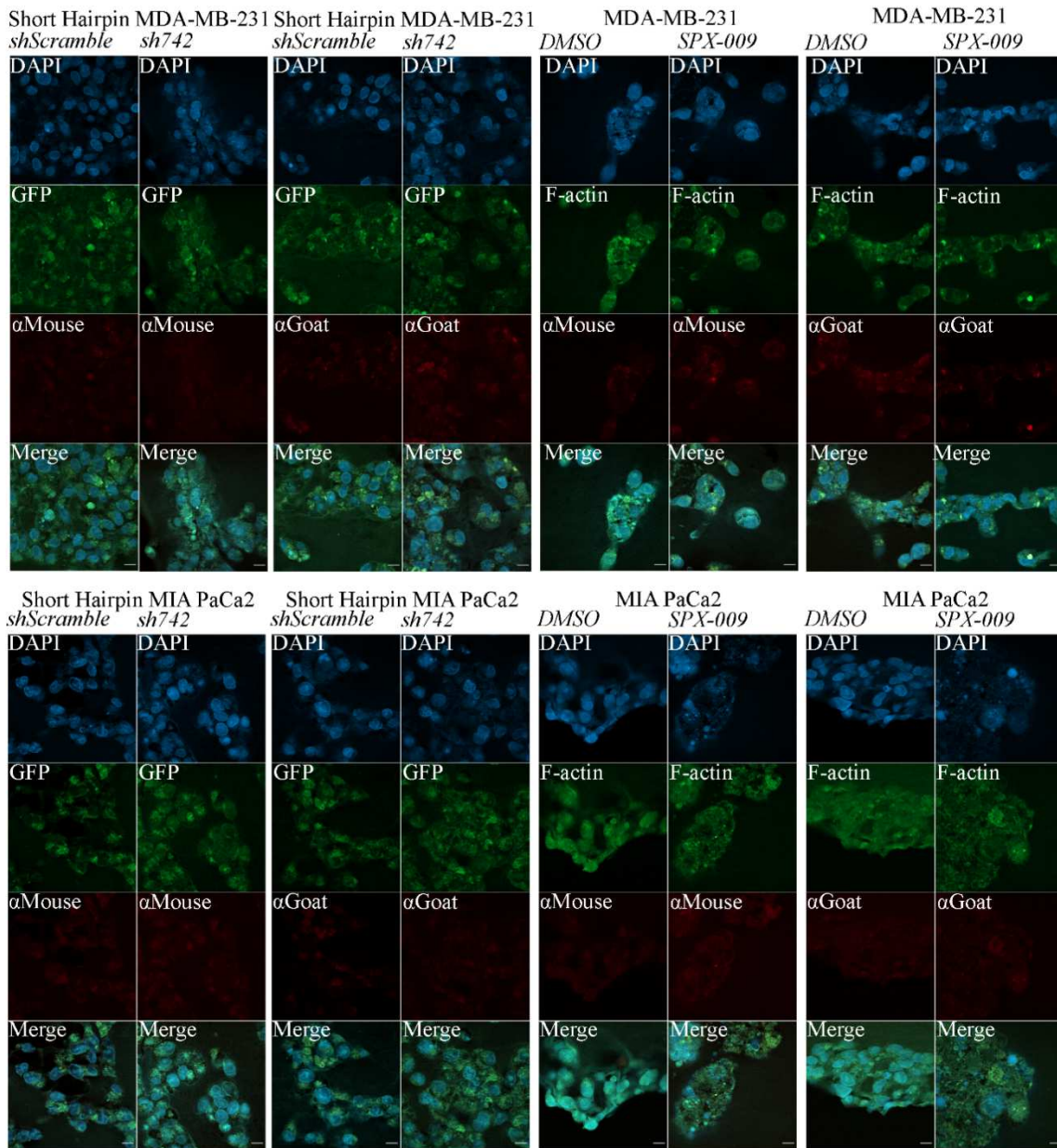


Figure 35. Immunofluorescence images of 3D invaded Short Hairpin, DMSO vehicle, or SPX-009 treated MDA-MB-231 and MIA PaCa2 not treated with primary antibody (secondary antibody only control). Images were taken at the highest exposure used in obtaining the images for laminin α 4, fibronectin, nidogen (α Mouse), or versican (α Goat). The shlentiviral constructs contained a GFP marker. All cell lines which were not treated with shRNA were counterstained with phalloidin Alexa Fluor-488 to visualize F-actin organization. Images were obtained on a Zeiss LSM 800 confocal microscope on the 63X

oil objective. Treated cells versus their controls were imaged at the same fluorescent intensity. Scale bar = 10 μ m.

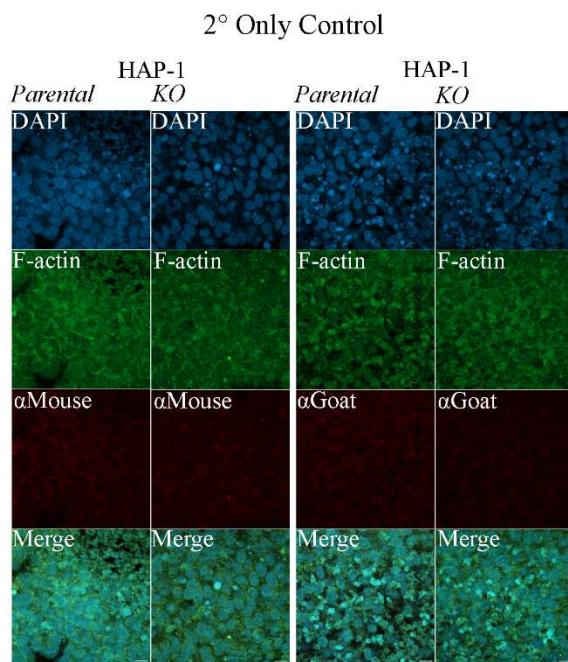


Figure 36. Immunofluorescence images of 3D invasion HAP-1 Parental or HAP-1 QSOX1 KO incubated without primary antibody (secondary antibody only control). Images were taken at the highest exposure used in obtaining the images for laminin α 4, fibronectin, nidogen (α Mouse), or versican (α Goat). Phalloidin Alexa Fluor-488 was utilized as a counterstain to visualize F-actin organization. Images were obtained on a Zeiss LSM 800 confocal microscope on the 63X oil objective. Treated cells versus their controls were imaged at the same fluorescent intensity. Scale bar = 10 μ m.

Conclusions:

SBI-183 was initially identified as a lead anti-QSOX1 compound exhibiting anti-tumorigenic effects, yet it was limited by high IC_{50} values. Our subsequent lead optimization protocol identified SPX-009 as the top QSOX1 inhibitory small molecule from a library of seventy-one novel analogs.

While SPX-009 suppressed 3D invasion more strongly than did SBI-183, we found it interesting that, though statistically significant, inhibition due to QSOX1 knockdown was not as potent as that observed in cells dosed with SPX-009 (-24% in

MDA-MB-231 sh742 versus -63% in MDA-MB-231 + 1.25 μ M SPX-009, and -26% in MIA PaCa2 sh742 versus -45% in MIA PaCa2 + 1.25 μ M SPX-009). Additionally, in our MTT assays, shKnockdown's of QSOX1 did not inhibit proliferation, while SPX-009 did. Interestingly, these data agree with recent literature in which inhibition of QSOX1 enzymatic activity with a monoclonal antibody did not affect proliferation of the mouse breast cancer cell line 4T1 when grown in culture, but tumors in mice treated with the same were smaller than controls. This was considered indicative of QSOX1's interaction with a proper microenvironment (148). Taken together, these data suggest that, similar to SBI-183 (27) and numerous other small molecules (177), SPX-009 has other targets within cells in addition to QSOX1. We utilized GraphPad Prism to determine if there was a correlation between QSOX1 secretion and SPX-009 IC₅₀'s in 3D invasion and proliferation (Figure 37). The p value for correlation in 3D invasion was .0573, while the p value for correlation in proliferation was .2954 indicating that QSOX1 secretion and SPX-009 IC₅₀'s were not correlated. However, these results do lend additional support for the hypothesis that SPX-009 does have other targets within cells. Inhibition of multiple cellular targets would compound the observed inhibitory phenotype. Another possible explanation for the apparent discrepancies observed in the shKnockdown's and SPX-009 treated cells is that cell lines differentially rely on QSOX1 enzymatic activity. Of all cell lines tested, MDA-MB-231 consistently had the highest levels of QSOX1 secreted into the supernatant, while MIA PaCa2 consistently had lower levels. However, tumors are well known to be genetically unstable, leading to the random overexpression of numerous proteins (189). Therefore, while MDA-MB-231 secretes high levels of QSOX1, it may not heavily rely on its activity for 3D invasion or proliferation. In contrast, while MIA

PaCa2 secretes much lower levels of QSOX1, it may be “addicted” to QSOX1 activity in 3D invasion or proliferation (190,191). Further research is required to determine the extent of tumor cell reliance on QSOX1 enzymatic activity in the various aspects of the cancer phenotype.

While SPX-009 likely has other cellular targets than QSOX1, it is still certainly active on QSOX1 as determined by our 3D rescue invasion assays (Figure 21) and by our 3D invasion assays with compounds that were inactive in the QSOX1 enzymatic activity assay (Figure 22). In our 3D rescue invasion assay, addition of a four-fold molar excess of QSOX1 to SPX-009 yielded a 16% increase in invasion of MDA-MB-231 (Figure 21A). Addition of a two-fold molar excess of QSOX1 to SPX-009 yielded a 17% and 19% increase in invasion of MIA PaCa2 and RCJ-41T2, respectively (Figure 21B, C). As discussed with SBI-183, the likely reason for only a partial rescue of invasion is because addition of exogenous rQSOX1 only overcomes the effects of external small molecule inhibitors against external QSOX1 (27). Small molecules can additionally enter the cell and therefore also inhibit intracellular QSOX1, while exogenously added rQSOX1 cannot enter the cell. As an additional line of evidence for QSOX1 as a cellular target of SPX-009 in 3D invasion, we utilized two other analogs of SBI-183 which did not have activity in the HVA fluorescence assay against QSOX1: SPX-006 and SPX-007 (see Table 6 for chemical structures). As seen in Figure 22, both compounds display a statistically significant reduction in 3D invasion inhibition in all cell lines tested, as compared to SBI-183. At 10 μ M, SPX-006 inhibition of invasion looked essentially the same as the DMSO vehicle control in all cell lines. SPX-007, also at 10 μ M, did display some inhibition of invasion, however this inhibition, is statistically significantly less than that observed in

SBI-183. Further, it is important to note that both compounds were tested at 10 μ M, while SPX-009 at that same concentration inhibited invasion considerably. Taken together, these data suggest that QSOX1 is a cellular target of SPX-009 because A) addition of exogenous rQSOX1 partially rescued the invasive phenotype, and B) analogs which were inactive in the HVA fluorescence assay were also inactive in the 3D invasion assay.

Further lead optimization studies were performed on SBI-183 analogs synthesized by Sapphire Biotech by screening for cellular activity in the 3D invasion assay (Figure 23A, C, C1, E, E1). Only AM-2172, SPX-5226, and SPX-5179 displayed inhibitory activity. AM-2172 contains the addition of a fluorine on the permissive benzene ring of SPX-009 and was purposely synthesized for use in F19 NMR studies as a spy molecule analog of SPX-009. Similar to ebselen and SBI-183 (27,139), these future NMR studies will be important in QSOX1 enzymology. This is because small molecules have the potential for highly targeted protein binding. The small molecule can bind directly to the target in a location that A) directly inhibits protein-protein interaction (QSOX1 binding to substrate), B) directly inhibits enzymatic activity (ability of QSOX1 to perform electrophilic attack on substrate sulfhydryls and subsequent electron shuttling), or C) binds outside of any active site, but the binding causes changes in protein conformation and/or dynamics, inhibiting activity (192). SPX-5226 is an analog of SPX-009 containing three ethoxy groups off the permissive benzene ring. SPX-5179 is the first molecule tested which contained a change to the pyrrolidine ring which did not abolish activity. The specific reasons for why the chemical modifications of SPX-009, SPX-5226, and SPX-5179 are active is currently unknown. More work is needed to elucidate this, as well

as what other modifications can be made which increase inhibitory activity. While none of the tested compounds were as universally inhibitory as SPX-009, they do begin to allow us some insight into chemical modifications that may be made to further increase potency.

To examine the biology of QSOX1 inhibition, we first looked at expression of sulfhydryl oxidases that shared some similarity to QSOX1. There is high redundancy of cellular sulfhydryl oxidases, therefore it seems possible that inhibition of one sulfhydryl oxidase that is overexpressed by tumor cells (Figure 27) would lead to overexpression of another sulfhydryl oxidase. Additionally, ERO1 α was overexpressed in the hearts of QSOX1^{-/-} mice (193). Here we tested three sulfhydryl oxidases which are related to the cancer phenotype, and which share some similarity to QSOX1: PDI, ERO1 α , and ALR. Interestingly, in the presence of QSOX1 inhibition, we did not observe overexpression of any of these enzymes (Figure 28). Because QSOX1^{-/-} mice overexpressed ERO1 α in heart tissue, and we did not observe a similar increase in any tumor cell line, this suggests that expression of sulfhydryl oxidases may be cell type dependent. As mentioned, there are numerous other sulfhydryl oxidases within cells- therefore it is still possible that inhibition of QSOX1 enzymatic activity does lead to overexpression of a sulfhydryl oxidase not tested here. The fact that we did not observe the upregulation of another sulfhydryl oxidase upon QSOX1 inhibition supports the role of QSOX1 as a master regulator of the ECM, making it an attractive target in anticancer therapeutics.

Cancer cells are heavily influenced by their microenvironment, including signaling for proliferation, migration, and invasion (11,12). Previous work has shown QSOX1 modulation of the ECM via deposition of laminin α 4 and changes in matrix

integrity via fibronectin (27,145,147,148), therefore we sought to begin characterization of tumor ECM on cells grown in 3D. In addition to examining laminin $\alpha 4$ and fibronectin, we also stained for nidogen (involved in laminin polymerization and ECM incorporation (185)) and versican (involved in tumor progression, invasion, and EMT (187,188)) due to the observed role of QSOX1 in tumor invasion and metastasis (27,148). Immunofluorescent staining on each of our cell lines for fibronectin, nidogen, and versican did not reveal any consistent changes in the treated cells versus controls. However, in our cell lines with genetic modulation of QSOX1 expression (short hairpin MDA-MB-231, short hairpin MIA PaCa2, and HAP-1) we observed statistically significant reductions in deposition of laminin $\alpha 4$ in the ECM of the treated compared to the shScramble or Parental controls, agreeing with the current literature (Figure 29). In cells that were treated with SPX-009 we expected to see this same reduction when compared to the DMSO control. Instead, we observed a statistically significant increase in intensity signal in SPX-009 treated MDA-MB-231 cells. We also observed an increase in signal in SPX-009 treated MIA PaCa2 cells, however this was not statistically significant. In addition to the increases in intensity, we also noted disorganization of laminin $\alpha 4$, including concentration of the staining and a whirling pattern (Figure 30). Observation of our F-actin counterstains revealed some similar disorganization, especially in MIA PaCa2 SPX-009 treated cells (Figure 31). α -dystroglycan is a cell-surface associated laminin receptor which interacts with F-actin via transmembrane β -dystroglycan (194). The disorganization of intracellular F-actin and subsequent modified organization of laminin $\alpha 4$ is likely responsible for the increased laminin $\alpha 4$ intensity (concentration) and disorganization (Figure 29). The extreme disorganization observed in

MIA PaCa2 could also explain the smaller, denser spheroids observed when this cell line was incubated with SPX-009 during spheroid formation (Figure 24). The minor disorganization of F-actin observed in MDA-MB-231 by immunofluorescence is also consistent with the minor reduction in initial spheroid formation when treated with SPX-009 (Figure 24). F-actin does contain intermolecular disulfide bonds, however, the formation and disassembly of filamentous actin is modulated through the activity of Rho GTPases (195) in the cytoplasm. Because QSOX1 is found primarily in the Golgi and secreted (126), it seems unlikely that it is involved in the formation of F-actin. As mentioned previously, SPX-009 likely has cellular targets in addition to anti-QSOX1 activity, similar to other small molecules (27,177). Our immunofluorescence results may be indicative of other cellular targets of SPX-009, which is corroborated by our data showing no correlation between QSOX1 expression and inhibition of proliferation or 3D invasion with SPX-009 (Figure 37). Due to their role in tumor progression and metastasis, cytoskeletal components are an emerging area of research in anti-cancer therapeutics. Two such recent targets which interact with F-actin are fascin and CapG. Fascin is involved in F-actin bundling and its inhibition was observed to block invasion and metastasis of MDA-MB-231 and the mouse 4T1 mammary gland cell line (196,197). CapG binds reversibly to the end of F-actin. Inhibition of CapG with a nanobody resulted in a decrease in invasion and metastasis of MDA-MB-231 (198). If SPX-009 is indeed interacting with a cytoskeleton component in addition to QSOX1, any specific biological modulations that are due to QSOX1 activity alone would be difficult to identify.

In summary, here we begin to address chemical modifications to the small molecule SBI-183 resulting in a novel top hit, SPX-009, which cause it to inhibit QSOX1

cell-free enzymatic activity and cancer cell invasion more strongly. We note modifications to the non-permissive pyrrolidine ring may be possible if they make this structure more flexible. Further work is needed to fully elucidate the range of modifications that can be made to SBI-183 and retain or increase anti-QSOX1 cellular activity. Additionally, more work is needed to exchange the peptide bond located between the two benzenes for a structure that is not readily cleaved *in vivo*. Our data provide further evidence for the pro-tumorigenic role of QSOX1. Short hairpin knockdown or KO of QSOX1 resulted in a decrease in deposition of laminin $\alpha 4$ in the ECM of three different cell lines. Inhibition of QSOX1 via the small molecule SPX-009 reduces invasion in an *in vivo*-like, 3D model. This invasion was partially rescued by the addition of exogenous rQSOX1, indicating that QSOX1 is a cellular target of SPX-009. However, our immunofluorescence data on 3D invaded spheroids indicates that SPX-009 may additionally be targeting components of the cytoskeleton, contributing to the observed phenotype.

SPX-009 IC_{50} and QSOX1 secretion correlation.

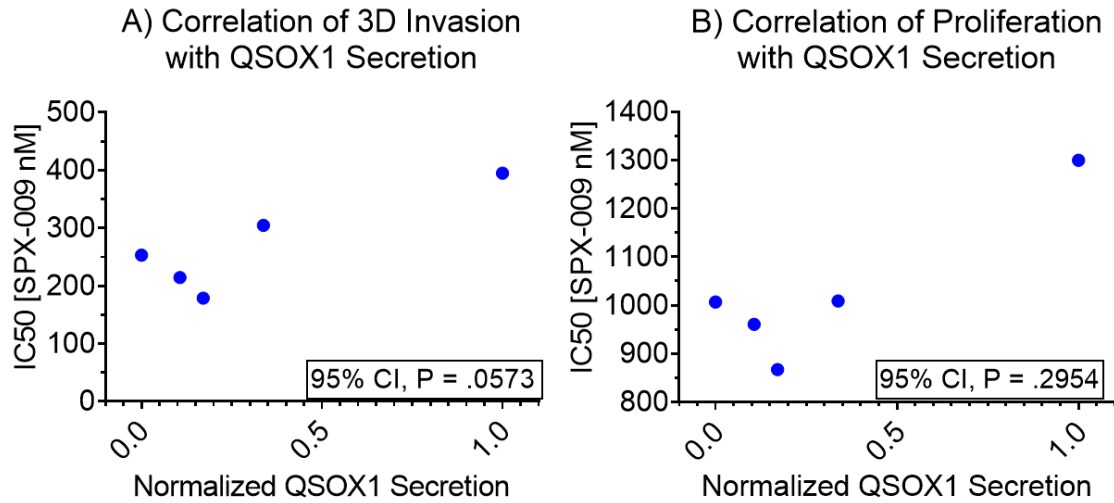


Figure 37. SPX-009 IC_{50} 's in 3D invasion and proliferation do not correlate with QSOX1 expression. Total QSOX1 in the supernatant of five cell lines (points on graph from left to right: A549, Panc1, MIA PaCa2, RCJ-41T2, and MDA-MB-231) was measured by capture ELISA, normalized, and plotted against IC_{50} values for 3D invasion (A) and proliferation (B). Correlation was determined using GraphPad Prism.

CHAPTER 5

DISCUSSION AND CONCLUSIONS

Traditional cancer treatments center around conventional chemotherapy in which cytotoxic drugs kill rapidly proliferating tumor cells. A major drawback of this method is the lack of specificity of cytotoxic drugs for cancer cells, killing normal cells in the process (199). As our understanding of the processes driving tumor growth expanded, targeted chemotherapy arose. In targeted chemotherapy, a drug specific for an individual tumor-derived protein upon which tumor growth is dependent is utilized to kill cancer cells with increased precision (200). For targeted chemotherapy to be effective, the context of vulnerability of the patient's tumor must be known (i.e. genomic, transcriptomic, and proteomic sequencing to identify mutational vulnerabilities). A major drawback of the targeted therapy method is that a single biomarker may only be involved in one or two molecular pathways. Depending on the pathway inhibited, this means that targeting a single marker by itself may not be enough to stop the spread of cancer. Additionally, the heterogeneity of tumors makes them extremely difficult to treat, as there is not a "one size fits all" regimen that is effective on all tumors. This heterogeneity gives rise to drug resistance, a common result of single drug cancer treatments. Drug resistance occurs when an anti-neoplastic agent kills all the cancer cells which express the marker it is effective against, leaving only those cells without that marker to survive and proliferate. Modern chemotherapy tactics have shifted to include combination chemotherapy. This approach utilizes two or more anti-cancer drugs to attack two or more tumor-specific targets at once, decreasing potential resistance while inhibiting multiple molecular pathways (201). With the rise in monoclonal antibody cancer

therapies, including monoclonal antibodies conjugated to drugs, tumor markers are routinely utilized when determining the best combination therapy for a patient. In the ongoing fight against cancer, it is therefore imperative to continue to grow our understanding of tumor biology, identifying potential novel cancer markers, and identifying small molecules or antibodies to target them. To that end, this work sought to further our knowledge of one understudied potential cancer marker, QSOX1, deepening our understanding of the role of QSOX1 in the cancer phenotype.

QSOX1 is an emerging cancer-associated enzyme which is overexpressed in many different tumor types (27,139,140,144,146,148–155). Through its oxidation of free thiols to form disulfide bonds, it acts on client substrates to help fold them into their proper shape in the Golgi or ECM (124–126,128–138). Here we characterize two novel inhibitors of QSOX1 enzymatic activity: SBI-183 and its analog SPX-009 (Figure 1, Figure 14, Figure 15). For this work, it was important to study three things: binding of the small molecules to QSOX1, inhibition of QSOX1 enzymatic activity, and inhibition of invasion/metastasis.

Our work demonstrates that SBI-183 binds to and inhibits the enzymatic activity of QSOX1 (Figure 1). Current work is underway utilizing NMR to determine the binding location of SPX-009 to QSOX1. Like ebselen, the binding location of SBI-183 was shown to be near C237 (27,139). The identification of this cysteine as a binding location for two independent QSOX1 small molecule inhibitors indicates it is a potential substrate binding location, as this cysteine is not thought to be involved in QSOX1 enzymatic activity (129,137). Another possibility is that, as hypothesized with ebselen, binding of SBI-183 to this cysteine hampers the flexibility of the QSOX1 disordered region which

functions like a hinge such that the Trx1 domain is unable to come into close proximity with the ERV domain to ultimately transfer electrons to the FAD domain (139). Future studies will be required to assess these hypotheses and determine the mechanism of action of SBI-183 and SPX-009 inhibition of QSOX1 activity.

Next, we studied the effects of SBI-183 and SPX-009 on cells. Invasion, a precursor to metastasis, is commonly studied in the lab utilizing a Boyden chamber, 2D microenvironment. In this assay, cells invade from a serum free media chamber, through a Matrigel coated membrane, and into a chamber containing serum, following a nutrient gradient. This assay typically takes less than 24 hours, so that proliferation is not a factor in quantification of the results. In this model of invasion, we observed that both SBI-183 and SPX-009 inhibited the invasion of all cell lines (Figure 3, Figure 20), with SPX-009 doing so at lower concentrations than SBI-183. In addition to the 2D classical model, we extensively utilized a 3D invasion assay in which cells invaded from a tumoroid or spheroid into the surrounding Matrigel matrix (30,175). Because cancer spheroids have proper intercellular communication, and because a compound must diffuse through layers of cells in order to effect those in the center, the 3D nature of this tumor microenvironment allowed for a more biologically relevant model to study cancer invasion. We noted that in all cell lines tested, SPX-009 again more potently inhibited invasion in this model than did SBI-183 (Figure 3, Figure 12, Figure 17, Figure 18). This inhibition was likely due to a malformed ECM (Figure 29) via deposition of laminin $\alpha 4$. Future work should focus on optimizing co-culture methods, expanding the presented monoculture conditions to include the microenvironmental interactions between tumor

cells and their supporting “normal” stromal cells. With proper controls, the 3D invasion model is a robust measure of tumor invasion *in vitro*.

In addition to standard invasion assays, we also performed 3D rescue invasion assays, in which rQSOX1 was added exogenously to wells containing SBI-183 or SPX-009 to “rescue” the invasive cancer phenotype. These “rescues” were only partially effective (Figure 5, Figure 21). This could be due to the inability of exogenous QSOX1 to enter cells where small molecules are likely inhibiting QSOX1 in the ER and Golgi. In conjunction with this, another possibility is that the partial rescue could be due to the tendency for small molecules to interact with cellular targets in addition to QSOX1 (177). In support of this idea, we observed that inhibition of QSOX1 expression by shKnockdown or KO resulted in a decrease in laminin $\alpha 4$ staining intensity in the ECM of three tested cell lines in a 3D invasion model when compared to controls (Figure 29), which is in agreement with the literature (27,145). In contrast, however, staining for laminin $\alpha 4$ in the ECM of SPX-009 treated 3D invaded cells resulted in an increase in intensity as compared to the controls, likely due to aberrant concentration of the protein, resulting in a more intense signal (Figure 29, Figure 30). Study of the pattern of laminin $\alpha 4$ organization under these conditions revealed disorganization that was similar to that observed with F-actin (Figure 31). Because QSOX1 is localized to the Golgi and is secreted (126), while G-actin forms F-actin in the cytoplasm (195), it seems unlikely that SPX-009 would disrupt F-actin formation via inhibition of QSOX1. This suggests that SPX-009 is inhibiting the proper formation of the ECM through QSOX1 inhibition as described above, and possibly also targeting a cytoskeletal component. Further work

might characterize all cellular targets of SPX-009 since it may have activity against non-QSOX1 proteins.

We next extended our findings to mouse models. In agreement with current literature, we observed that inhibition of QSOX1 enzymatic activity with the small molecule SBI-183 was not toxic to athymic nude mice (Table 3), and resulted in a decrease in tumor volume in a RCC xenograft model, and in a sarcomatoid RCC xenograft model (Figure 7) (139,148,149). Metastasis of a TNBC was also reduced following inhibition of QSOX1 enzymatic activity (Figure 13). These results are further corroborated by our previous publications and that of other groups showing that QSOX1 promotes metastasis (153), and that inhibition of QSOX1 activity with a monoclonal antibody reduces metastasis in a mouse breast cancer model (148). Inhibition of the cancer phenotype in mice is partially due to a malformed tumor ECM via laminin α 4 deposition (Figure 8), (145,147).

Currently work is underway to determine the pharmacokinetics of SPX-009 in a murine model. Future work will characterize the toxicity, anti-proliferative, and anti-metastatic properties of SPX-009 *in vivo*. Because current literature suggests that QSOX1 is involved in metastasis, it would be prudent to perform a large-scale study on the expression of QSOX1 in primary tumors vs. matched metastatic sites to deepen our understanding of its biology.

In addition to our study of invasion and metastasis with SBI-183 and SPX-009, we also examined cellular viability when QSOX1 was inhibited. Treatment with SBI-183 and SPX-009 resulted in a decrease in cellular viability (Figure 2, Figure 25). In the stable shKnockdown cell line 786-O sh742.E11, a decrease in cellular viability was also noted (Figure 2). These findings agree with much of the current literature regarding the

involvement of QSOX1 in tumor viability (27,139,146,149,151). However, in some tumor cell lines, we did not observe any change in viability. In MDA-MB-231 and MIA PaCa2 shKnockdown cells, tumor cell viability was not affected (Figure 25), but we did observe a reduction in 3D invasion of these same cells (Figure 17). Two other groups observed a similar phenomenon in Lewis lung cancer (LLC) (153) and in a mouse breast cancer (4T1) (148). In the LLC model, no difference in proliferation was observed in their QSOX1 shKnockdown vs. their controls, however in their mouse model with the same, QSOX1 shKnockdown tumors were smaller than controls. In the 4T1 breast cancer model, no inhibition of viability was observed when an anti-QSOX1 monoclonal antibody was incubated with 4T1 cells in culture. They did, however, observe a reduction in tumor volume when mice bearing 4T1 tumors were dosed with this same antibody (148). These data point to the importance of studying QSOX1 in a biologically relevant model. A properly formed tumor microenvironment appears to be essential when studying QSOX1 and will be crucial in the elucidation of QSOX1's *in vivo* substrates. These data also suggest that tumor cell lines may differentially rely on QSOX1 enzymatic activity under different growth conditions.

Structurally, a major drawback of both SBI-183 and SPX-009 is their shared peptide bond, located between the two benzenes (Figure 9, Figure 16). This is because this bond is readily cleaved *in vivo* resulting in a loss of bioavailability of the compound. Our collaborators at Sapphire Biotech synthesized a number of analogs in which this peptide bond was replaced with a sulfonamide (Table 6), however this particular substitution routinely resulted in a loss of cellular activity (Figure 23). It will be important to synthesize a molecule which does not contain the amide linkage, and which

is active on cells. Further chemical synthesis should center on the creation of sulfonamides with additional active chemical modifications as noted in Figure 23. For instance, SPX-5226, while not as inhibitory as SPX-009, might provide a pathway for synthesis of new analogs resistant to breakdown while retaining activity. Synthesis of an analog containing three ethoxy groups on the permissive benzene with a sulfonamide linkage may prove active. Alternatively, there are numerous other amide bond surrogates which are utilized in medicinal chemistry other than sulfonamides including alkenes, fluoroalkenes, ketomethylenes, depsipeptides, methyleneaminos, and trifluoroethylamines, to name just a few (202). Any one of these may increase inhibition of QSOX1 enzymatic activity and prove inhibitory on cells, while remaining biologically available.

As mentioned numerous times in this work, the direct, *in vivo* substrates of QSOX1 are unknown. It is thought that QSOX1 is involved in incorporation of the pro-invasive ECM component laminin $\alpha 4$ into the ECM of WI38 fibroblasts (145) and a sarcomatoid renal cell carcinoma, RCJ-41T2 (27). Additionally, inhibition of QSOX1 with a monoclonal antibody caused disorganization of fibronectin in the ECM of WI38 fibroblasts (147) and in murine breast cancer models (148). While the disarray of these ECM components might suggest that they are direct substrates of extracellular QSOX1, in the case of laminin at least, this is unlikely. Laminins are assembled intracellularly, and are not secreted until incorporation of the alpha chain occurs (203–205). Further, in the WI38 model in which QSOX1 had been knocked down with a siRNA, laminin $\alpha 4$ was identified in its complete, heterotrimeric form. Only its localization (in the supernatant instead of incorporated into the ECM) was abnormal (145). Additionally,

maleimide-gold labelling followed by scanning electron microscopy identified QSOX1 target cysteines in the defined ECM of these cells, rather than on laminin scaffolding sites on the cell membrane. The authors suggest that extracellular QSOX1 is required for incorporation of laminin α 4 into the ECM, rather than being required for its folding (145). Regarding fibronectin organization, it may be possible that fibronectin is an *in vivo* substrate of QSOX1 via interaction with the QSOX1 cis-proline loop. However, directly observing the interaction of QSOX1 with its substrates via classic thiol trapping has proven elusive (147). Further work to identify the *in vivo* substrates is required. Because an increase in free sulfhydryls has been observed in the ECM of cells treated with RNAi for QSOX1 (145), it has been suggested to utilize maleimide conjugated to biotin to label these free thiols for identification (206). An additional possibility would be to utilize the high throughput Nucleic Acid Programmable Protein Array – Surface Plasmon Resonance imaging (NAPPA-SPRi) system (207–209) followed by confirmation of the *in vivo* relevance of the identified substrates with FRET microscopy. These methods would inform on the potential substrates of QSOX1, deepening our understanding of QSOX1 biology in both normal and cancer cells.

Here we establish that inhibition of QSOX1 enzymatic activity utilizing small molecules or shRNA leads to a reduction in tumor invasion *in vitro*, and tumor growth and metastasis *in vivo*, through modulation of tumor ECM via laminin α 4 deposition. Due to its overexpression in and promotion of numerous cancers (27,139,140,144,146,148–155), QSOX1 is an exciting potential therapeutic target. Future research should focus on the elucidation of the tumor biology of QSOX1 in a biologically relevant molecular context as well as full characterization of QSOX1 small molecule

inhibitors as probes to reveal mechanism of action. Since 90% of patient deaths are due to metastasis, complete understanding of the role of QSOX1 in cancer has the potential to preserve patient lives.

REFERENCES

1. Siegel RL, Miller KD, Jemal A. Cancer statistics, 2020. *CA Cancer J Clin* [Internet]. 2020 Jan 1;70(1):7–30. Available from: <https://doi.org/10.3322/caac.21590>
2. Kamb A, Wee S, Lengauer C. Why is cancer drug discovery so difficult? *Nat Rev Drug Discov* [Internet]. 2007;6(2):115–20. Available from: <https://doi.org/10.1038/nrd2155>
3. Hanahan D, Weinberg RA. Hallmarks of Cancer: The Next Generation. *Cell* [Internet]. 2011 Mar 4;144(5):646–74. Available from: <https://doi.org/10.1016/j.cell.2011.02.013>
4. Venning FA, Wullkopf L, Erler JT. Targeting ECM Disrupts Cancer Progression. *Front Oncol* [Internet]. 2015 Oct 20;5:224. Available from: <https://www.ncbi.nlm.nih.gov/pubmed/26539408>
5. Carter SK. The Search for Therapeutic Cell Controls by the Chemotherapy Program of the National Cancer Institute. *J Invest Dermatol* [Internet]. 1972 Jul 1 [cited 2020 Apr 21];59(1):128–38. Available from: <https://www.sciencedirect.com/science/article/pii/S0022202X15481898>
6. Moffat JG, Rudolph J, Bailey D. Phenotypic screening in cancer drug discovery — past, present and future. *Nat Rev Drug Discov* [Internet]. 2014;13(8):588–602. Available from: <https://doi.org/10.1038/nrd4366>
7. AL-Busairi W. The Principles behind Targeted Therapy for Cancer Treatment. In: Cohen-Solal MKE-ALE-K, editor. Rijeka: IntechOpen; 2020. p. Ch. 8. Available from: <https://doi.org/10.5772/intechopen.86729>
8. Schenone M, Dančik V, Wagner BK, Clemons PA. Target identification and mechanism of action in chemical biology and drug discovery. *Nat Chem Biol* [Internet]. 2013;9(4):232–40. Available from: <https://doi.org/10.1038/nchembio.1199>
9. Hoelder S, Clarke PA, Workman P. Discovery of small molecule cancer drugs: Successes, challenges and opportunities. *Mol Oncol* [Internet]. 2012 Apr 1 [cited 2020 Jul 8];6(2):155–76. Available from: [/pmc/articles/PMC3476506/?report=abstract](https://pubmed.ncbi.nlm.nih.gov/22111111/)
10. Walker C, Mojares E, Del Río Hernández A. Role of Extracellular Matrix in Development and Cancer Progression. *Int J Mol Sci* [Internet]. 2018 Oct 4;19(10):3028. Available from: <https://pubmed.ncbi.nlm.nih.gov/30287763>
11. Levental KR, Yu H, Kass L, Lakins JN, Egeblad M, Erler JT, et al. Matrix

- Crosslinking Forces Tumor Progression by Enhancing Integrin Signaling. *Cell*. 2009 Nov 25;139(5):891–906.
12. Jodele S, Blavier L, Yoon JM, DeClerck YA. Modifying the soil to affect the seed: Role of stromal-derived matrix metalloproteinases in cancer progression. Vol. 25, *Cancer and Metastasis Reviews*. Springer; 2006. p. 35–43.
 13. Lo CM, Wang HB, Dembo M, Wang YL. Cell movement is guided by the rigidity of the substrate. *Biophys J*. 2000 Jul 1;79(1):144–52.
 14. Singleton PA, Mirzapozova T, Guo Y, Sammani S, Mambetsariev N, Lennon FE, et al. High-molecular-weight hyaluronan is a novel inhibitor of pulmonary vascular leakiness. *Am J Physiol Lung Cell Mol Physiol* [Internet]. 2010/08/13. 2010 Nov;299(5):L639–51. Available from: <https://pubmed.ncbi.nlm.nih.gov/20709728>
 15. Mambetsariev N, Mirzapozova T, Mambetsariev B, Sammani S, Lennon FE, Garcia JGN, et al. Hyaluronic Acid binding protein 2 is a novel regulator of vascular integrity. *Arterioscler Thromb Vasc Biol* [Internet]. 2009/12/30. 2010 Mar;30(3):483–90. Available from: <https://pubmed.ncbi.nlm.nih.gov/20042707>
 16. Simpson-Haidaris PJ, Rybarczyk B. Tumors and Fibrinogen. *Ann N Y Acad Sci* [Internet]. 2001 Jun 1;936(1):406–25. Available from: <https://doi.org/10.1111/j.1749-6632.2001.tb03525.x>
 17. Amo L, Tamayo-Orbegozo E, Maruri N, Eguizabal C, Zenarruzabeitia O, Riñón M, et al. Involvement of platelet-tumor cell interaction in immune evasion. Potential role of podocalyxin-like protein 1. *Front Oncol* [Internet]. 2014 Sep 11;4:245. Available from: <https://pubmed.ncbi.nlm.nih.gov/25309871>
 18. Rybarczyk BJ, Simpson-Haidaris PJ. Fibrinogen Assembly, Secretion, and Deposition into Extracellular Matrix by MCF-7 Human Breast Carcinoma Cells. *Cancer Res* [Internet]. 2000 Apr 1;60(7):2033 LP – 2039. Available from: <http://cancerres.aacrjournals.org/content/60/7/2033.abstract>
 19. Lowy CM, Oskarsson T. Tenascin C in metastasis: A view from the invasive front. *Cell Adh Migr* [Internet]. 2015;9(1–2):112–24. Available from: <https://pubmed.ncbi.nlm.nih.gov/25738825>
 20. González-González L, Alonso J. Periostin: A Matricellular Protein With Multiple Functions in Cancer Development and Progression. *Front Oncol* [Internet]. 2018 Jun 12;8:225. Available from: <https://pubmed.ncbi.nlm.nih.gov/29946533>
 21. Barkan D, Kleinman H, Simmons JL, Asmussen H, Kamaraju AK, Hoenorhoff MJ, et al. Inhibition of metastatic outgrowth from single dormant tumor cells by targeting the cytoskeleton. *Cancer Res* [Internet]. 2008 Aug 1;68(15):6241–50. Available from: <https://pubmed.ncbi.nlm.nih.gov/18676848>

22. Soikkeli J, Podlasz P, Yin M, Nummela P, Jahkola T, Virolainen S, et al. Metastatic outgrowth encompasses COL-I, FN1, and POSTN up-regulation and assembly to fibrillar networks regulating cell adhesion, migration, and growth. *Am J Pathol* [Internet]. 2010/05/20. 2010 Jul;177(1):387–403. Available from: <https://pubmed.ncbi.nlm.nih.gov/20489157>
23. Birgersdotter A, Sandberg R, Ernberg I. Gene expression perturbation in vitro—A growing case for three-dimensional (3D) culture systems. *Semin Cancer Biol* [Internet]. 2005 Oct 1 [cited 2020 Apr 17];15(5):405–12. Available from: <https://www.sciencedirect.com/science/article/pii/S1044579X05000416?via%3Dihub>
24. Bhadriraju K, Chen CS. Engineering cellular microenvironments to improve cell-based drug testing. *Drug Discov Today* [Internet]. 2002 May 6 [cited 2020 Apr 17];7(11):612–20. Available from: <https://www.sciencedirect.com/science/article/pii/S1359644602022730?via%3Dihub>
25. Weaver VM, Petersen OW, Wang F, Larabell CA, Briand P, Damsky C, et al. Reversion of the malignant phenotype of human breast cells in three-dimensional culture and in vivo by integrin blocking antibodies. *J Cell Biol* [Internet]. 1997 Apr 7;137(1):231–45. Available from: <https://pubmed.ncbi.nlm.nih.gov/9105051>
26. Duval K, Grover H, Han L-H, Mou Y, Pegoraro AF, Fredberg J, et al. Modeling Physiological Events in 2D vs. 3D Cell Culture. *Physiology (Bethesda)* [Internet]. 2017 Jul;32(4):266–77. Available from: <https://pubmed.ncbi.nlm.nih.gov/28615311>
27. Fifield AL, Hanavan PD, Faigel DO, Sergienko E, Bobkov A, Meurice N, et al. Molecular Inhibitor of QSOX1 Suppresses Tumor Growth in vivo. *Mol Cancer Ther* [Internet]. 2019 Jan 1;molcanther.0233.2019. Available from: <http://mct.aacrjournals.org/content/early/2019/10/01/1535-7163.MCT-19-0233.abstract>
28. Edmondson R, Broglie JJ, Adcock AF, Yang L. Three-dimensional cell culture systems and their applications in drug discovery and cell-based biosensors. *Assay Drug Dev Technol* [Internet]. 2014 May 1;12(4):207–18. Available from: <https://www.ncbi.nlm.nih.gov/pubmed/24831787>
29. Batchelder CA, Martinez ML, Duru N, Meyers FJ, Tarantal AF. Three Dimensional Culture of Human Renal Cell Carcinoma Organoids. *PLoS One* [Internet]. 2015 Aug 28;10(8):e0136758. Available from: <https://doi.org/10.1371/journal.pone.0136758>
30. Benton G, George J, Kleinman HK, Arnaoutova IP. Advancing science and technology via 3D culture on basement membrane matrix. *J Cell Physiol* [Internet]. 2009 Oct 1;221(1):18–25. Available from:

<https://doi.org/10.1002/jcp.21832>

31. Hopkins AL. Network pharmacology: the next paradigm in drug discovery. *Nat Chem Biol* [Internet]. 2008;4(11):682–90. Available from: <https://doi.org/10.1038/nchembio.118>
32. Kim JW, Ho WJ, Wu BM. The role of the 3D environment in hypoxia-induced drug and apoptosis resistance. *Anticancer Res*. 2011 Oct 1;31(10):3237–45.
33. Sevier CS, Cuzzo JW, Vala A, Åslund F, Kaiser CA. A flavoprotein oxidase defines a new endoplasmic reticulum pathway for biosynthetic disulphide bond formation. *Nat Cell Biol* [Internet]. 2001;3(10):874–82. Available from: <https://doi.org/10.1038/ncb1001-874>
34. Faccio G, Nivala O, Kruus K, Buchert J, Saloheimo M. Sulfhydryl oxidases: sources, properties, production and applications. *Appl Microbiol Biotechnol* [Internet]. 2011;91(4):957–66. Available from: <https://doi.org/10.1007/s00253-011-3440-y>
35. Wilkinson B, Gilbert HF. Protein disulfide isomerase. *Biochim Biophys Acta - Proteins Proteomics*. 2004 Jun 1;1699(1–2):35–44.
36. Munro S, Pelham HRB. A C-Terminal Signal Prevents Secretion of Luminal ER Proteins. Vol. 48, *Cell*. 1987.
37. Terada K, Manchikalapudi P, Noiva R, Jauregui HO, Stockert RJ, Schilsky ML. Secretion, surface localization, turnover, and steady state expression of protein disulfide isomerase in rat hepatocytes. *J Biol Chem*. 1995 Sep 1;270(35):20410–6.
38. Bi S, Hong PW, Lee B, Baum LG. Galectin-9 binding to cell surface protein disulfide isomerase regulates the redox environment to enhance T-cell migration and HIV entry. *Proc Natl Acad Sci* [Internet]. 2011 Jun 28 [cited 2020 Apr 28];108(26):10650–5. Available from: <http://www.pnas.org/cgi/doi/10.1073/pnas.1017954108>
39. Mezghrani A, Courageot J, Mani JC, Pugniere M, Bastiani P, Miquelis R. Protein-disulfide Isomerase (PDI) in FRTL5 Cells. *J Biol Chem* [Internet]. 2000 Jan 21 [cited 2020 Apr 28];275(3):1920–9. Available from: <http://www.jbc.org/lookup/doi/10.1074/jbc.275.3.1920>
40. Freedman RB, Hirst TR, Tuite MF. Protein disulphide isomerase: building bridges in protein folding. Vol. 19, *Trends in Biochemical Sciences*. Elsevier Current Trends; 1994. p. 331–6.
41. Benham AM, Cabibbo A, Fassio A, Bulleid N, Sitia R, Braakman I. The CXXCXXC motif determines the folding, structure and stability of human Ero1- α . *EMBO J* [Internet]. 2000 Sep 1;19(17):4493–502. Available from:

<https://pubmed.ncbi.nlm.nih.gov/10970843>

42. Van Anken E, Braakman I. Versatility of the endoplasmic reticulum protein folding factory. Vol. 40, *Critical Reviews in Biochemistry and Molecular Biology*. 2005. p. 191–228.
43. Araki K, Iemura S, Ichiro, Kamiya Y, Ron D, Kato K, Natsume T, et al. Ero1- α and pdis constitute a hierarchical electron transfer network of endoplasmic reticulum oxidoreductases. *J Cell Biol*. 2013 Sep 16;202(6):861–74.
44. Rickman DS, Bobek MP, Misek DE, Kuick R, Blaivas M, Kurnit DM, et al. Distinctive Molecular Profiles of High-Grade and Low-Grade Gliomas Based on Oligonucleotide Microarray Analysis. *Cancer Res*. 2001 Sep 15;54(15):3988–92.
45. Gutmann DH, Hedrick NM, Li J, Nagarajan R, Perry A, Watson MA. Comparative Gene Expression Profile Analysis of Neurofibromatosis 1-associated and Sporadic Pilocytic Astrocytomas. *Cancer Res*. 2002 Apr 1;54(1):45–7.
46. McLendon R, Friedman A, Bigner D, Van Meir EG, Brat DJ, Mastrogiannis GM, et al. Comprehensive genomic characterization defines human glioblastoma genes and core pathways. *Nature*. 2008 Oct 23;455(7216):1061–8.
47. Shai R, Shi T, Kremen TJ, Horvath S, Liao LM, Cloughesy TF, et al. Gene expression profiling identifies molecular subtypes of gliomas. *Oncogene*. 2003 Jul 31;22(31):4918–23.
48. Sun L, Hui AM, Su Q, Vortmeyer A, Kotliarov Y, Pastorino S, et al. Neuronal and glioma-derived stem cell factor induces angiogenesis within the brain. *Cancer Cell*. 2006 Apr 1;9(4):287–300.
49. Bredel M, Bredel C, Juric D, Harsh GR, Vogel H, Recht LD, et al. Functional network analysis reveals extended gliomagenesis pathway maps and three novel MYC-interacting genes in human gliomas. *Cancer Res*. 2005 Oct 1;65(19):8679–89.
50. Xu S, Sankar S, Neamati N. Protein disulfide isomerase: A promising target for cancer therapy. Vol. 19, *Drug Discovery Today*. Elsevier Ltd; 2014. p. 222–40.
51. Yusenko M V., Kuiper RP, Boethe T, Ljungberg B, van Kessel G, Geurts AG, et al. High-resolution DNA copy number and gene expression analyses distinguish chromophobe renal cell carcinomas and renal oncocytomas. *BMC Cancer*. 2009 May 18;9(1):1–10.
52. Beroukhim R, Brunet JP, Di Napoli A, Mertz KD, Seeley A, Pires MM, et al. Patterns of gene expression and copy-number alterations in von-Hippel Lindau disease-associated and sporadic clear cell carcinoma of the kidney. *Cancer Res*. 2009 Jun 1;69(11):4674–81.

53. Jones J, Otu H, Spentzos D, Kolia S, Inan M, Beecken WD, et al. Gene signatures of progression and metastasis in renal cell cancer. *Clin Cancer Res.* 2005 Aug 15;11(16):5730–9.
54. Bonome T, Levine DA, Shih J, Randonovich M, Pise-Masison CA, Bogomolny F, et al. A gene signature predicting for survival in suboptimally debulked patients with ovarian cancer. *Cancer Res.* 2008 Jul 1;68(13):5478–86.
55. Welsh JB, Zarrinkar PP, Sapinoso LM, Kern SG, Behling CA, Monk BJ, et al. Analysis of gene expression profiles in normal and neoplastic ovarian tissue samples identifies candidate molecular markers of epithelial ovarian cancer. *Proc Natl Acad Sci U S A* [Internet]. 2001 [cited 2020 Apr 29];98(3):1176–81. Available from: www.pnas.org.
56. Welsh JB, Sapinoso LM, Su AI, Kern SG, Wang-Rodriguez J, Moskaluk CA, et al. Analysis of Gene Expression Identifies Candidate Markers and Pharmacological Targets in Prostate Cancer. *Cancer Res.* 2001 Aug 15;61(12):4683–8.
57. Singh D, Febbo PG, Ross K, Jackson DG, Manola J, Ladd C, et al. Gene expression correlates of clinical prostate cancer behavior. *Cancer Cell.* 2002 Mar 1;1(2):203–9.
58. Alaiya AA, Al-Mohanna M, Aslam M, Shinwari Z, Al-Mansouri L, Al-Rodayan M, et al. Proteomics-based signature for human benign prostate hyperplasia and prostate adenocarcinoma. *Int J Oncol.* 2011 Apr 1;38(4):1047–57.
59. Beer DG, Kardia SLR, Huang CC, Giordano TJ, Levin AM, Misek DE, et al. Gene-expression profiles predict survival of patients with lung adenocarcinoma. *Nat Med.* 2002 Jul 15;8(8):816–24.
60. Korkola JE, Houldsworth J, Chadalavada RSV, Olshen AB, Dobrzynski D, Reuter VE, et al. Down-regulation of stem cell genes, including those in a 200-kb gene cluster at 12p13.31, is associated with in vivo differentiation of human male germ cell tumors. *Cancer Res.* 2006 Jan 15;66(2):820–7.
61. Compagno M, Lim WK, Grunn A, Nandula S V., Brahmachary M, Shen Q, et al. Mutations of multiple genes cause deregulation of NF- κ B in diffuse large B-cell lymphoma. *Nature.* 2009 Jun 4;459(7247):717–21.
62. Piccaluga PP, Agostinelli C, Califano A, Rossi M, Basso K, Zupo S, et al. Gene expression analysis of peripheral T cell lymphoma, unspecified, reveals distinct profiles and new potential therapeutic targets. *J Clin Invest.* 2007 Mar 1;117(3):823–34.
63. Basso K, Margolin AA, Stolovitzky G, Klein U, Dalla-Favera R, Califano A. Reverse engineering of regulatory networks in human B cells. *Nat Genet.* 2005 Apr 20;37(4):382–90.

64. Chahed K, Kabbage M, Hamrita B, Guillier CL, Trimeche M, Remadi S, et al. Detection of protein alterations in male breast cancer using two dimensional gel electrophoresis and mass spectrometry: The involvement of several pathways in tumorigenesis. *Clin Chim Acta*. 2008 Feb 1;388(1–2):106–14.
65. Chahed K, Kabbage M, Ehret-Sabatier L, Lemaitre-Guillier C, Remadi S, Hoebeker J, et al. Expression of fibrinogen E-fragment and fibrin E-fragment is inhibited in the human infiltrating ductal carcinoma of the breast: The two-dimensional electrophoresis and MALDI-TOF-mass spectrometry analyses. *Int J Oncol*. 2005 Nov 1;27(5):1425–31.
66. Gromov P, Gromova I, Bunkenborg J, Cabezon T, Moreira JMA, Timmermans-Wielenga V, et al. Up-regulated Proteins in the Fluid Bathing the Tumour Cell Microenvironment as Potential Serological Markers for Early Detection of Cancer of the Breast. *Mol Oncol*. 2010 Feb 1;4(1):65–89.
67. Thongwatchara P, Promwikorn W, Srisomsap C, Chokchaichamnankit D, Boonyaphiphat P, Thongsuksai P. Differential protein expression in primary breast cancer and matched axillary node metastasis. *Oncol Rep*. 2011 Jul 1;26(1):185–91.
68. Goplen D, Wang J, Enger P, Tysnes BB, Terzis AJA, Laerum OD, et al. Protein disulfide isomerase expression is related to the invasive properties of malignant glioma. *Cancer Res*. 2006 Oct 15;66(20):9895–902.
69. Dickerhof N, Kleffmann T, Jack R, McCormick S. Bacitracin inhibits the reductive activity of protein disulfide isomerase by disulfide bond formation with free cysteines in the substrate-binding domain. *FEBS J* [Internet]. 2011 Jun 1 [cited 2020 Apr 29];278(12):2034–43. Available from: <http://doi.wiley.com/10.1111/j.1742-4658.2011.08119.x>
70. González-Santiago L, Alfonso P, Suárez Y, Núñez A, García-Fernández LF, Alvarez E, et al. Proteomic Analysis of the Resistance to Aplidin in Human Cancer Cells. *J Proteome Res*. 2007;6:1286–94.
71. Yu SJ, Yoon JH, Yang JI, Cho EJ, Kwak MS, Jang ES, et al. Enhancement of hexokinase II inhibitor-induced apoptosis in hepatocellular carcinoma cells via augmenting ER stress and anti-angiogenesis by protein disulfide isomerase inhibition. *J Bioenerg Biomembr*. 2012 Feb 15;44(1):101–15.
72. Xu S, Butkevich AN, Yamada R, Zhou Y, Debnath B, Duncan R, et al. Discovery of an orally active small-molecule irreversible inhibitor of protein disulfide isomerase for ovarian cancer treatment. *Proc Natl Acad Sci* [Internet]. 2012 Oct 2 [cited 2020 Apr 29];109(40):16348 LP – 16353. Available from: <http://www.pnas.org/content/109/40/16348.abstract>
73. Hashida T, Kotake Y, Ohta S. Protein disulfide isomerase knockdown-induced cell death is cell-line-dependent and involves apoptosis in MCF-7 cells. *J Toxicol Sci*

[Internet]. 2011 Jan 1 [cited 2020 Apr 29];36(1):1–7. Available from: <http://joi.jlc.jst.go.jp/JST.JSTAGE/jts/36.1?from=CrossRef>

74. Zito E, Chin KT, Blais J, Harding HP, Ron D. ERO1- β , a pancreas-specific disulfide oxidase, promotes insulin biogenesis and glucose homeostasis. *J Cell Biol*. 2010 Mar 22;188(6):821–32.
75. Pagani M, Fabbri M, Benedetti C, Fassio A, Pilati S, Bulleid NJ, et al. Endoplasmic reticulum oxidoreductin 1-L β (ERO1-L β), a human gene induced in the course of the unfolded protein response. *J Biol Chem*. 2000 Aug 4;275(31):23685–92.
76. Dias-Gunasekara S, Gubbens J, Van Lith M, Dunne C, Williams JAG, Katakly R, et al. Tissue-specific expression and dimerization of the endoplasmic reticulum oxidoreductase Ero1 β . *J Biol Chem*. 2005 Sep 23;280(38):33066–75.
77. Zito E. ERO1: A protein disulfide oxidase and H₂O₂ producer. *Free Radic Biol Med*. 2015 Oct 29;83:299–304.
78. Frand AR, Kaiser CA. Ero1p oxidizes protein disulfide isomerase in a pathway for disulfide bond formation in the endoplasmic reticulum. *Mol Cell*. 1999 Oct 1;4(4):469–77.
79. Tu BP, Weissman JS. The FAD- and O₂-dependent reaction cycle of Ero1-mediated oxidative protein folding in the endoplasmic reticulum. *Mol Cell*. 2002 Nov 1;10(5):983–94.
80. Frand AR, Kaiser CA. The ERO1 gene of yeast is required for oxidation of protein dithiols in the endoplasmic reticulum. *Mol Cell*. 1998 Jan 1;1(2):161–70.
81. Kutomi G, Tamura Y, Tanaka T, Kajiwara T, Kukita K, Ohmura T, et al. Human endoplasmic reticulum oxidoreductin 1- α is a novel predictor for poor prognosis of breast cancer. *Cancer Sci* [Internet]. 2013 Aug 1 [cited 2020 May 3];104(8):1091–6. Available from: <http://doi.wiley.com/10.1111/cas.12177>
82. Tanaka T, Kutomi G, Kajiwara T, Kukita K, Kochin V, Kanaseki T, et al. Cancer-associated oxidoreductase ERO1- α promotes immune escape through up-regulation of PD-L1 in human breast cancer. *Oncotarget*. 2017;8(15):24706–18.
83. Yan W, Wang X, Liu T, Chen L, Han L, Xu J, et al. Expression of endoplasmic reticulum oxidoreductase 1- α in cholangiocarcinoma tissues and its effects on the proliferation and migration of cholangiocarcinoma cells. *Cancer Manag Res*. 2019;11:6727–39.
84. Zhang Y, Li T, Zhang L, Shangguan F, Shi G, Wu X, et al. Targeting the functional interplay between endoplasmic reticulum oxidoreductin-1 α and protein disulfide isomerase suppresses the progression of cervical cancer. *EBioMedicine*.

2019 Mar 1;41:408–19.

85. Seol SY, Kim C, Lim JY, Yoon SO, Hong SW, Kim JW, et al. Overexpression of endoplasmic reticulum oxidoreductin 1- α (ERO1L) is associated with poor prognosis of gastric cancer. *Cancer Res Treat*. 2016;48(4):1196–209.
86. Endoh H, Tomida S, Yatabe Y, Konishi H, Osada H, Tajima K, et al. Prognostic Model of Pulmonary Adenocarcinoma by Expression Profiling of Eight Genes As Determined by Quantitative Real-Time Reverse Transcriptase Polymerase Chain Reaction. *J Clin Oncol* [Internet]. 2004 [cited 2020 May 3];22:811–9. Available from: www.jco.org
87. Kim KM, An AR, Park HS, Jang KY, Moon WS, Kang MJ, et al. Combined expression of protein disulfide isomerase and endoplasmic reticulum oxidoreductin 1- α is a poor prognostic marker for non-small cell lung cancer. *Oncol Lett*. 2018 Nov 1;16(5):5753–60.
88. Shergalis AG, Hu S, Bankhead A, Neamati N. Role of the ERO1-PDI interaction in oxidative protein folding and disease. *Pharmacol Ther*. 2020 Mar 20;
89. Yang S, Yang C, Yu F, Ding W, Hu Y, Cheng F, et al. Endoplasmic reticulum resident oxidase ERO1-L α promotes hepatocellular carcinoma metastasis and angiogenesis through the S1PR1/STAT3/VEGF-A pathway. *Cell Death Dis*. 2018;9(1105).
90. Hayes KE, Batsomboon P, Chen WC, Johnson BD, Becker A, Eschrich S, et al. Inhibition of the FAD containing ER oxidoreductin 1 (Ero1) protein by EN-460 as a strategy for treatment of multiple myeloma. *Bioorganic Med Chem*. 2019 Apr 15;27(8):1479–88.
91. Kukita K, Tamura Y, Tanaka T, Kajiwara T, Kutomi G, Saito K, et al. Cancer-Associated Oxidase ERO1- α Regulates the Expression of MHC Class I Molecule via Oxidative Folding. *J Immunol*. 2015 Dec 1;194:4988–96.
92. Takei N, Yoneda A, Sakai-Sawada K, Kosaka M, Minomi K, Tamura Y. Hypoxia-inducible ERO1 α promotes cancer progression through modulation of integrin- β 1 modification and signalling in HCT116 colorectal cancer cells. *Sci Rep*. 2017 Dec 1;7(1):1–11.
93. Blais JD, Chin K-T, Zito E, Zhang Y, Heldman N, Harding HP, et al. A Small Molecule Inhibitor of Endoplasmic Reticulum Oxidation 1 (ERO1) with Selectively Reversible Thiol Reactivity. *J Biol Chem* [Internet]. 2010 Jul 2 [cited 2020 May 3];285(27):20993–1003. Available from: <http://www.jbc.org/cgi/content/short/285/27/20993>
94. Hagiya M, Francavilla A, Polimeno L, Ihara I, Sakai H, Seki T, et al. Cloning and sequence analysis of the rat augments of liver regeneration (ALR) gene:

- Expression of biologically active recombinant ALR and demonstration of tissue distribution. *Proc Natl Acad Sci U S A*. 1994 Aug 16;91(17):8142–6.
95. Lorenzo P, Barbara P, Floriana G, Biagio M, Leonardo R, Roberta R, et al. Expression and localization of augmenter of liver regeneration in human muscle tissue. *Int J Exp Pathol*. 2009 Aug;90(4):423–30.
 96. Yu HY, Zhu MH, Xiang DR, Li J, Sheng JF. High expression of 23 kDa protein of augmenter of liver regeneration (ALR) in human hepatocellular carcinoma. *Oncotargets Ther*. 2014 Jun 2;7:887–93.
 97. Lisowsky T, Lee JE, Polimeno L, Francavilla A, Hofhaus G. Mammalian augmenter of liver regeneration protein is a sulfhydryl oxidase. *Dig Liver Dis*. 2001 Mar 1;33(2):173–80.
 98. Farrell SR, Thorpe C. Augmenter of liver regeneration: A flavin-dependent sulfhydryl oxidase with cytochrome c reductase activity. *Biochemistry*. 2005 Feb 8;44(5):1532–41.
 99. Banci L, Bertini I, Calderone V, Cefaro C, Ciofi-Baffoni S, Gallo A, et al. Molecular recognition and substrate mimicry drive the electron-transfer process between MIA40 and ALR. *Proc Natl Acad Sci U S A*. 2011 Mar 22;108(12):4811–6.
 100. Uhlén M, Björling E, Agaton C, Szgyarto CA-K, Amini B, Andersen E, et al. A Human Protein Atlas for Normal and Cancer Tissues Based on Antibody Proteomics. *Mol Cell Proteomics* [Internet]. 2005 Dec 1;4(12):1920 LP – 1932. Available from: <http://www.mcponline.org/content/4/12/1920.abstract>
 101. Pontén F, Jirstrom K, Uhlen M. The Human Protein Atlas—a tool for pathology. *J Pathol* [Internet]. 2008 Dec 1;216(4):387–93. Available from: <https://doi.org/10.1002/path.2440>
 102. The Human Protein Atlas [Internet]. [cited 2020 Apr 22]. Available from: <https://www.proteinatlas.org/ENSG00000127554-GFER/pathology>
 103. Dayoub R, Wagner H, Bataille F, Stöltzing O, Spruss T, Buechler C, et al. Liver regeneration associated protein (ALR) exhibits antimetastatic potential in hepatocellular carcinoma. *Mol Med*. 2011 Mar 8;17(3–4):221–8.
 104. Cao Y, Fu YL, Yu M, Yue P bin, Ge CH, Xu WX, et al. Human augmenter of liver regeneration is important for hepatoma cell viability and resistance to radiation-induced oxidative stress. *Free Radic Biol Med*. 2009 Oct 1;47(7):1057–66.
 105. Thasler WE, Schlott T, Thelen P, Hellerbrand C, Bataille F, Lichtenauer M, et al. Expression of augmenter of liver regeneration (ALR) in human liver cirrhosis and carcinoma. *Histopathology*. 2005;47:57–66.

106. Polimeno L, Pesetti B, De Santis F, Resta L, Rossi R, De Palma A, et al. Decreased expression of the Augmenter of Liver Regeneration results in increased apoptosis and oxidative damage in human-derived glioma cells. *Cell Death Dis.* 2012 Apr 5;3(4):e289–e289.
107. Lorenzo P, Barbara P, Thomas L, Florenzo I, Leonardo R, Floriana G, et al. Protective effect of augmenter of liver regeneration on hydrogen peroxide-induced apoptosis in SH-SY5Y human neuroblastoma cells. *Free Radic Res* [Internet]. 2009 Jan [cited 2020 Apr 22];43(9):865–75. Available from: <http://www.tandfonline.com/doi/full/10.1080/10715760903100125>
108. Guo YY, Wu Y, Jia XW, An W. Augmenter of liver regeneration potentiates doxorubicin anticancer efficacy by reducing the expression of ABCB1 and ABCG2 in hepatocellular carcinoma. *Lab Investig.* 2017 Dec 1;97(12):1400–11.
109. Shen Y, Liu Q, Lou S, Luo Y, Sun H, Zeng H, et al. Decreased expression of the augmenter of liver regeneration results in growth inhibition and increased chemosensitivity of acute T lymphoblastic leukemia cells. *Oncol Rep.* 2017 Nov 1;38(5):3130–6.
110. Tang L, Sun H, Zhang L, Deng JC, Guo H, Zhang L, et al. Effects of the augmenter of liver regeneration on the biological behavior of hepatocellular carcinoma. *Saudi Med J.* 2009 Aug 1;30(8):1001–9.
111. Sun L, Liang C, Shirazian S, Zhou Y, Miller T, Cui J, et al. Discovery of 5-[5-Fluoro-2-oxo-1,2-dihydroindol-(3Z)-ylidenemethyl]-2,4-dimethyl-1H-pyrrole-3-carboxylic Acid (2-Diethylaminoethyl)amide, a Novel Tyrosine Kinase Inhibitor Targeting Vascular Endothelial and Platelet-Derived Growth Factor Receptor Tyrosi. *J Med Chem* [Internet]. 2003 Mar 1;46(7):1116–9. Available from: <https://doi.org/10.1021/jm0204183>
112. Chopra S, De Mattos SF, Lam EWF, Mann DJ. Jab1 co-activation of c-Jun is abrogated by the serine 10-phosphorylated form of p27 Kip1. *J Biol Chem.* 2002 Sep 6;277(36):32413–6.
113. Garces de Los Fayos Alonso I, Liang HC, Turner SD, Lagger S, Merkel O, Kenner L. The role of activator protein-1 (AP-1) family members in CD30-positive lymphomas. *Cancers (Basel).* 2018 Apr 1;10(4).
114. Li Y, Li M, Xing G, Hu Z, Wang Q, Dong C, et al. Stimulation of the mitogen-activated protein kinase cascade tyrosine phosphorylation of the epidermal growth factor receptor by hepatopoietin. *J Biol Chem.* 2000 Dec 1;275(48):37443–7.
115. Wang G, Yang XM, Zhang Y, Wang QM, Chen H, Wei H, et al. Identification and characterization of receptor for mammalian hepatopoietin that is homologous to yeast ERV1. *J Biol Chem.* 1999 Apr 23;274(17):11469–72.

116. LaBrecque DR, Pesch LA. Preparation and partial characterization of hepatic regenerative stimulator substance (SS) from rat liver. *J Physiol*. 1975 Jun 1;248(2):273–84.
117. Gatzidou E, Kouraklis G, Theocharis S. Insights on augments of liver regeneration cloning and function. Vol. 12, *World Journal of Gastroenterology*. WJG Press; 2006. p. 4951–8.
118. Daithankar VN, Farrell SR, Thorpe C. Augmenter of liver regeneration: Substrate specificity of a flavin-dependent oxidoreductase from the mitochondrial intermembrane space. *Biochemistry*. 2009 Jun 9;48(22):4828–37.
119. Sankar U, Means AR. Gfer is a critical regulator of HSC proliferation. Vol. 10, *Cell Cycle*. Taylor and Francis Inc.; 2011. p. 2263–8.
120. Todd LR, Damin MN, Gomathinayagam R, Horn SR, Means AR, Sankar U. Growth Factor ero1-like Modulates Drp1 to Preserve Mitochondrial Dynamics and Function in Mouse Embryonic Stem Cells. *Mol Biol Cell*. 2010 Apr 1;21(7):1225–36.
121. Coppock DL, Kopman C, Scandalis S, Gilleran S. Preferential gene expression in quiescent human lung fibroblasts. *Cell Growth Differ* [Internet]. 1993 Jun 1;4(6):483–93. Available from: <http://cgd.aacrjournals.org/cgi/content/abstract/4/6/483>
122. Coppock DL, Cina-Poppe D, Gilleran S. The Quiescin Q6 gene (QSCN6) is a fusion of two ancient gene families: Thioredoxin and ERV1. *Genomics*. 1998 Dec 15;54(3):460–8.
123. Lake DF, Faigel DO. The emerging role of QSOX1 in cancer. *Antioxid Redox Signal* [Internet]. 2014 Jul 20;21(3):485–96. Available from: <https://www.ncbi.nlm.nih.gov/pubmed/24359107>
124. Zheng W, Chu Y, Yin Q, Xu L, Yang C, Zhang W, et al. Crucial effect of the first CXXC motif of human QSOX 1b on the activity to different substrates. *J Biochem* [Internet]. 2010 Dec 9;149(3):293–300. Available from: <https://doi.org/10.1093/jb/mvq143>
125. Chakravarthi S, Jessop CE, Willer M, Stirling CJ, Bulleid NJ. Intracellular catalysis of disulfide bond formation by the human sulfhydryl oxidase, QSOX1. *Biochem J*. 2007 Jun 15;404(3):403–11.
126. Rudolf J, Pringle MA, Bulleid NJ. Proteolytic processing of QSOX1A ensures efficient secretion of a potent disulfide catalyst. *Biochem J*. 2013 Sep 1;454(2):181–90.
127. Thorpe C, Hooper KL, Raje S, Glynn NM, Burnside J, Turi GK, et al. Sulfhydryl

- oxidases: Emerging catalysts of protein disulfide bond formation in eukaryotes. *Arch Biochem Biophys* [Internet]. 2002 Sep 1 [cited 2020 Apr 21];405(1):1–12. Available from: <https://www.sciencedirect.com/science/article/abs/pii/S0003986102003375?via%3Dihub>
128. Kodali VK, Thorpe C. Quiescin sulfhydryl oxidase from *trypanosoma brucei*: Catalytic activity and mechanism of a QSOX family member with a single thioredoxin domain. *Biochemistry*. 2010 Mar 9;49(9):2075–85.
129. Heckler EJ, Alon A, Fass D, Thorpe C. Human quiescin-sulfhydryl oxidase, QSOX1: probing internal redox steps by mutagenesis. *Biochemistry* [Internet]. 2008/04/05. 2008 Apr 29;47(17):4955–63. Available from: <https://www.ncbi.nlm.nih.gov/pubmed/18393449>
130. Israel BA, Kodali VK, Thorpe C. Going through the Barrier: Coupled disulfide exchange reactions promote efficient catalysis in quiescin sulfhydryl oxidase. *J Biol Chem*. 2014 Feb 21;289(8):5274–84.
131. Raje S, Glynn NM, Thorpe C. A continuous fluorescence assay for sulfhydryl oxidase. *Anal Biochem* [Internet]. 2002;307(2):266–72. Available from: <http://www.sciencedirect.com/science/article/pii/S0003269702000507>
132. Raje S, Thorpe C. Inter-Domain Redox Communication in Flavoenzymes of the Quiescin/Sulfhydryl Oxidase Family: Role of a Thioredoxin Domain in Disulfide Bond Formation,. *Biochemistry* [Internet]. 2003 Apr 1;42(15):4560–8. Available from: <https://doi.org/10.1021/bi030003z>
133. Rancy PC, Thorpe C. Oxidative protein folding in vitro: a study of the cooperation between quiescin-sulfhydryl oxidase and protein disulfide isomerase. *Biochemistry* [Internet]. 2008/10/21. 2008 Nov 18;47(46):12047–56. Available from: <https://pubmed.ncbi.nlm.nih.gov/18937500>
134. Zheng W, Zhang W, Hu W, Zhang C, Yang Y. Exploring the smallest active fragment of HsQSOX1b and finding a highly efficient oxidative engine. *PLoS One* [Internet]. 2012/07/20. 2012;7(7):e40935–e40935. Available from: <https://pubmed.ncbi.nlm.nih.gov/22911720>
135. Alon A, Heckler EJ, Thorpe C, Fass D. QSOX contains a pseudo-dimer of functional and degenerate sulfhydryl oxidase domains. *FEBS Lett* [Internet]. 2010 Apr 16;584(8):1521–5. Available from: <https://doi.org/10.1016/j.febslet.2010.03.001>
136. Alon A, Grossman I, Gat Y, Kodali VK, DiMaio F, Mehlman T, et al. The dynamic disulphide relay of quiescin sulphhydryl oxidase. *Nature* [Internet]. 2012 [cited 2019 Feb 24];488:414–8. Available from: <https://www.rcsb.org/structure/3Q6O>

137. Gat Y, Vardi-Kilshtain A, Grossman I, Major DT, Fass D. Enzyme structure captures four cysteines aligned for disulfide relay. *Protein Sci* [Internet]. 2014/06/18. 2014 Aug;23(8):1102–12. Available from: <https://pubmed.ncbi.nlm.nih.gov/24888638>
138. Grossman I, Alon A, Ilani T, Fass D. An Inhibitory Antibody Blocks the First Step in the Dithiol/Disulfide Relay Mechanism of the Enzyme QSOX1. *J Mol Biol* [Internet]. 2013;425(22):4366–78. Available from: <http://www.sciencedirect.com/science/article/pii/S0022283613004439>
139. Hanavan PD, Borges CR, Katchman BA, Faigel DO, Ho TH, Ma C-T, et al. Ebselen inhibits QSOX1 enzymatic activity and suppresses invasion of pancreatic and renal cancer cell lines. *Oncotarget* [Internet]. 2015 Jun 1;6(21):18418–28. Available from: <https://www.ncbi.nlm.nih.gov/pubmed/26158899>
140. Antwi K, Hostetter G, Demeure MJ, Katchman BA, Decker GA, Ruiz Y, et al. Analysis of the Plasma Peptidome from Pancreas Cancer Patients Connects a Peptide in Plasma to Overexpression of the Parent Protein in Tumors. *J Proteome Res* [Internet]. 2009 Oct 2 [cited 2020 May 8];8(10):4722–31. Available from: <https://doi.org/10.1021/pr900414f>
141. Morel C, Adami P, Musard JF, Duval D, Radom J, Jouvenot M. Involvement of sulfhydryl oxidase QSOX1 in the protection of cells against oxidative stress-induced apoptosis. *Exp Cell Res*. 2007 Nov 15;313(19):3971–82.
142. Song H, Zhang B, Watson MA, Humphrey PA, Lim H, Milbrandt J. Loss of Nkx3.1 leads to the activation of discrete downstream target genes during prostate tumorigenesis. *Oncogene* [Internet]. 2009/07/13. 2009 Sep 17;28(37):3307–19. Available from: <https://www.ncbi.nlm.nih.gov/pubmed/19597465>
143. Ouyang X, DeWeese TL, Nelson WG, Abate-Shen C. Loss-of-function of Nkx3.1 promotes increased oxidative damage in prostate carcinogenesis. *Cancer Res*. 2005 Aug 1;65(15):6773–9.
144. Shi C-Y, Fan Y, Liu B, Lou W-H. HIF1 Contributes to Hypoxia-Induced Pancreatic Cancer Cells Invasion via Promoting QSOX1 Expression. *Cell Physiol Biochem* [Internet]. 2013 [cited 2020 May 8];32(3):561–8. Available from: <https://www.karger.com/Article/FullText/354460>
145. Ilani T, Alon A, Grossman I, Horowitz B, Kartvelishvily E, Cohen SR, et al. A Secreted Disulfide Catalyst Controls Extracellular Matrix Composition and Function. *Science* (80-) [Internet]. 2013 Jul 5;341(6141):74 LP – 76. Available from: <http://science.sciencemag.org/content/341/6141/74.abstract>
146. Katchman BA, Antwi K, Hostetter G, Demeure MJ, Watanabe A, Decker GA, et al. Quiescin Sulfhydryl Oxidase 1 Promotes Invasion of Pancreatic Tumor Cells Mediated by Matrix Metalloproteinases. *Mol Cancer Res* [Internet]. 2011 Dec

1;9(12):1621 LP – 1631. Available from:
<http://mcr.aacrjournals.org/content/9/12/1621.abstract>

147. Javitt G, Grossman-Haham I, Alon A, Resnick E, Mutsafi Y, Ilani T, et al. cis-Proline mutants of quiescin sulfhydryl oxidase 1 with altered redox properties undermine extracellular matrix integrity and cell adhesion in fibroblast cultures. *Protein Sci* [Internet]. 2018/12/17. 2019 Jan;28(1):228–38. Available from: <https://www.ncbi.nlm.nih.gov/pubmed/30367560>
148. Feldman T, Grossman-Haham I, Elkis Y, Vilela P, Moskovits N, Barshack I, et al. Inhibition of fibroblast secreted QSOX1 perturbs extracellular matrix in the tumor microenvironment and decreases tumor growth and metastasis in murine cancer models. *Oncotarget* [Internet]. 2020 Jan 28 [cited 2020 May 5];11(4):386–98. Available from: <http://www.oncotarget.com/index.php?journal=oncotarget&>
149. Geng Y, Xu C, Wang Y, Zhang L. Quiescin Sulfhydryl Oxidase 1 Regulates the Proliferation, Migration and Invasion of Human Glioblastoma Cells via PI3K/Akt Pathway. *Onco Targets Ther* [Internet]. 2020 Jun 17;13:5721–9. Available from: <https://pubmed.ncbi.nlm.nih.gov/32606784>
150. Knutsvik G, Collett K, Arnes J, Akslen LA, Stefansson IM. QSOX1 expression is associated with aggressive tumor features and reduced survival in breast carcinomas. *Mod Pathol* [Internet]. 2016 Aug 26 [cited 2020 May 8];29(12):1485. Available from: <https://doi.org/10.1038/modpathol.2016.148>
151. Katchman BA, Ocal IT, Cunliffe HE, Chang Y-H, Hostetter G, Watanabe A, et al. Expression of quiescin sulfhydryl oxidase 1 is associated with a highly invasive phenotype and correlates with a poor prognosis in Luminal B breast cancer. *Breast Cancer Res* [Internet]. 2013 Mar 28;15(2):R28–R28. Available from: <https://www.ncbi.nlm.nih.gov/pubmed/23536962>
152. Soloviev M, Esteves MP, Amiri F, Crompton MR, Rider CC. Elevated Transcription of the Gene QSOX1 Encoding Quiescin Q6 Sulfhydryl Oxidase 1 in Breast Cancer. *PLoS One* [Internet]. 2013 Feb 27;8(2):e57327. Available from: <https://doi.org/10.1371/journal.pone.0057327>
153. Sung H-J, Ahn J-M, Yoon Y-H, Na S-S, Choi Y-J, Kim Y-I, et al. Quiescin Sulfhydryl Oxidase 1 (QSOX1) Secreted by Lung Cancer Cells Promotes Cancer Metastasis. *Int J Mol Sci* [Internet]. 2018 Oct 17;19(10):3213. Available from: <https://www.ncbi.nlm.nih.gov/pubmed/30336636>
154. Zhou L, Chen H-M, Qu S, Li L, Zhao W, Liang Z-G, et al. Reduced QSOX1 enhances radioresistance in nasopharyngeal carcinoma. *Oncotarget* [Internet]. 2017 Dec 14;9(3):3230–41. Available from: <https://www.ncbi.nlm.nih.gov/pubmed/29423042>
155. Guo J, Jing R, Zhong J-H, Dong X, Li Y-X, Liu Y-K, et al. Identification of CD14

- as a potential biomarker of hepatocellular carcinoma using iTRAQ quantitative proteomics. *Oncotarget* [Internet]. 2017 Jun 28;8(37):62011–28. Available from: <https://www.ncbi.nlm.nih.gov/pubmed/28977922>
156. Do WL, Conneely K, Gabram-Mendola S, Krishnamurti U, D'Angelo O, Miller-Kleinhenz J, et al. Obesity-associated methylation in breast tumors: a possible link to disparate outcomes? *Breast Cancer Res Treat*. 2020 May 1;181(1):135–44.
 157. Pernodet N, Hermetet F, Adami P, Vejux A, Descotes F, Borg C, et al. High expression of QSOX1 reduces tumorigenesis, and is associated with a better outcome for breast cancer patients. *Breast Cancer Res* [Internet]. 2012 Oct 25 [cited 2020 May 5];14(5):R136. Available from: <http://breast-cancer-research.biomedcentral.com/articles/10.1186/bcr3341>
 158. Poillet L, Pernodet N, Boyer-Guittaut M, Adami P, Borg C, Jouvenot M, et al. QSOX1 inhibits autophagic flux in breast cancer cells. *PLoS One*. 2014 Jan 24;9(1).
 159. Zhang X-F, Wang J, Jia H-L, Zhu W-W, Lu L, Ye Q-H, et al. Core fucosylated glycan-dependent inhibitory effect of QSOX1-S on invasion and metastasis of hepatocellular carcinoma. *Cell death Discov* [Internet]. 2019 Apr 3 [cited 2020 May 5];5(1):84. Available from: <http://www.nature.com/articles/s41420-019-0164-8>
 160. Radom J, Colin D, Thiebault F, Dognin-Bergeret M, Mairet-Coello G, Esnard-Feve A, et al. Identification and expression of a new splicing variant of FAD-sulfhydryl oxidase in adult rat brain. *Biochim Biophys Acta - Gene Struct Expr*. 2006 May 1;1759(5):225–33.
 161. Sapra A, Ramadan D, Thorpe C. Multivalency in the inhibition of oxidative protein folding by arsenic(III) species. *Biochemistry*. 2015 Jan 20;54(2):612–21.
 162. Schueler J, Klingner K, Bug D, Zoeller C, Maier A, Dong M, et al. Patient derived renal cell carcinoma xenografts exhibit distinct sensitivity patterns in response to antiangiogenic therapy and constitute a suitable tool for biomarker development. *Oncotarget* [Internet]. 2018 Jul 24;9(57):30946–61. Available from: <https://www.ncbi.nlm.nih.gov/pubmed/30123419>
 163. Mohamadi F, Richards NGJ, Guida WC, Liskamp R, Lipton M, Caufield C, et al. Macromodel—an integrated software system for modeling organic and bioorganic molecules using molecular mechanics. *J Comput Chem* [Internet]. 1990 May 1;11(4):440–67. Available from: <https://doi.org/10.1002/jcc.540110405>
 164. Caulfield T, Devkota B. Motion of transfer RNA from the A/T state into the A-site using docking and simulations. *Proteins Struct Funct Bioinforma* [Internet]. 2012 Nov 1;80(11):2489–500. Available from: <https://doi.org/10.1002/prot.24131>

165. Caulfield TR, Devkota B, Rollins GC. Examinations of tRNA Range of Motion Using Simulations of Cryo-EM Microscopy and X-Ray Data. *J Biophys* [Internet]. 2011/03/28. 2011;2011:219515. Available from: <https://www.ncbi.nlm.nih.gov/pubmed/21716650>
166. Caulfield TR, Fiesel FC, Moussaud-Lamodière EL, Dourado DFAR, Flores SC, Springer W. Phosphorylation by PINK1 releases the UBL domain and initializes the conformational opening of the E3 ubiquitin ligase Parkin. *PLoS Comput Biol* [Internet]. 2014 Nov 6;10(11):e1003935–e1003935. Available from: <https://www.ncbi.nlm.nih.gov/pubmed/25375667>
167. Caulfield TR, Fiesel FC, Springer W. Activation of the E3 ubiquitin ligase Parkin. *Biochem Soc Trans* [Internet]. 2015 Apr;43(2):269–74. Available from: <https://www.ncbi.nlm.nih.gov/pubmed/25849928>
168. Puschmann A, Fiesel FC, Caulfield TR, Hudec R, Ando M, Truban D, et al. Heterozygous PINK1 p.G411S increases risk of Parkinson's disease via a dominant-negative mechanism. *Brain* [Internet]. 2016/11/02. 2017 Jan;140(1):98–117. Available from: <https://www.ncbi.nlm.nih.gov/pubmed/27807026>
169. Vivoli M, Caulfield TR, Martínez-Mayorga K, Johnson AT, Jiao G-S, Lindberg I. Inhibition of prohormone convertases PC1/3 and PC2 by 2,5-dideoxystreptamine derivatives. *Mol Pharmacol* [Internet]. 2012 Mar;81(3):440–54. Available from: <https://www.ncbi.nlm.nih.gov/pubmed/22169851>
170. Caulfield T, Medina-Franco JL. Molecular dynamics simulations of human DNA methyltransferase 3B with selective inhibitor nanaomycin A. *J Struct Biol* [Internet]. 2011;176(2):185–91. Available from: <http://www.sciencedirect.com/science/article/pii/S1047847711002243>
171. Jorgensen WL, Tirado-Rives J. The OPLS [optimized potentials for liquid simulations] potential functions for proteins, energy minimizations for crystals of cyclic peptides and crambin. *J Am Chem Soc* [Internet]. 1988 Mar 1;110(6):1657–66. Available from: <https://doi.org/10.1021/ja00214a001>
172. Loving K, Salam NK, Sherman W. Energetic analysis of fragment docking and application to structure-based pharmacophore hypothesis generation. *J Comput Aided Mol Des* [Internet]. 2009;23(8):541–54. Available from: <https://doi.org/10.1007/s10822-009-9268-1>
173. Friesner RA, Murphy RB, Repasky MP, Frye LL, Greenwood JR, Halgren TA, et al. Extra Precision Glide: Docking and Scoring Incorporating a Model of Hydrophobic Enclosure for Protein–Ligand Complexes. *J Med Chem* [Internet]. 2006 Oct 1;49(21):6177–96. Available from: <https://doi.org/10.1021/jm051256o>
174. Salam NK, Nuti R, Sherman W. Novel Method for Generating Structure-Based Pharmacophores Using Energetic Analysis. *J Chem Inf Model* [Internet]. 2009 Oct

- 26;49(10):2356–68. Available from: <https://doi.org/10.1021/ci900212v>
175. Vinci M, Box C, Eccles SA. Three-dimensional (3D) tumor spheroid invasion assay. *J Vis Exp* [Internet]. 2015 May 1;(99):e52686–e52686. Available from: <https://www.ncbi.nlm.nih.gov/pubmed/25993495>
 176. Schindelin J, Arganda-Carreras I, Frise E, Kaynig V, Longair M, Pietzsch T, et al. Fiji: an open-source platform for biological-image analysis. *Nat Methods* [Internet]. 2012 Jun 28;9(7):676–82. Available from: <https://www.ncbi.nlm.nih.gov/pubmed/22743772>
 177. Jalencas X, Mestres J. On the origins of drug polypharmacology. *Medchemcomm* [Internet]. 2013;4(1):80–7. Available from: <http://dx.doi.org/10.1039/C2MD20242E>
 178. Mustafa HN, El Awdan SA, Hegazy GA, Abdel Jaleel GA. Prophylactic role of coenzyme Q10 and *Cynara scolymus* L on doxorubicin-induced toxicity in rats: Biochemical and immunohistochemical study. *Indian J Pharmacol* [Internet]. 2015;47(6):649–56. Available from: <https://www.ncbi.nlm.nih.gov/pubmed/26729958>
 179. Baek JA, Song PH, Ko Y, Gu MJ. High expression of QSOX1 is associated with tumor invasiveness and high grades groups in prostate cancer. *Pathol - Res Pract* [Internet]. 2018;214(7):964–7. Available from: <http://www.sciencedirect.com/science/article/pii/S0344033818304369>
 180. Oraiopoulou M-E, Tzamali E, Tzedakis G, Liapis E, Zacharakis G, Vakis A, et al. Integrating in vitro experiments with in silico approaches for Glioblastoma invasion: the role of cell-to-cell adhesion heterogeneity. *Sci Rep* [Internet]. 2018;8(1):16200. Available from: <https://doi.org/10.1038/s41598-018-34521-5>
 181. Sharma I, Singh A, Siraj F, Saxena S. IL-8/CXCR1/2 signalling promotes tumor cell proliferation, invasion and vascular mimicry in glioblastoma. *J Biomed Sci* [Internet]. 2018 Aug 8;25(1):62. Available from: <https://www.ncbi.nlm.nih.gov/pubmed/30086759>
 182. Lang L, Shay C, Xiong Y, Thakkar P, Chemmalakuzhy R, Wang X, et al. Combating head and neck cancer metastases by targeting Src using multifunctional nanoparticle-based saracatinib. *J Hematol Oncol* [Internet]. 2018;11(1):85. Available from: <https://doi.org/10.1186/s13045-018-0623-3>
 183. Ho TH, Serie DJ, Parasramka M, Cheville JC, Bot BM, Tan W, et al. Differential gene expression profiling of matched primary renal cell carcinoma and metastases reveals upregulation of extracellular matrix genes. *Ann Oncol Off J Eur Soc Med Oncol* [Internet]. 2016/12/19. 2017 Mar;28(3):604–10. Available from: <https://www.ncbi.nlm.nih.gov/pubmed/27993815>

184. Mahesh S, Tang KC, Raj M. Amide bond activation of biological molecules. *Molecules*. 2018 Oct 12;23(10).
185. Hohenester E, Yurchenco PD. Laminins in basement membrane assembly. *Cell Adh Migr* [Internet]. 2012/10/17. 2013;7(1):56–63. Available from: <https://pubmed.ncbi.nlm.nih.gov/23076216>
186. Hamill KJ, Kligys K, Hopkinson SB, Jones JCR. Laminin deposition in the extracellular matrix: a complex picture emerges. *J Cell Sci* [Internet]. 2009 Dec 15;122(24):4409 LP – 4417. Available from: <http://jcs.biologists.org/content/122/24/4409.abstract>
187. Gorter A, Zijlmans HJ, van Gent H, Trimbos JB, Fleuren GJ, Jordanova ES. Versican expression is associated with tumor-infiltrating CD8-positive T cells and infiltration depth in cervical cancer. *Mod Pathol* [Internet]. 2010;23(12):1605–15. Available from: <https://doi.org/10.1038/modpathol.2010.154>
188. Mitsui Y, Shiina H, Kato T, Maekawa S, Hashimoto Y, Shiina M, et al. Versican Promotes Tumor Progression, Metastasis and Predicts Poor Prognosis in Renal Carcinoma. *Mol Cancer Res* [Internet]. 2017/02/27. 2017 Jul;15(7):884–95. Available from: <https://pubmed.ncbi.nlm.nih.gov/28242813>
189. Yao Y, Dai W. Genomic Instability and Cancer. *J Carcinog Mutagen* [Internet]. 2014;5:1000165. Available from: <https://pubmed.ncbi.nlm.nih.gov/25541596>
190. Singh A, Greninger P, Rhodes D, Koopman L, Violette S, Bardeesy N, et al. A Gene Expression Signature Associated with “K-Ras Addiction” Reveals Regulators of EMT and Tumor Cell Survival. *Cancer Cell* [Internet]. 2009;15(6):489–500. Available from: <http://www.sciencedirect.com/science/article/pii/S1535610809001111>
191. Torti D, Trusolino L. Oncogene addiction as a foundational rationale for targeted anti-cancer therapy: promises and perils. *EMBO Mol Med* [Internet]. 2011/09/23. 2011 Nov;3(11):623–36. Available from: <https://pubmed.ncbi.nlm.nih.gov/21953712>
192. Xu D, Jalal SI, Sledge GW, Meroueh SO. Small-molecule binding sites to explore protein-protein interactions in the cancer proteome. *Mol Biosyst* [Internet]. 2016/07/25. 2016 Oct 20;12(10):3067–87. Available from: <https://pubmed.ncbi.nlm.nih.gov/27452673>
193. Caillard A, Sadoune M, Cescau A, Meddour M, Gandon M, Polidano E, et al. QSOX1, a novel actor of cardiac protection upon acute stress in mice. *J Mol Cell Cardiol* [Internet]. 2018;119:75–86. Available from: <http://www.sciencedirect.com/science/article/pii/S0022282818301445>
194. Chen Y-J, Spence HJ, Cameron JM, Jess T, Ilsley JL, Winder SJ. Direct

- interaction of beta-dystroglycan with F-actin. *Biochem J* [Internet]. 2003 Oct 15;375(Pt 2):329–37. Available from: <https://pubmed.ncbi.nlm.nih.gov/12892561>
195. Sit S-T, Manser E. Rho GTPases and their role in organizing the actin cytoskeleton. *J Cell Sci* [Internet]. 2011 Mar 1;124(5):679 LP – 683. Available from: <http://jcs.biologists.org/content/124/5/679.abstract>
 196. Chen L, Yang S, Jakoncic J, Zhang JJ, Huang X-Y. Migrastatin analogues target fascin to block tumour metastasis. *Nature* [Internet]. 2010 Apr 15;464(7291):1062–6. Available from: <https://pubmed.ncbi.nlm.nih.gov/20393565>
 197. Huang F-K, Han S, Xing B, Huang J, Liu B, Bordeleau F, et al. Targeted inhibition of fascin function blocks tumour invasion and metastatic colonization. *Nat Commun* [Internet]. 2015;6(1):7465. Available from: <https://doi.org/10.1038/ncomms8465>
 198. Van Impe K, Bethuyne J, Cool S, Impens F, Ruano-Gallego D, De Wever O, et al. A nanobody targeting the F-actin capping protein CapG restrains breast cancer metastasis. *Breast Cancer Res* [Internet]. 2013;15(6):R116. Available from: <https://doi.org/10.1186/bcr3585>
 199. Zhou J, Yu G, Huang F. Supramolecular chemotherapy based on host–guest molecular recognition: a novel strategy in the battle against cancer with a bright future. *Chem Soc Rev* [Internet]. 2017;46(22):7021–53. Available from: <http://dx.doi.org/10.1039/C6CS00898D>
 200. Peters C, Brown S. Antibody-drug conjugates as novel anti-cancer chemotherapeutics. *Biosci Rep* [Internet]. 2015 Jun 12;35(4):e00225. Available from: <https://pubmed.ncbi.nlm.nih.gov/26182432>
 201. Frei EJ, Eder J. *Combination Chemotherapy* [Internet]. Holland-Fr. Kufe D, Pollock R, Weichselbaum R, editors. Hamilton (ON): BC Decker; 2003. Available from: <https://www.ncbi.nlm.nih.gov/books/NBK13955/>
 202. Sani M, Volonterio A, Zanda M. The Trifluoroethylamine Function as Peptide Bond Replacement. *ChemMedChem* [Internet]. 2007 Dec 10;2(12):1693–700. Available from: <https://doi.org/10.1002/cmdc.200700156>
 203. Yurchenco PD, Quan Y, Colognato H, Mathus T, Harrison D, Yamada Y, et al. The α chain of laminin-1 is independently secreted and drives secretion of its β - and γ -chain partners. *Proc Natl Acad Sci U S A* [Internet]. 1997 Sep 16 [cited 2020 Sep 19];94(19):10189–94. Available from: <https://pubmed.ncbi.nlm.nih.gov/9294185/>
 204. Nomizu M, Utani A, Beck K, Otaka A, Roller PP, Yamada Y. Mechanism of laminin chain assembly into a triple-stranded coiled-coil structure. *Biochemistry* [Internet]. 1996 Mar 5 [cited 2020 Sep 19];35(9):2885–93. Available from:

<https://pubmed.ncbi.nlm.nih.gov/8608125/>

205. Hamill KJ, Kligys K, Hopkinson SB, Jones JCRR. Laminin deposition in the extracellular matrix: a complex picture emerges. *J Cell Sci* [Internet]. 2009 Dec 15 [cited 2020 Sep 19];122(24):4409 LP – 4417. Available from: [/pmc/articles/PMC2787456/?report=abstract](https://pubmed.ncbi.nlm.nih.gov/8608125/)
206. Hanavan P. Small Molecule Inhibition of Quiescin Sulfhydryl Oxidase 1 (QSOX1), a Dynamic ProTumorigenic Regulator of the Extracellular Matrix. Arizona State University; 2015.
207. Yu X, Petritis B, Duan H, Xu D, LaBaer J. Advances in cell-free protein array methods. *Expert Rev Proteomics* [Internet]. 2018 Jan 2;15(1):1–11. Available from: <https://doi.org/10.1080/14789450.2018.1415146>
208. Ramachandran N, Raphael J V, Hainsworth E, Demirkan G, Fuentes MG, Rolfs A, et al. Next-generation high-density self-assembling functional protein arrays. *Nat Methods* [Internet]. 2008/05/11. 2008 Jun;5(6):535–8. Available from: <https://pubmed.ncbi.nlm.nih.gov/18469824>
209. Ramachandran N, Hainsworth E, Bhullar B, Eisenstein S, Rosen B, Lau AY, et al. Self-Assembling Protein Microarrays. *Science (80-)* [Internet]. 2004 Jul 2;305(5680):86 LP – 90. Available from: <http://science.sciencemag.org/content/305/5680/86.abstract>

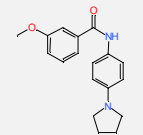
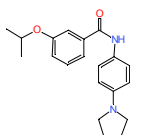
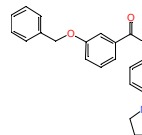
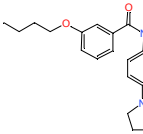
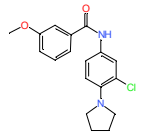
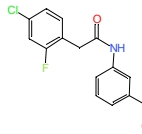
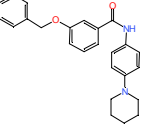
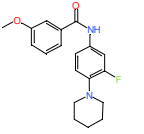
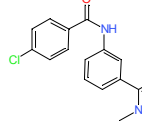
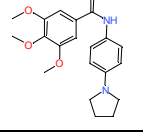
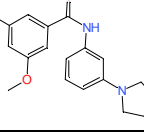
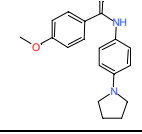
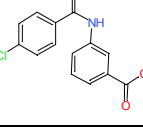
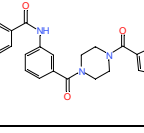
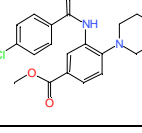
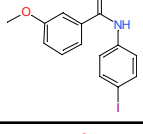
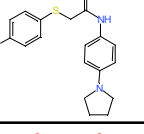
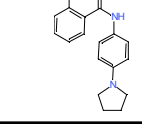
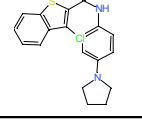
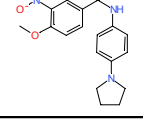
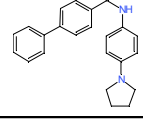
APPENDIX A
FULL DOCKING SCORES FOR SBI-183

Title	docking score	mol MW	dipole	SASA	FOSA	FISA	PISA	WPSA	volume	donorHB
SBI-0143183	-7.052	296.368	5.628	596.922	279.955	48.024	268.942	0	1023.298	1
Title	accptHB	dip ² /V	ACxDN ⁵ /SA	glob	QPolrz	QPlogPC16	QPlogPoct	QPlogPw	QPlogPo/w	QPlogS
SBI-0143183	4.25	0.030956	0.0071199	0.8227147	35.44	10.129	15.387	8.301	3.9	-5.125
Title	CIQPlogS	QPlogHERG	QPPCaco	QPlogBB	QPPMDCK	QPlogKp	IP(eV)	EA(eV)	#metab	QPlogKhsa
SBI-0143183	-4.301	-5.683	3471.271	-0.09	1899.127	-1.169	7.854	0.305	2	0.448
Title	HumanOralAbsorption	PercentHumanOralAbsorption	SAfluorine	SAamideO	PSA	#NandO	RuleOfFive	RuleOfThree	#ringatoms	#in34
SBI-0143183	3	100	0	0	47.366	4	0	0	17	0
Title	#in56	#noncon	#nonHatm	Jm	compound code					
SBI-0143183	17	4	22	0.15	SBI-0143183					

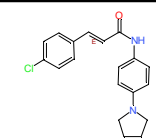
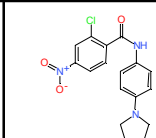
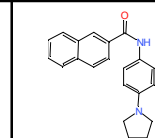
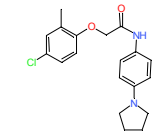
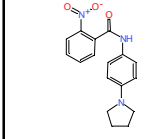
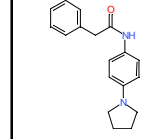
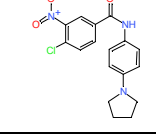
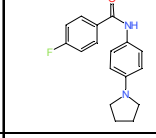
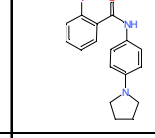
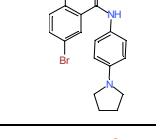
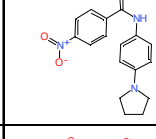
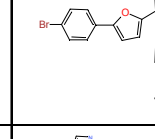
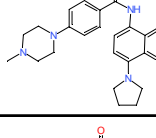
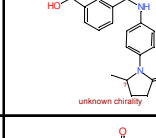
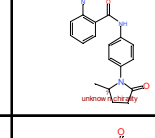
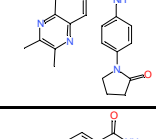
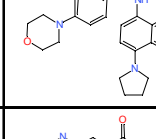
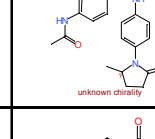
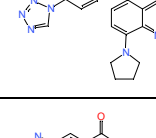
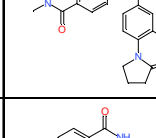
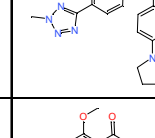
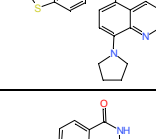
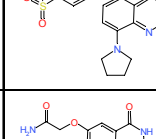
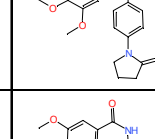
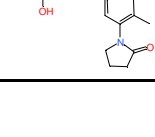
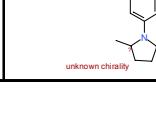
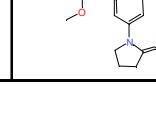
Table 5. Full results from SBI-183 docking protocols.

APPENDIX B
CHEMICAL STRUCTURES FOR TESTED COMPOUNDS

COLOR CODE: CHEMICAL CHANGES & RESULTANT HVA ASSAY ACTIVITY	
LOSS OF INHIBITION	Changes to permissive benzene
	Changes to variable benzene
	Changes to permissive & variable benzene
	Changes to permissive benzene & add to pyrrolidine
	Changes to permissive & variable benzene & add to pyrrolidine
SAME OR BETTER INHIBITION	Changes to permissive benzene
	Changes to permissive & variable benzene
	Change to permissive benzene & remove from pyrrolidine
UNKNOWN	Undefined

SPX ID	MW	Structure	SPX ID	MW	Structure	SPX ID	MW	Structure
SBI-183	296		1	324		2	372	
3	338		4	331		5	306	
6	386		7	328		8	301	
9	356		10	326		11	296	
12	290		13	417		14	416	
15	353		16	347		17	296	
18	357		19	341		20	342	

Continued.

SPX ID	MW	Structure	SPX ID	MW	Structure	SPX ID	MW	Structure
21	327		22	346		23	316	
24	345		25	311		26	280	
27	346		28	284		29	392	
30	380		31	311		32	411	
33	416		34	338	 <small>unknown chirality</small>	35	361	 <small>unknown chirality</small>
36	360		37	402		38	351	 <small>unknown chirality</small>
39	385		40	376		41	413	
42	388		43	395		44	370	
45	338		46	367	 <small>unknown chirality</small>	47	370	

Continued.

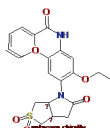
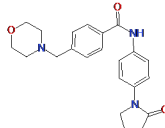
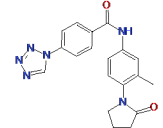
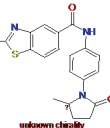
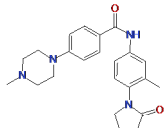
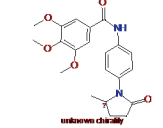
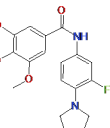
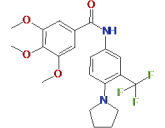
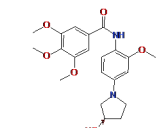
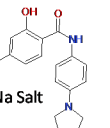
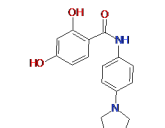
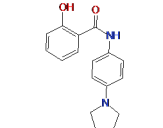
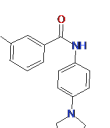
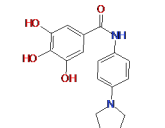
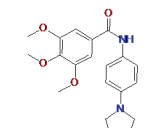
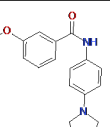
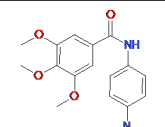
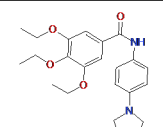
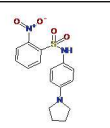
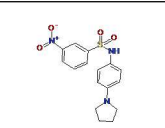
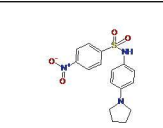
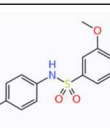
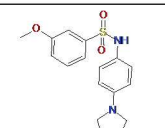
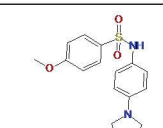
SPX ID	MW	Structure	SPX ID	MW	Structure	SPX ID	MW	Structure
48	447		49	379		50	362	
51	365		52	393		53	384	
AM-2172	374		QA-3179	424		SS-3742	402	
5103	298		5104	298		5132	282	
5137.1	282		5137.2	314		5177	358	
5179	298		5221	330		5226	399	
5229.1	347		5229.2	347		5229.3	347	
6003	362		52091	332		52092	332	

Table 6. List of SPX compounds and structures. The table displays the SPX ID, the molecular weight (MW) and the structure for each compound. Compounds 1-53 were purchased from ChemBridge. The subsequent eighteen compounds were synthesized by Sapphire Biotech. The color code represents the chemical modifications made to the structure of SBI-183 and the resultant inhibitory activity in the HVA fluorescence assay.